https://lib.uliege.be https://matheo.uliege.be

Mémoire

Auteur : Ernst, Vincent
Promoteur(s) : Dupret, Marc-Antoine; Van Grootel, Valérie
Faculté : Faculté des Sciences
Diplôme : Master en sciences spatiales, à finalité approfondie
Année académique : 2024-2025
URI/URL : http://hdl.handle.net/2268.2/22968

Avertissement à l'attention des usagers :

Tous les documents placés en accès ouvert sur le site le site MatheO sont protégés par le droit d'auteur. Conformément aux principes énoncés par la "Budapest Open Access Initiative"(BOAI, 2002), l'utilisateur du site peut lire, télécharger, copier, transmettre, imprimer, chercher ou faire un lien vers le texte intégral de ces documents, les disséquer pour les indexer, s'en servir de données pour un logiciel, ou s'en servir à toute autre fin légale (ou prévue par la réglementation relative au droit d'auteur). Toute utilisation du document à des fins commerciales est strictement interdite.

Par ailleurs, l'utilisateur s'engage à respecter les droits moraux de l'auteur, principalement le droit à l'intégrité de l'oeuvre et le droit de paternité et ce dans toute utilisation que l'utilisateur entreprend. Ainsi, à titre d'exemple, lorsqu'il reproduira un document par extrait ou dans son intégralité, l'utilisateur citera de manière complète les sources telles que mentionnées ci-dessus. Toute utilisation non explicitement autorisée ci-avant (telle que par exemple, la modification du document ou son résumé) nécessite l'autorisation préalable et expresse des auteurs ou de leurs ayants droit.

FACULTY OF SCIENCES

DEPARTEMENT OF ASTROPHYSICS, GEOPHYSICS AND OCEANOGRAPHY

MASTER THESIS

Multi-Messenger Study of White Dwarf Binaries

A thesis submitted to obtain the degree of Master in Space Sciences, Research Focus

Author:
Vincent ERNST

Supervisers:
Marc-Antoine DUPRET
Valérie VAN GROOTEL

Reading committee:
Jean-Marie BECKERS
Maxime FAYS
Camilla PEZZOTTI

Academic year 2024-2025

Abstract

Tidal interactions and gravitational wave emission both drive the orbital evolution of compact binaries, yet their precise interplay in double white dwarf systems has not been fully explored. In this thesis, we focus on DA white dwarfs near and within the ZZ Ceti instability strip. We combine asteroseismic theory with the non-adiabatic oscillation codes *MAD* and *MAD_tides*, along with Peters' gravitational wave formulas, to compute tidal and gravitational wave torques near spin-orbit synchronisation. We demonstrate that when the orbital forcing frequency matches a white dwarf's eigenmode, tides and gravitational waves can balance, creating *resonance locking* points. We show that these locking points are favoured when white dwarf masses are lower and spin rates higher. By performing backward integrations of the gravitational wave equations from locking points, we show that these binaries must have had orbital periods below a few hours at earlier epochs. Comparison with Sloan Digital Sky Survey (SDSS)-selected extremely low-mass white dwarf binaries supports the existence of systems within this locking region.

Acknowledgments

My first thanks go to my supervisors, Valérie Van Grootel and Marc-Antoine Dupret, for their involvement, kindness and benevolence throughout this work and beyond. I also want to sincerely thank Loïc Fellay for his essential help throughout this work.

I would also like to thank Jean-Marie Beckers, Maxime Fays and Camilla Pezzotti for being part of my reading committee. I hope you will enjoy reading this thesis as much as I enjoyed writing it.

This master's thesis represents the culmination of five years of study at the University of Liège. I thank all the professors from the Bachelor's in Physics, who provided me with the essential knowledge to pursue my passion for Astronomy and Astrophysics. I also thank all the professors from the Master in Space Sciences for sharing their passion through teaching over the past two years. Their availability and welcoming nature were invaluable throughout my education. In particular, I express my gratitude to Michaël De Becker, who guided me in making the best decisions for my studies even before I began university.

Finally, I would like to thank everyone at the University who contributed to my time here and to making this work possible, from the administrative and technical staff to the cleaning teams.

None of this would have been possible without the unconditional love and support of my parents. I also thank my siblings and my partner for their unwavering encouragement. A heartfelt thank you as well to my friends Antoine Dessart and Théotime Vande Populiere, with whom I forged lifelong bonds during our time at university. Last but not least, I am grateful for the comforting presence of Sherlock, who has been a loyal companion throughout this journey.

Contents

Introduction

In recent years there has been growing interest in compact binary systems, driven by high-precision space-based missions (e.g. CoRoT, Kepler, TESS) and revolutionary discoveries in gravitational wave astrophysics (LIGO, VIRGO, KAGRA).

White dwarfs have been among the greatest beneficiaries of precise photometric and astrometric surveys. As the endpoints of low-mass stellar evolution, they are crucial to understanding the fate of stars like our Sun. A key asteroseismic finding is that white dwarfs form distinct families of pulsators. These families are defined by differing surface and core compositions and by distinct effective temperature ranges, within which unstable oscillation modes can propagate. As a white dwarf evolves, it can thus cross these *instability strips* and undergo such pulsations. Their detailed analyses have allowed us to probe the interiors of these dense, opaque objects, yielding insights into their internal structures and compositions.

It is now well established that white dwarfs frequently occur in binary systems. While companions may vary in nature, this work focuses exclusively on double white dwarf binaries. In Jackim et al. (2024), over 300 000 binary white dwarf candidate systems were identified from GALEX and Gaia data. The close proximity of two white dwarfs gives rise to significant tidal interactions. Whenever a white dwarf's spin is not perfectly synchronised with the orbital frequency, *dynamical tides*—tidal "waves"—arise on its surface, applying a torque to its spin and altering the orbital motion. Depending on whether the white dwarf is within one of the instability strips and whether it rotates faster or slower than the orbital motion, these torques can drive the components closer together or push them further apart. Moreover, each white dwarf possesses its own set of free oscillation frequencies. When the orbital forcing frequency matches a white dwarf's free oscillation frequency, the two phenomena enter in resonance, greatly enhancing the dynamical tide effects on the orbital elements and on the star's spin rate.

White dwarf binaries are yet to be detected through their gravitational wave emission. Current ground-based detectors are sensitive to frequencies above a few hertz and have observed only massive compact binaries (neutron stars and black holes) at the time of merger. By contrast, future space-based observatories such as the *Laser Interferometer Space Antenna* (LISA) will probe the millihertz band, notably allowing the detection of white dwarf binaries with orbital periods of several minutes or longer. Gravitational wave emission removes angular momentum from the system and acts to circularise the orbit.[1] Consequently, the two components spiral inwards over time, ultimately leading to coalescence.

---

[1] Throughout this thesis, we refer to relativistic effects on the orbital elements—responsible for gravitational wave emission—as the *effect of gravitational waves* on those elements.

This thesis investigates the combined influence of tides and gravitational waves on the dynamics of hydrogen atmosphere (DA) white dwarf binaries. As stated earlier, while gravitational wave emission invariably reduces the binary separation, tidal torques can either reinforce or oppose this effect, potentially giving rise to scenarios in which the two contributions balance. In particular, the sharp increase in tidal intensity near resonances may be crucial to such behaviour. To explore these issues, we address the following questions:

1. Which process—tides or gravitational waves—dominates the secular evolution of the semi-major axis?
2. Do epochs exist in the binary's evolution when tidal and gravitational wave contributions exactly balance, producing locking points?
3. Which system parameters (mass, rotation rate, effective temperature, core composition, eccentricity) make locking more likely?
4. How do white dwarf binaries evolve under the combined influence of tides and gravitational waves, particularly in the vicinity of locking points?
5. What region of parameter space allows binaries to encounter locking points during their evolution?
6. Is there observational evidence supporting the existence of systems within this region of the parameter space?

In this thesis we demonstrate that, although gravitational wave emission dominates over tidal effects for most of a white dwarf binary's evolution, locking points can nonetheless arise at orbital resonances. Systems encountering *resonance locking* occupy a restrictive region of parameter space—mainly characterised by mass, temperature and separation. Preliminary observational evidence indicates that binaries within this region do indeed exist.

In practice, we first restrict our analysis to circularised white dwarf binaries. This circular approximation greatly simplifies the governing equations and helps building physical intuition. Thus, in the theoretical part, we will highlight each simplification this assumption brings. Once the circular case is fully explored, we then go beyond this assumption and introduce orbital eccentricity to assess its impact on resonance locking.

This thesis is organised in two main parts. The first is dedicated to the theoretical framework. Chapter 1 reviews the fundamentals of stellar astrophysics, outlines stellar evolution and emphasises the physics of white dwarfs. Chapter 2 introduces free stellar oscillations, while Chapter 3 describes tidal interactions in binaries and their relation to stellar oscillation modes. Chapter 4 concludes the theoretical part by presenting the equations governing gravitational wave emission and its effect on binary dynamics.

The second part presents our methods and results. Chapter 5 introduces the white dwarf models and the non-adiabatic oscillation code *MAD* used in this work. Chapter 6 describes the dynamical tide code *MAD_tides* and our implementation of the gravitational wave evolution equations. It demonstrates that gravitational waves generally dominate tidal effects except at resonances, and identifies the conditions under which resonance locking points arise. Chapter 7 maps the region of parameter space in which a binary must reside to encounter locking points during its evolution and compares these predictions with observational data, demonstrating that such systems are likely to exist. Finally, the concluding chapter summarises our conclusions and outlines prospects for future work.

Part I

Theoretical Introduction

Chapter 1

Stellar Astrophysics

In this chapter, we review the essentials of stellar astrophysics needed for our study. We begin by defining how a star's luminosity, flux, and magnitude relate to its effective temperature and position on the Hertzsprung-Russell diagram. We then outline stellar evolution, from the main sequence through the giant phases to compact remnants. Next, we present the four fundamental equations of stellar structure: mass continuity, hydrostatic equilibrium, radiative transport, and convective transport. Finally, we delve deeper into white dwarfs by describing their internal structure, cooling behaviour and pulsation families.

1.1 Basic concepts

To begin this chapter, we will start by presenting some basic concepts in Stellar Astrophysics. The total power radiated by a star is defined as its *luminosity* L, given at the surface by

$$L = 4\pi R^2 \int_0^\infty F_\lambda(R) d\lambda \tag{1.1}$$

where R is the radius of the star and $F_\lambda(R)$ is the monochromatic flux at a wavelength λ at the surface of the star, which is a measure of energy per unit time, per unit surface and per unit wavelength. The luminosity of stars can vary largely, with typical values ranging from $10^{-3}\,L_\odot$ to $10^6\,L_\odot$.[1,2]

The integral in Eq. (1.1) yields the *bolometric flux* b at the surface of the star. It is important to note that the bolometric flux at the surface cannot be measured directly. Observations are typically limited to specific filter bands and require models to infer the bolometric flux, which induces possible errors. Additionally, the observed flux corresponds to the radiation received at a distance d from the star. While d can be estimated through various methods, it remains a significant source of uncertainty in determining the star's luminosity. For an observer measuring a bolometric flux F at a distance d from the star, the luminosity is given by:

$$L = 4\pi d^2 F(d) \tag{1.2}$$

---

[1] Any quantity with a subscript $\odot$ refers to this quantity for the Sun.

[2] The faintest known white dwarfs have luminosities of $\sim 10^{-4.7}\,L_\odot$, whereas the brightest reach $\sim 10^3\,L_\odot$ (Fontaine et al., 2001).

The *magnitude* m is a logarithmic scale used for the measure of the brightness of stars. It is defined as:

$$m = -2.5\log(F) + C \tag{1.3}$$

where C is a constant originally chosen such that the magnitude of Vega is equal to 0. The value of m therefore depends on the observer. If the distance of a star to the observer is known, one can compute its absolute magnitude M, which corresponds to the apparent magnitude the star would have if it was at a distance of 10 parsecs (pc) to the observer:

$$M = -2.5\log(B) + C \tag{1.4}$$

where B is the bolometric flux the star would have at this distance. We therefore have:

$$M - m = 5 - 5\log(d_{pc}) \tag{1.5}$$

where d_{pc} is the real distance of the star to the observer in parsecs. The absolute magnitude is therefore independent of the observer and can be used to compare stars similarly to the luminosity, but with a restricted range of values through to the use of a logarithmic scale.

The spectrum of a star is similar to the spectrum of a *blackbody*. The monochromatic flux of a blackbody at temperature T follows Planck's law:

$$F_\lambda = \frac{2\pi hc^2}{\lambda^5}\frac{1}{\exp(hc/\lambda kT) - 1} \tag{1.6}$$

where c is the speed of light, h is Planck's constant and k is Boltzmann's constant. Integrating this function yields the Stefan-Boltzmann law:

$$F = \int_0^\infty F_\lambda d\lambda = \sigma T^4 \tag{1.7}$$

where σ is the Stefan-Boltzmann constant. From this equation, the effective temperature T_{eff} of a star is defined as the temperature a blackbody would need to have in order to radiate the same bolometric flux as the star:

$$T_{\text{eff}} \equiv \left(\frac{F}{\sigma}\right)^{\frac{1}{4}} \tag{1.8}$$

Finally, the Wien law gives the value of the wavelength, in centimetres (cm), at the maximum of Planck's law from the temperature, in kelvins (K), of the blackbody:

$$\lambda(cm) = \frac{0.29}{T(K)} \tag{1.9}$$

Wien's law therefore yields the value of the temperature of a blackbody only from the knowledge of the wavelength at the maximum of Eq. (1.6).

Based on their luminosity L and their effective temperature T_{eff}, stars can be represented conveniently in a Hertzprung-Russell diagram as shown in Figure 1.1. These two quantities are often characteristic of certain types of objects and evolutionary phases, as detailed in the following section. The Hertzsprung-Russell diagram is commonly used to illustrate the different categories of stars within a population or to depict their evolutionary paths.

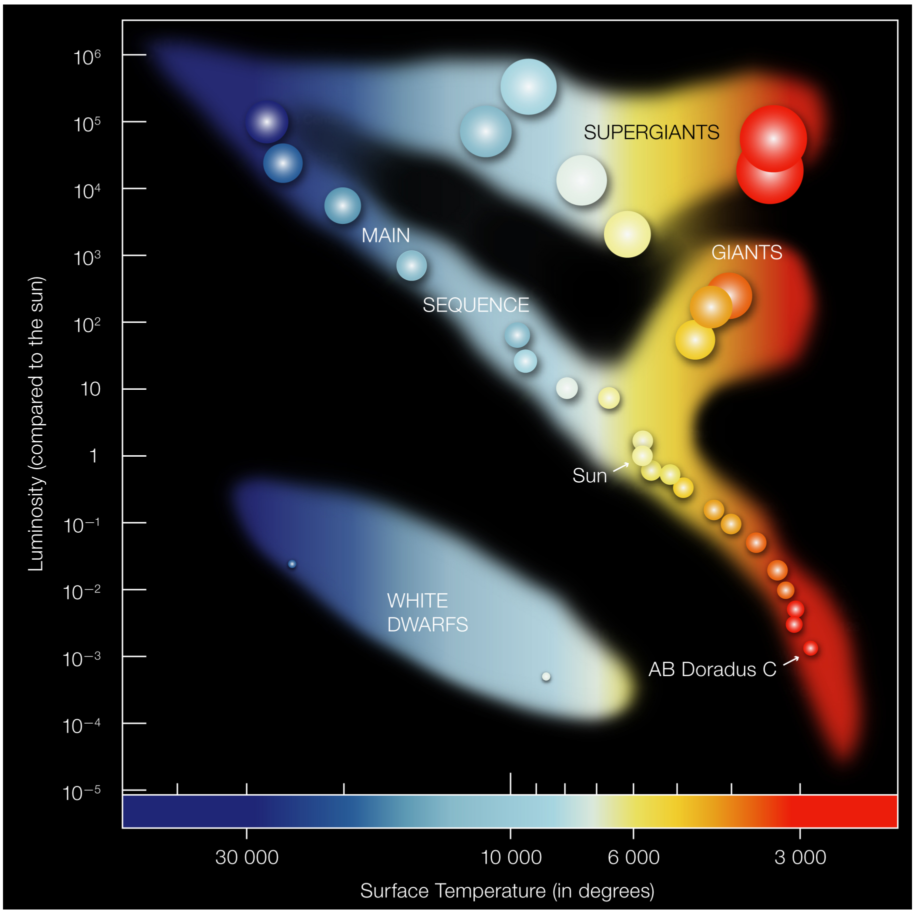

Figure 1.1: Hertzsprung-Russell diagram. Credit: ESO (2007).

1.2 Stellar evolution phases

In the following, we present the outline of the typical evolutionary pathway of stars.[3] In this context, one must stress on the crucial role played by the mass of the star as it enters in main sequence. This mass is referred to as the *zero age main sequence* (ZAMS) mass.

Stars form through the gravitational collapse of molecular clouds. If the mass of the resulting object is below $0.01\,M_\odot$, nuclear burning will not occur. The object is classified either as a *planet* or a *brown dwarf*, depending on the adopted definition. For masses between $0.01\,M_\odot$ and $0.08\,M_\odot$, some deuterium burning occurs during the formation. However, the sufficient conditions for sustained nuclear fusion are not met in the core of the star, preventing the object from entering any phase of stable nuclear burning. Such an object is classified as a brown dwarf.

Stars with a ZAMS mass between $0.08\,M_\odot$ and $8\,M_\odot$ are usually referred to as *low-mass stars*, in opposition to *massive stars* having a ZAMS mass above $8\,M_\odot$. The current upper limit for the ZAMS mass of stars is believed to be of the order of $\sim 100\,M_\odot$. Very massive stars aside, all these stars begin their evolution similarly. Following their formation and some short-lived deuterium burning, stable hydrogen fusion establish in the core of the

---

[3] For certain peculiar stars, such as very massive stars like Wolf-Rayet stars, highly magnetic stars, or stars with strong interactions with a companion, the evolutionary path may differ.

star. This is the point at which the star truly enters the *main sequence*. This phase is the longest phase of stellar evolution, representing $\sim 90\%$ of the stars' lifetime, from onset of core hydrogen fusion to the end of it. This explains why most stars that are observed are in this phase.

In the Hertzsprung-Russell diagram (Figure 1.1), stars in their main sequence occupy a diagonal band that extends from the upper left (high luminosity, high effective temperature) to the lower right (low luminosity, low effective temperature). This region therefore represents stars undergoing stable hydrogen fusion in their cores, with hotter, more massive stars appearing toward the upper end of the sequence and cooler, lower-mass stars toward the lower end.

Depending on their ZAMS mass, stars leave the main sequence through different evolutionary pathways. After exhausting hydrogen in the core, the helium core of a low-mass star contracts under gravity and increases in temperature, while hydrogen fusion continues in a shell surrounding the core. This helium core is *degenerated*, meaning that the pressure needed to avoid a collapse of the core is provided by the electron degeneracy pressure, and grows in mass as shell burning proceeds.[4] At the beginning of shell hydrogen burning, the star departs the main sequence and ascends the red-giant branch (RGB): its radius increases by several orders of magnitude, reaching tens to hundreds of solar radii, and its luminosity rises in accordance with Eq. (1.1). Throughout the RGB phase, the effective temperature stays lower than during the main sequence, placing these stars in the upper-right (high luminosity, low effective temperature) region of the Hertzsprung-Russell diagram. When the core temperature approaches $10^8\,\mathrm{K}$, core helium fusion begins, ending the RGB phase in a rapid event known as the *helium flash*. Note that stars with ZAMS mass below $\approx 0.4\,M_\odot$ never reach the conditions for core helium burning and would instead evolve directly into helium core white dwarfs. However, their evolutionary timescales exceed the age of the Universe, so none of the observed helium core white dwarfs can have formed in this way.

The energy released during the helium flash lifts the core degeneracy. The star then enters a *stable core helium burning* phase, converting helium into carbon and oxygen. In addition, the core expands, causing the radius to contract from its RGB maximum and the surface temperature to increase. On the Hertzsprung-Russell diagram, the star is on the *horizontal branch*, with luminosities of a few tens to a few hundred solar luminosities.

Once central helium is exhausted, the star evolves onto the asymptotic giant branch (AGB), characterised by two burning shells: while the degenerate carbon-oxygen core contracts, helium fusion continues in a shell immediately above it, and hydrogen fusion persists in a shell above the helium layer. The envelope expands again, reaching luminosities of order $10^4\,L_\odot$, and the surface temperature decreases, placing these stars once again in the upper-right region of the Hertzsprung-Russell diagram. Stellar winds during the AGB phase are intense, causing a significant part of the envelope to be lost.

After losing their envelope, some stars enter the *thermally pulsing AGB* (TP-AGB) phase. Without the envelope, stable helium burning does not occur in the star. The

---

[4] Degenerate electrons have very high thermal conductivity. Hence, the degenerate helium core remains nearly isothermal.

helium therefore accumulates in a shell around the carbon-oxygen core and can ignite briefly, producing thermal pulses. These repeated pulses and the winds lead to the ejection of the remaining envelope, thereby exposing the hot carbon-oxygen core. This core then stabilises into a white dwarf composed mainly of carbon and oxygen (or helium in the lowest-mass remnants), supported by electron degeneracy pressure. Some stars do not experience thermal pulses and their core directly evolve into white dwarfs. White dwarfs are discussed in more detail in Section 1.5.

Massive stars undergo complex evolutionary processes as they approach the end of their lives. Following the depletion of core hydrogen, these stars enter successive stages of nuclear fusion, synthesising increasingly heavy elements up to iron. The fusion of iron (and heavier elements) is endothermic and hence does not take place in the star. Iron therefore accumulates in the core of the star which becomes degenerated. As the mass of the iron core increases, the electrons become relativistic and eventually saturate at the speed of light. The core has reached the *Chandrasekhar mass* M_{ch}, given by

$$M_{ch} = \left(\frac{2}{\mu_e}\right)^2 \times \; 1.459 M_\odot \tag{1.10}$$

where μ_e is the average number of nucleons per electron, which is close to 2 in this situation. Past this limit, the degenerated core can no longer resist to the gravitational force and collapses. Once again, the result of the collapse is dependent on the ZAMS mass of the star. Typical massive stars with a ZAMS mass between $8\,M_\odot$ and $25\,M_\odot$ will see their core collapse into a *neutron star*, a very dense remnant of $\sim (1-2)\,M_\odot$ with radius of the order of $\sim (10-15)\,\mathrm{km}$. The collapse of the core is very brief. After bouncing off the collapsed core, the outer layers of the star are violently ejected in the surrounding medium in an event called a *supernova*.[5] Massive stars with a ZAMS above $25\,M_\odot$ can see their core collapse either into a temporary, unstable neutron star—which eventually collapses into a black hole—or directly into a black hole. If the outer layers are ejected, they can result in a bright supernova called a *hypernova*. However, it is believed that in some situations the entirety of the star could fall into the newly-formed black hole, leading to a failed supernova (Schaffner-Bielich, 2020).

To conclude this section, it is important to emphasise that the ZAMS mass is the *primary* factor determining the duration of the main sequence as well as the red giant and supergiant phases. In general, more massive stars burn their nuclear fuel significantly more rapidly than their lower-mass counterparts. Hence, there is in an inverse relationship between a star's lifetime and its ZAMS mass. Other factors—such as chemical composition, stellar rotation, and interactions with a companion—can also influence these timescales and the resulting remnants.

---

[5] Supernovae therefore play an important role in the enrichment of the interstellar medium by providing heavy elements synthesised both during the main sequence and during the supernova event itself.

1.3 Equations of stellar structure

In this section, we provide a first physical description of stars in an equilibrium state. We consider a static, non-rotating star and assume it to be spherically symmetric. The impact of the magnetic field on the internal structure is also neglected. Thus, all physical quantities are assumed to depend only on the radial distance from the centre of the star and on time.

Mass and density

Consider a very thin spherical shell of radius r and thickness δr of the star. This shell therefore has a volume $\delta V = 4\pi r^2 \delta r$ at first order in δr. By definition of the density ρ, we have that the mass of this thin shell is $\delta m = \rho \delta V = 4\pi r^2 \rho \delta r$. Dividing by δr and taking the limit for $r \to 0$, we obtain the differential equation:

$$\frac{dm}{dr} = 4\pi r^2 \rho \tag{1.11}$$

Integrating therefore yields:

$$m(r) = \int_0^r 4\pi r^2 \rho dr \tag{1.12}$$

In the above equations, $m(r)$ is the mass contained within a sphere of radius r centered on the star. We therefore have $m(0) = 0$ and, if we write R for the radius of the star and M for its total mass, $m(R) = M$.

Hydrostatic equilibrium

The stability of a star during its main sequence phase, as well as in most later stages, is maintained by an equilibrium between the pressure, which pushes outward, and the gravitational force, which pulls inward toward the centre of the star. This balance is described by the *hydrostatic equilibrium* equation, which relates the pressure P to the enclosed mass m within a radius r through the relation:

$$\frac{dP}{dr} = -\frac{Gm\rho}{r^2} \tag{1.13}$$

where G is the gravitational constant and ρ is the density at the radius r. Using Eq. (1.11), this equation can be expressed under the integrated form:

$$P(m) = \int_m^M \frac{Gm}{4\pi r^4} \, dm \tag{1.14}$$

Transport of energy by radiation

A further crucial equilibrium inside stars is the maintenance of thermal balance between energy production and energy loss through surface radiation. Energy is primarily provided via nuclear fusion in the core, supplemented by the conversion of gravitational potential energy into thermal energy during contraction. Because most of this energy is generated in the central regions while the outer layers continuously radiate it, this energy must be transported outward. Two principal processes can be at play: convection and radiation.[6]

---

[6] Conduction does not contribute significantly to energy transport in main-sequence star. However, it must be accounted for when studying white dwarfs (see Fontaine et al. 2001).

Assuming the star behaves as a blackbody, the transport by radiation can be evaluated at any layer of the star as the power L_R going through a spherical shell of radius r through the relation:

$$L_R = -\frac{16\pi r^2 acT^3}{3\kappa\rho}\frac{dT}{dr} \tag{1.15}$$

where $a = 4\sigma/c$ is the radiation constant and κ is the Rosseland mean opacity defined by:

$$\kappa = \left[\frac{\pi}{acT^3}\int_0^\infty \frac{1}{\kappa_\lambda}\frac{dB_\lambda}{dT}d\lambda\right]^{-1} \tag{1.16}$$

where B_λ is the Planck function per unit wavelength for the spectral radiance and κ_λ is the opacity per unit wavelength.

Let us now introduce the *real temperature gradient* ∇_T, which will be used when studying convection. It is defined by:

$$\nabla_T \equiv \frac{d\ln T}{d\ln P} = \frac{P}{T}\frac{dT/dr}{dP/dr} = -\frac{r^2 P}{\rho GmT}\frac{dT}{dr} \tag{1.17}$$

where Eq. (1.13) has been used. Substituting in Eq. (1.15) yields:

$$L_R = \frac{16\pi acGmT^4}{3\kappa P}\nabla_T \quad \Leftrightarrow \quad \nabla_T = \frac{3\kappa PL_R}{16\pi acGmT^4} \tag{1.18}$$

Transport of energy by convection

When radiative energy transport alone is insufficient to carry the energy from the deeper regions of the star to its outer layers, convection may become the dominant transport mechanism. Convection occurs in a fluid in hydrostatic equilibrium when a sufficiently high temperature gradient is applied. This movement of matter from the warm, dense inner regions of the star to the cooler, outer regions transports a part of the energy flux of the star. The power carried by convective motions is denoted by L_C, and the total luminosity L can be expressed as the sum of the contributions from both radiation and convection:

$$L = L_R + L_C \tag{1.19}$$

In order to obtain a practical condition on convective instability, two gradients must be introduced. The first is the *radiative gradient*, obtained by substituting L_R for the total luminosity in Eq. (1.18):

$$\nabla_{rad} \equiv \frac{3\kappa PL}{16\pi acGmT^4} \tag{1.20}$$

This gradient therefore represents the temperature gradient that would be required to transport all the energy by radiative transport alone. The second gradient is the *adiabatic gradient*, defined by:

$$\nabla_{ad} = \left.\frac{\partial\ln T}{\partial\ln P}\right|_S \tag{1.21}$$

where the partial derivative is taken at constant entropy S. The adiabatic gradient represents the temperature variation experienced by an element of gas when it is displaced vertically and adiabatically.[7] A layer of the star is convectively unstable if

$$\nabla_{rad} > \nabla_{ad} \tag{1.22}$$

This condition is called the *Schwarzschild criterion* of convective instability. Regions of the star where this condition is met are thus *convective regions*, in opposition to *radiative regions*, where the energy is transported by radiation only.

1.4 Compact stars

Compact stars is a specific category of astrophysical objects that includes white dwarfs, neutron stars and black holes.[8] Intermediate to supermassive black holes aside, all these objects are generally the endpoint of stellar evolution, although some may also form through mergers, accretion-induced collapse, or other dynamical processes. Therefore, these objects can still evolve through interactions with their environment or a potential companion.

Compact stars involve a wide range of densities and involve all four fundamental forces: the strong nuclear force, the weak nuclear force, electromagnetism, and gravity, often under extreme conditions. The mean density $\bar{\rho}$ of a compact star is defined as

$$\bar{\rho} = \frac{3M}{4\pi R^3} \tag{1.23}$$

with the total mass M and the radius R. The surface gravity g is defined as

$$g = \frac{GM}{R^2} \tag{1.24}$$

While the radii of several white dwarfs have been measured, the radius of neutron stars—significantly smaller—has been approximately measured in only a few cases. Consequently, constraints on neutron star radii are largely based on theoretical estimations. For black holes, the radius used is the Schwarzschild radius, defined as

$$R_S = \frac{2GM}{c^2} \tag{1.25}$$

The compactness C of an object is often introduced for compact stars. It is defined as:

$$C = \frac{GM}{Rc^2}. \tag{1.26}$$

For non-rotating black holes, the compactness is therefore equal to one half. One must mention that for a black hole the mean density is undefined. In addition, the surface gravity of a Schwarzschild black hole is defined as $\kappa = 1/(4GM)$, which is the acceleration experienced by an observer at the event horizon.[9] Typical values of compactness are shown on Figure 1.2.

---

[7] i.e. without exchanging heat with its surroundings.

[8] Some authors also include hot subdwarfs in this category.

[9] Note that due to relativistic effects, the acceleration at the black hole horizon diverges for a distant observer.

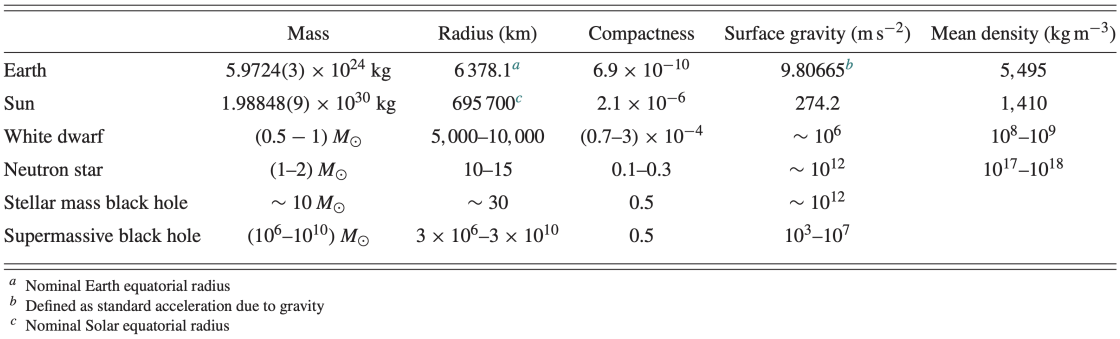

	Mass	Radius (km)	Compactness	Surface gravity ($\mathrm{m\,s^{-2}}$)	Mean density ($\mathrm{kg\,m^{-3}}$)
Earth	$5.9724(3) \times 10^{24}$ kg	6 378.1[a]	6.9×10^{-10}	9.80665[b]	5,495
Sun	$1.98848(9) \times 10^{30}$ kg	695 700[c]	2.1×10^{-6}	274.2	1,410
White dwarf	$(0.5 - 1)\,M_\odot$	5,000–10,000	$(0.7\text{–}3) \times 10^{-4}$	$\sim 10^{6}$	10^{8}–10^{9}
Neutron star	$(1\text{–}2)\,M_\odot$	10–15	0.1–0.3	$\sim 10^{12}$	10^{17}–10^{18}
Stellar mass black hole	$\sim 10\,M_\odot$	~ 30	0.5	$\sim 10^{12}$	
Supermassive black hole	$(10^{6}\text{–}10^{10})\,M_\odot$	3×10^{6}–3×10^{10}	0.5	10^{3}–10^{7}	

[a] Nominal Earth equatorial radius
[b] Defined as standard acceleration due to gravity
[c] Nominal Solar equatorial radius

Figure 1.2: Comparison of compact objects. Figure from Schaffner-Bielich (2020).

This work is centred around the physics of binary white dwarfs. In the next section, we will delve deeper into the physics of white dwarfs. For further information on neutron stars and black holes, we recommend the book *Compact Star Physics* by Schaffner-Bielich (2020), which served as the primary reference for this introduction to compact stars.

1.5 More on white dwarfs

Structure and composition

White dwarfs are degenerate stars. As no nuclear reactions occur within them, they remain in equilibrium due to their residual thermal energy and, primarily, the electron degeneracy pressure, which counterbalances gravitational collapse. A key consequence of this is that **the radius of a white dwarf is inversely proportional to its mass**. Hence, the lightest white dwarfs are also the largest. Aside from these significant differences, white dwarfs still follow the laws of stellar structure presented in Section 1.3.

We now examine the overall structure of a white dwarf, from its surface down to its core. The outermost region is known as the *atmosphere*, extending from the photosphere outwards. This layer only contains $\sim 10^{-14}$ of the mass of the white dwarf (Fontaine et al., 2001). Because the deeper layers are optically thick, the observed spectra of white dwarfs reflect solely the atmospheric composition. Depending on their history, white dwarfs can have various surface compositions which are thus not indicative of their core composition.

The variety of observed spectra has led to the introduction of a *spectral classification*. The classification currently used is based on Sion et al. (1983) and Wesemael et al. (1993). The first letter of the spectral type of a white dwarf is always be an upper D, standing for *degenerate*. It is then followed by a letter corresponding to the dominating spectral line in the optical band. The main classes are summarised by Bédard (2024) as follows:

- DA: hydrogen features
- DB: neutral helium features
- DC: no features (continuous spectrum)
- DO: ionised helium features
- DQ: carbon features
- DZ: other metal features

Additionally, a third letter can be added for the second dominating feature in this band, if present. Finally, a number from 0 et 9 is added as a temperature index. Additional subscripts can be included for specific characteristics such as polarisation of light.

Past the photosphere, we enter into the white dwarf's *envelope*. This layer is made of non-degenerated material and represents less than 1% of the total mass of the white dwarf (Fontaine et al., 2001). As we get deeper, the electron density increases as well as their Fermi momentum. When the electrons' energy equals their binding energy to the nucleus, the electrons can be stripped from the nucleus and matter becomes degenerated. A sharp change in chemical composition marks the end of the envelope and the beginning of the *core* of the white dwarf.

Since, as presented in Section 1.2, white dwarfs are the remnants of the cores of low-mass stars, their core composition is therefore related to the history of their parent star. The majority of observed white dwarfs are believed to possess a carbon-oxygen core (C-O), inherited from their helium core-burning progenitors with ZAMS masses between $0.4\,M_\odot$ and $8\,M_\odot$. For very massive white dwarfs, it is possible that their progenitors initiated core carbon and oxygen burning. In such cases, the resulting white dwarfs would have an oxygen-neon-magnesium core. For massive white dwarfs only, it is expected that the electron density and the momentum become so large deep in the crystalline region that it become energetically more favourable for electrons to interact with protons to form neutrons. Hence, the atomic nuclei are expected to be more neutron-rich in these deep regions than in the above layers (Schaffner-Bielich, 2020). Due to the degenerate electrons' high thermal conductivity, the core of white dwarfs is nearly isothermal (Fontaine et al., 2001).

Recent asteroseismic findings by Giammichele et al. (2018) have shown that C–O white dwarfs are significantly more oxygen-enriched in their interiors than previously believed. Figure 1.3 shows the interior structure of a C–O white dwarf, displaying the mass fractions

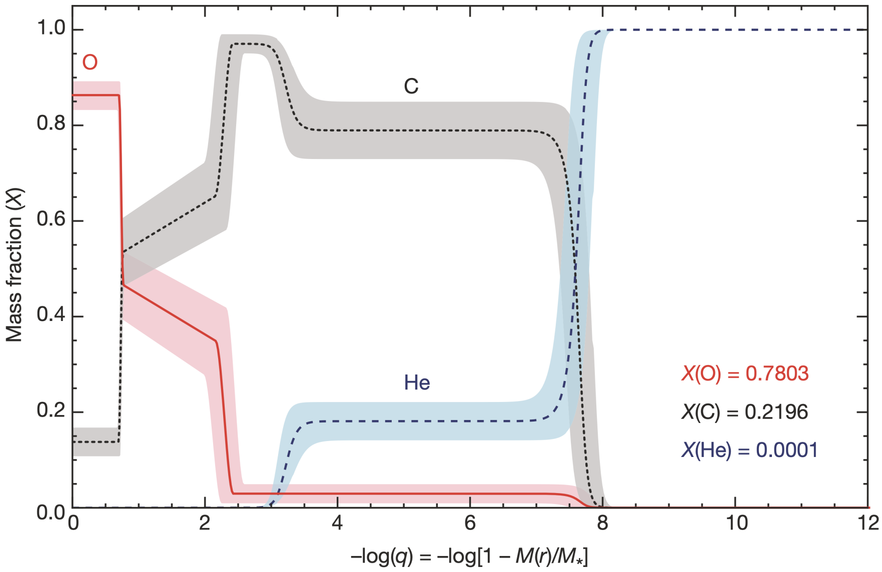

Figure 1.3: Derived chemical stratification of a C-O white dwarf. Credit: Giammichele et al. (2018)

of O, C, He, and H as a function of depth. The abscissa is defined as

$$-\log(q) \equiv -\log\left(1 - \frac{M(r)}{M_*}\right), \tag{1.27}$$

where M_* is the total mass of the white dwarf. This quantity represents the logarithm of the fraction of the white dwarf's mass lying above a radius r. Choosing $-\log q$ on the horizontal axis is common in compact star astrophysics, as it emphasises behaviour in the outermost layers, where most of the relevant physics occurs. In particular, the white dwarf envelope corresponds to $-\log q > 2$. Thus, with this choice of abscissa, the deepest layers appear on the left and the surface layers on the right. As shown on this figure, the chemical composition transitions are relatively sharp, a feature with important implications for oscillations (see Section 2.5).

The distribution of mass of known white dwarfs peaks at $\sim 0.6\,M_\odot$, which corresponds to the carbon-oxygen core white dwarfs presented above. However, there is a non-negligible tail extending towards the lower masses, down to $\sim 0.3\,M_\odot$ (Fontaine et al., 2001). This corresponds to core helium (He) white dwarfs, which should result from stars with ZAMS masses between $0.08\,M_\odot$ and $0.4\,M_\odot$, as core helium burning never occurs the core of such stars. As mentioned earlier, the evolutionary timescales for such low-mass stars exceed the current age of the universe. As a result, no such star has yet evolved into a white dwarf, and no very low-mass white dwarfs should be observed. **This remains true as long as we consider single-star evolution.** In binary systems, interactions with a companion can significantly alter stellar evolution. The companion of an RGB star may strip away its outer layers, leading to the formation of low-mass core helium white dwarf, often referred to as a *stripped RGB star.* Observational evidence indicates that the lightest white dwarfs are found exclusively in binary systems, strongly suggesting that their formation occurs through the stripped RGB process.

Cooling, convection and pulsations

Due to the absence of stable nuclear fusion, white dwarfs gradually radiate their energy. The presence and the size of convective zones depend on the white dwarf's cooling stage. In standard models, convective regions are predominantly confined to the envelope. When these regions extend into the atmospheric layers, they lead to the mixing of superficial material and can thus alter the observed spectral features. If convection reaches the degenerate, nearly isothermal core, it significantly enhances heat transport to the outer layers. This *convective coupling* increases the energy transfer between the core and the optically thick atmosphere well beyond the limits of radiative diffusion alone, effectively accelerating the cooling of the white dwarf.

White dwarfs show pulsations within specific ranges of temperature and $\log(g)$ called *instability strips.* As a white dwarf cools, it enters the instability strip through the strip's *blue edge* and leave it through the *red edge.* These boundaries are frequently revised and appear to be both mass and composition-dependent. Several families of pulsating white dwarfs are known. Let us first introduce the three main ones. We will here use typical temperature ranges provided in Fontaine & Brassard (2008)'s review. Let us insist on the fact that the precise entry and exit of a star in an instability strip is also dependent on its $\log(g)$.

The first instability strip covers a large range of temperatures: $\sim 75 - 170 \times 10^3$ K. These pulsators are called *GW Vir* stars. These objects show a remarkable variety of chemical composition from one star to another, leading to very uncertain strip edge values. In the $\sim 23 - 28 \times 10^3$ K temperature range, DB white dwarfs can start pulsating. These helium atmosphere pulsating stars are called *V777 Her* or *DBV*. Finally, DA stars can show pulsations in the $\sim 9 - 12 \times 10^3$ K range. These hydrogen-rich atmosphere white dwarfs are referred to as *ZZ Ceti* or *DAV* stars, which is the family we consider in this work. Other families of pulsating white dwarfs are shown in the Hertzsprung-Russell diagram in Figure 1.4.

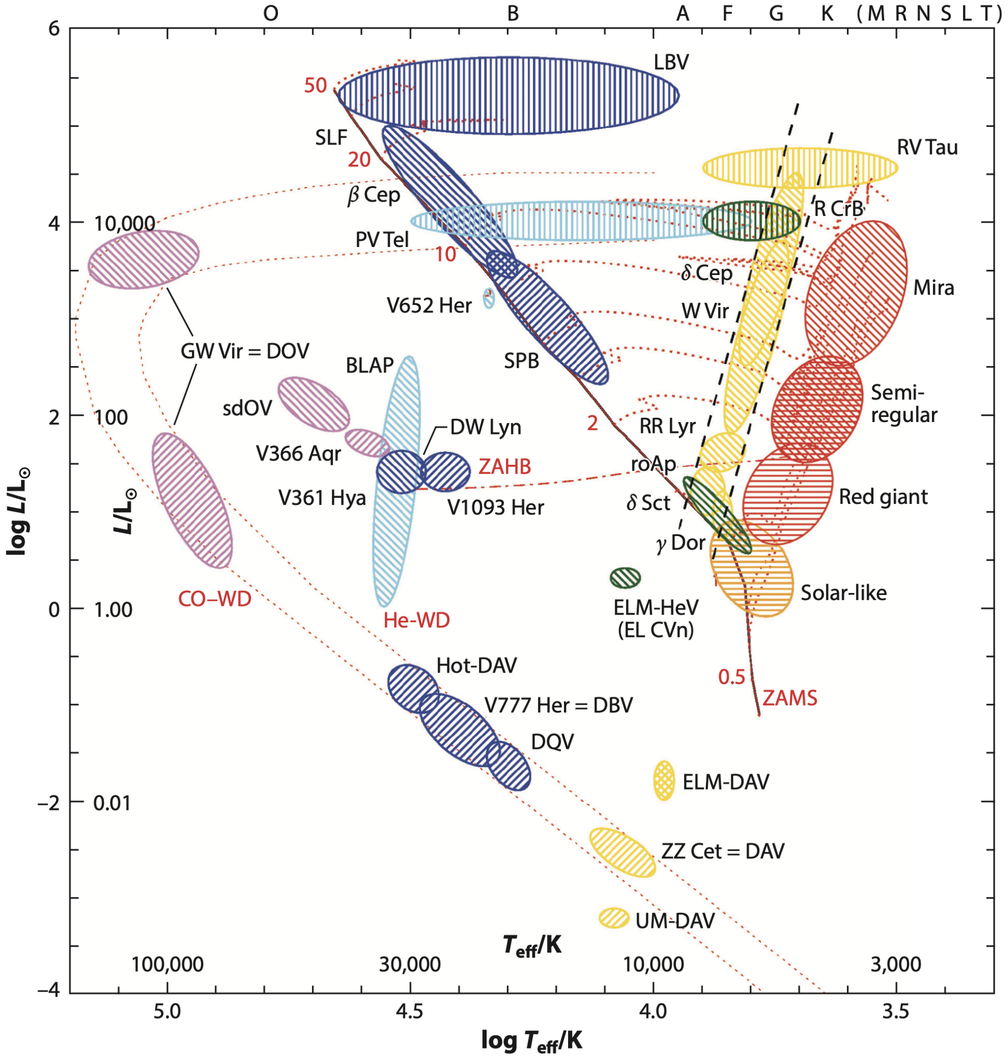

Figure 1.4: Various families of pulsating stars: White dwarfs exhibit pulsations under diverse conditions throughout their cooling track, leading to distinct classes of variable stars. Note the importance of the white dwarfs' composition. Credit: Kurtz (2022).

End of life

White dwarfs can end their lives in various ways. If they remain isolated and do not interact with other objects, white dwarfs are expected radiate away all their thermal energy over timescales exceeding the current age of the universe. These completely crystallised objects, called *black dwarf*, have therefore never been observed.

In binary systems, the white dwarf can accrete hydrogen from its companion star. If the white dwarf is well below the Chandrasekhar mass, the material can accumulate on its surface. At some point, the fusion of accumulated material can ignite for a very brief instant during which the entirety of the accreted hydrogen burns. After this burning, the white dwarf can continue accreting and start a new cycle. These brief increases in magnitude are called *novae*. If the white dwarf continues accreting material, it will eventually reach the Chandrasekhar mass, at which point the electron degeneracy pressure can no longer balance the weight of the star. This leads to a runaway thermonuclear reaction that totally disrupts the star. Since white dwarfs are typically composed of carbon and oxygen, and not hydrogen, the spectra of these bright events lack hydrogen lines and instead show a specific spectral signature dominated by elements like silicon. These explosions are referred to as *Type Ia supernovae*. Since they always occur when the white dwarf's mass approaches the Chandrasekhar limit, these events tend to be extremely similar in absolute magnitude. For this reason, Type Ia supernovae have historically been used as *standard candles* to measure distances in the nearby universe. To conclude, binary interaction can also lead to the merger of the two components. The outcome will largely depend on the nature of the white dwarf's companion.

Chapter 2

Stellar Oscillations

The history of asteroseismology is directly related to the discovery of the variability of stars. In the 17th century, Mira (o Ceti) was the first documented case of variable star, followed by Algol and classical Cepheid variables. The variability of stars is not necessarily due to stellar oscillations. Algol, for example, is an eclipsing binary system. Helioseismology, the study of the oscillations of the Sun, emerged in the 1960s, leading to major discoveries about our star's internal structure. Asteroseismology applied these principles to other stars, though the quality of ground-based observations showed to be limited. Space missions like CoRoT, Kepler, and TESS revolutionised the field, enabling precise stellar oscillation studies. In the near future, upcoming missions like PLATO, along with large-scale surveys, will continue to drive advancements in stellar physics (Bétrisey, 2024).

A key difference between helioseismology and asteroseismology is that the surface of other stars cannot be resolved. Consequently, observations are limited to variations in the stars' light curves. Through the analysis of these light curves, it is nonetheless possible to extract the spectrum of the stars' oscillation modes. As it will be shown further in the equations presented in this chapter, this spectrum depends on the physical properties of the star. Stellar oscillations have already proved to be powerful at probing the physical conditions in the interior of stars with many remarkable and unexpected results.

2.1 Stellar hydrodynamics

2.1.1 Typical timescales

As we begin to discuss dynamic phenomena, it is important to introduce three characteristic timescales commonly used in stellar astrophysics.[1] The first is the *dynamical time*, which represents the free-fall time of the outer layers of the star to the centre, assuming that the pressure is neglected. As such, it is defined as:

$$t_{\mathrm{dyn}} = \sqrt{\frac{R^3}{GM}} \tag{2.1}$$

The dynamical time yields the typical timescale for cycles of compression and decompression of the star's layers and hence is the typical timescale of stellar oscillations.

---

[1] The following definitions do not apply to black holes.

The *Helmholtz-Kelvin time* (or thermal time) is the characteristic timescale of thermal disequilibrium. It is the time it would take for the star, at its current luminosity L, to radiate the entirety of its gravitational energy if there was no nuclear reactions. It is therefore given by

$$t_{\text{HK}} = \frac{GM^2}{2RL} \tag{2.2}$$

Finally, the *nuclear time* of a star is the time needed by the star to radiate all the energy that it could produce through nuclear reactions throughout its lifetime.[2] We can therefore define it as

$$t_{\text{nuc}} = \frac{E_{\text{nuc}}}{L} \tag{2.3}$$

These timescales typically follow:

$$t_{\text{dyn}} \ll t_{\text{HK}} \ll t_{\text{nuc}} \tag{2.4}$$

In the case of the Sun, we have: 26 minutes $\ll 10^7$ years $\ll 10^{10}$ years respectively.

2.1.2 Eulerian and Lagrangian formalisms

Two distinct formalisms are commonly introduced in stellar hydrodynamics. In the *Eulerian* formalism, the evolution of a quantity X is studied at a **fixed** point in space. In spherical coordinates, this quantity is therefore described as $X(r, \theta, \phi, t)$, where r is the radial distance to the centre of the referential, θ is the polar angle, ϕ is the azimuthal angle and t is the time. This coordinate system is therefore independent of the movement of the particles. As such, the Eulerian formalism is preferred when following changes of state or variation in chemical composition.

In the *Lagrangian* formalism, a system of coordinates is associated to each material element of the fluid, **following their motion**. The quantity X therefore evolves as the fluid flows over time. One must therefore provide initial conditions $X(r_0, \theta_0, \phi_0, t_0)$, given here in spherical coordinates. As the coordinate systems *move* with the particles, this formalism is well-suited to study the motion of the particles and the evolution of the physical conditions they experience along their motion.

Due to the fundamental difference between the two formalisms, the time derivative of a quantity differs in the two formalisms. It is therefore important to introduce different notations for the two types of derivatives. One notes $\partial/\partial t$ the partial time derivative in Eulerian coordinates. In Lagrangian coordinates, the variation of a quantity relative to time along the motion of the fluid is written D/Dt. The latter derivative is called the *material derivative.* For a quantity X, both derivatives are related through the relation:

$$\frac{DX}{Dt} = \frac{\partial X}{\partial t} + \nabla X \cdot \vec{v} \tag{2.5}$$

---

[2] Naturally, the nuclear time cannot be define for white dwarfs and neutron stars, in which no stable fusion takes place.

2.1.3 Stellar dynamical equations

In stellar astrophysics, the dynamics of stars is governed by a set of fundamental stellar dynamical equations derived from fluid dynamics and thermodynamics. These equations describe notably mass conservation, momentum conservation, energy transport, and the behaviour of radiation within a star. Building upon the above formalisms and using the physical quantities introduced in Section 1.3, we have:

Conservation of mass or *continuity equation*:

$$\frac{D\rho}{Dt} + \rho\nabla \cdot \vec{v} = \frac{\partial \rho}{\partial t} + \nabla \cdot (\rho \vec{v}) = 0 \tag{2.6}$$

Conservation of momentum:

$$\frac{D\vec{v}}{Dt} = \frac{\partial \vec{v}}{\partial t} + \vec{v} \cdot \nabla \vec{v} = -\nabla\psi - \frac{\nabla P}{\rho} \tag{2.7}$$

Poisson equation:

$$\nabla^2 \psi_0 = 4\pi G \rho_0 \tag{2.8}$$

Conservation of energy:

$$T\frac{Ds}{Dt} = \frac{Du}{Dt} + P\frac{Dv}{Dt} = \epsilon - \frac{\nabla \cdot \vec{F}}{\rho} = \epsilon - \frac{d\delta L}{dm} \tag{2.9}$$

Transport of energy by radiation:

$$\vec{F}_R = -\frac{4acT^3}{3\kappa\rho}\nabla T \tag{2.10}$$

2.2 Small perturbation theory

Stellar oscillations will be studied in the framework of the small perturbation theory. We will study the evolution of the system starting from an initial state only slightly differing from the equilibrium state. As such, each state quantity is said to be *perturbed.* Eulerian perturbations differ from Lagrangian perturbations but are not unrelated. If we write X' for the Eulerian perturbation of the quantity X, and δX for the Lagrangian perturbation of the same quantity X, the two perturbed quantities are related through:

$$\delta X(\vec{r}_0, t) = X'(\vec{r}_0, t) + \nabla X(\vec{r}_0, t) \cdot \delta\vec{r}(\vec{r}_0, t) + \mathcal{O}(X'^2) \tag{2.11}$$

This relation therefore allows to express an equation with perturbed quantities in one formalism or the other, which can be very useful when developing equations.[3] Indeed, some mathematical simplifications are more straightforward in one formalism than the other and vice-versa. For example, $(\nabla X)' = \nabla(X')$ while $\delta(\nabla X) \neq \nabla(\delta X)$. Therefore, the Eulerian formalism is more convenient when working with gradients. However, it is

---

[3] Note that the above equation is obtained through a Taylor expansion limited to the first order, underlying the importance of only considering *small* perturbations.

the opposite for time derivatives since

$$\delta\left(\frac{DX}{Dt}\right)=\frac{\partial(\delta X)}{\partial t}\quad\text{while}\quad\left(\frac{DX}{Dt}\right)'\neq\frac{\partial(X)'}{\partial t}$$

In the following, considering small perturbations we will allow us to *linearise* the dynamical equations and significantly simplify the study of stellar oscillations.

2.3 Perturbed dynamical equations

Using the small perturbation theory and the two formalisms described above, we will now linearise the dynamical equations of Section 2.1.3. The *perturbed dynamical equations* that will be obtained are the basic equations used to describe stellar oscillations. Depending on the equation, we may prefer to work with either of the two formalisms in light of the examples given above. Note that we shall begin by considering **adiabatic** oscillations only. In other words, we do not take into account any exchange of energy over the timescale of the oscillations. For most stars, the adiabatic treatment yields results that are very close to the more elaborate non-adiabatic models. Actually, oscillations are close to perfectly adiabatic in most of the stars' interior. As mentioned previously, oscillation modes—in particular of low order—have periods of the order of the dynamical time, much shorter than the thermal timescale, further justifying the adiabatic approximation. This hypothesis will be revised in Section 2.7.

In order to obtain the perturbed equation of conservation of mass, we will work in the Lagrangian formalism:

$$\frac{D\rho}{Dt}+\rho\nabla\cdot\vec{v}=0 \tag{2.12}$$

By definition of the velocity, we have:

$$\begin{aligned}\vec{v}&=\frac{D\vec{r}}{Dt}=\frac{D(\vec{r}_0+\delta\vec{r})}{Dt} &(2.13)\\ &=\frac{D\vec{r}_0}{Dt}+\frac{D\delta\vec{r}}{Dt}=\frac{D\delta\vec{r}}{Dt}\approx\frac{\partial\delta\vec{r}}{\partial t} &(2.14)\end{aligned}$$

Where the last equality is valid to first order. Hence, the conservation of mass becomes:

$$\begin{aligned}\frac{D\rho}{Dt}+\rho\nabla\cdot\vec{v}&=\frac{D\rho}{Dt}+\rho\nabla\cdot\left(\frac{\partial\delta\vec{r}}{\partial t}\right)=\frac{D\rho}{Dt}+\rho\frac{\partial}{\partial t}\left(\nabla\cdot\delta\vec{r}\right) &(2.15)\\ &\approx\frac{D\rho}{Dt}+\rho\frac{D}{Dt}\left(\nabla\cdot\delta\vec{r}\right)=0 &(2.16)\end{aligned}$$

The two terms of this equation can then be integrated to yield an integrated form of the continuity equation that can be expressed in the Eulerian formalism:

$$\boxed{\frac{\delta\rho}{\rho}=-\nabla\cdot\delta\vec{r}\quad\Leftrightarrow\quad\rho'=-\nabla\cdot(\rho\delta\vec{r})} \tag{2.17}$$

For the conservation of momentum (Eq. (2.7)), let us consider an equilibrium configuration:

$$\left(\frac{D\vec{v}}{Dt}\right)_0 = 0 \quad \Rightarrow \quad \nabla\psi_0 + \frac{\nabla P_0}{\rho_0} = 0 \tag{2.18}$$

We can also make an approximation similarly to Eq. (2.14):

$$\frac{D\vec{v}}{Dt} \approx \frac{\partial^2 \delta\vec{r}}{\partial t^2} \tag{2.19}$$

Let us now take the difference between the instantaneous expression of the momentum equation and its equilibrium expression. We have:

$$\begin{aligned} \frac{\partial^2 \delta\vec{r}}{\partial t^2} - 0 &= -\nabla\psi - \frac{\nabla P}{\rho} + \nabla\psi_0 + \frac{\nabla P_0}{\rho_0} && (2.20)\\ &= (\nabla\psi_0 - \nabla\psi) + \left(\frac{\nabla P_0}{\rho_0} - \frac{\nabla P}{\rho}\right) && (2.21)\\ &= -\left(\nabla\psi\right)' - \left(\frac{\nabla P}{\rho}\right)' && (2.22) \end{aligned}$$

The term $(\nabla P/\rho)'$ can be seen as the Eulerian perturbation of the function $1/\bullet$. The Eulerian perturbation of a function $f(X)$ is:

$$(f(X))' \approx \frac{df}{dX} X' \tag{2.23}$$

This yield the following expression for the Eulerian perturbation of the conservation momentum:

$$\boxed{\frac{\partial^2 \delta\vec{r}}{\partial t^2} = \nabla\psi' - \frac{\nabla P'}{\rho} + \frac{\rho'}{\rho^2}\nabla P} \tag{2.24}$$

At equilibrium, Poisson's equation yields:

$$\nabla^2\psi_0 = 4\pi G\rho_0 \quad \Rightarrow \quad \nabla^2\psi_0 - 4\pi G\rho_0 = 0 \tag{2.25}$$

Therefore if we consider Poisson's equation with a small Eulerian perturbation of the physical quantities, we obtain:

$$\begin{aligned} \nabla^2(\psi_0 + \psi') &= 4\pi G(\rho_0 + \rho') && (2.26)\\ \Leftrightarrow \ \nabla^2\psi_0 - 4\pi G\rho_0 &= 4\pi G\rho' - \nabla^2\psi' && (2.27) \end{aligned}$$

$$\boxed{\Rightarrow \ \nabla^2\psi' = 4\pi G\rho'} \tag{2.28}$$

The last basic dynamical equation that should be expressed in terms of small perturbations in order to describe adiabatic oscillations is the equation of the *adiabatic expansion* of a gas. In thermodynamic, the adiabatic relation between pressure and density variation is given by:

$$\frac{d\ln P}{d\ln\rho} = \left.\frac{\partial \ln P}{\partial \ln \rho}\right|_S \equiv \Gamma_1 \tag{2.29}$$

For a Lagrangian perturbation, we have $\delta(\ln X) \approx \delta X/X$. Hence,

$$\frac{\delta P}{P} \approx \delta(\ln P) = \frac{d\ln P}{d\ln\rho}\delta(\ln\rho) = \Gamma_1\frac{\delta\rho}{\rho} \tag{2.30}$$

and we can therefore write

$$\boxed{\frac{\delta P}{P} = \Gamma_1\frac{\delta\rho}{\rho}} \tag{2.31}$$

which is the perturbed adiabatic relation.

Summary of perturbed dynamical equations

We have therefore obtained the 4 dynamical equations that will be used further to describe *adiabatic oscillations*:

Conservation of mass:

$$\frac{\delta\rho}{\rho} = -\nabla\cdot\delta\vec{r} \tag{2.32}$$

Conservation of momentum:

$$\frac{\partial^2\delta\vec{r}}{\partial t^2} = \nabla\psi' - \frac{\nabla P'}{\rho} + \frac{\rho'}{\rho^2}\nabla P \tag{2.33}$$

Poisson equation:

$$\nabla^2\psi' = 4\pi G\rho' \tag{2.34}$$

Adiabatic relation:

$$\frac{\delta P}{P} = \Gamma_1\frac{\delta\rho}{\rho} \tag{2.35}$$

Thanks to the small perturbation approximation, the above equations are **linear** in the perturbations, which will simplify some of the calculations.

2.4 Radial adiabatic oscillations

Radial oscillations are the simplest stellar oscillations. These modes are *spherically symmetric*. They can be classified in terms of their number of radial nodes. The first radial mode therefore as no node and corresponds to the simultaneous contraction and expansion of each layer of the star. The following mode has one node. When the outer layers of the stars contact, the inner layers expand and vice-versa. The subsequent modes follow the exact same logic with increasingly more nodes. In this section, we will present how radial adiabatic oscillations can be obtained from the dynamical equations for an unperturbed, non-rotating, spherically symmetric star in an equilibrium configuration.

In the following, we will show that the dynamical equations (2.32) to (2.35) form a system of four differential equations that can be projected radially and expressed as a *Sturm-Liouville problem* of the form:

$$\frac{d}{dx}\left(p(x)\frac{du}{dx}\right) + \left[q(x) + \lambda\rho(x)\right]u(x) = 0 \tag{2.36}$$

with homogeneous or periodic boundary conditions.

Since the problem is spherically symmetric, we work in spherical coordinates. From the spherical symmetry, we can suppose that an element of the star oscillates as:

$$\delta\vec{r} = \delta r(r)\sin(\sigma t)\vec{e}_r \tag{2.37}$$

where σ is unknown. The pressure and density vary similarly and can be expressed as $P' = P'(r)\sin(\sigma t)$ and $\rho' = \rho'(r)\sin(\sigma t)$. Since the problem is symmetric, we do not have to consider the angular components of the vectors. Hence, from the expression of the divergence of a vector in spherical coordinates, we have for the conservation of mass:

$$\frac{\delta\rho}{\rho} = -\nabla\cdot\delta\vec{r} = -\frac{1}{r^2}\frac{d(r^2\delta r)}{dr} \tag{2.38}$$

From Eq. (2.37) and the conservation of momentum, we have:

$$\frac{\partial^2\delta r}{\partial t^2} = -\sigma^2\delta r = -\delta\left(\nabla\psi + \frac{\nabla P}{\rho}\right) \tag{2.39}$$

We can then use Eq. (1.11) to express the derivative of the pressure in terms of the mass. We also use the expression of the gravitational potential to compute its derivative:

$$\begin{aligned} -\sigma^2\delta r &= -\delta\left(\frac{Gm}{r^2} + 4\pi r^2\frac{\partial P}{\partial m}\right) && (2.40)\\ &= 2\frac{Gm}{r^2}\frac{\delta r}{r} - 8\pi r^2\frac{\partial P}{\partial m}\frac{\delta r}{r} - 4\pi r^2\frac{\partial P}{\partial m} && (2.41)\end{aligned}$$

Using again Eq. (1.11), we can re-express the mass derivatives:

$$-\sigma^2\delta r = 2\frac{Gm}{r^2}\frac{\delta r}{r} - \frac{2}{\rho}\frac{\partial P}{\partial r}\frac{\delta r}{r} - \frac{1}{\rho}\frac{\partial\delta P}{\partial r} \tag{2.42}$$

From the hydrostatic equilibrium (Eq. (1.13)) and introducing $g = Gm/r^2$, we obtain:

$$-\sigma^2\delta r = 4g\frac{\delta r}{r} - \frac{1}{\rho}\frac{\partial\delta P}{\partial r} \tag{2.43}$$

We can then make use of the adiabatic relation (Eq. (2.35)) and Eq. (2.38). Indeed, we have:

$$\delta P = \Gamma_1 \left(\frac{\delta\rho}{\rho}\right) P = \Gamma_1 \left(\frac{-1}{r^2}\frac{\partial(r^2\delta r)}{\partial r}\right) P \tag{2.44}$$

Injecting this result in Eq. (2.43) and developing the derivative, one obtains:

$$\begin{aligned} -\sigma^2\delta r &= 4g\frac{\delta r}{r} - \frac{1}{\rho}\frac{d}{dr}\left(\frac{\Gamma_1 P}{r^2}\frac{d(r^2\delta r)}{dr}\right) && (2.45)\\ &= 4g\frac{\delta r}{r} + \frac{\Gamma_1 P r}{\rho}\frac{d^2}{dr^2}\left(\frac{\delta r}{r}\right) + \frac{1}{\rho r^3}\frac{d}{dr}\left(r^4\Gamma_1 P\right)\frac{d}{dr}\left(\frac{\delta r}{r}\right) + \frac{3}{\rho}\frac{d(\Gamma_1 P)}{dr}\frac{\delta r}{r} && (2.46)\end{aligned}$$

Finally, by introducing the notation $\xi = \delta r/r$, this relation can be cast into the form of Eq. (2.36) as

$$\frac{d}{dr}\left(r^4\Gamma_1 P\frac{d\xi}{dr}\right) + \left[r^3\frac{d}{dr}\left((3\Gamma_1 - 4)P\right) + \sigma^2\rho r^4\right]\xi = 0 \tag{2.47}$$

Sturm-Liouville problems are eigenvalue problems, with σ^2 representing the eigenvalues in this context. Such problems possess several notable properties:

- The eigenvalues are real and form an ordered, countable, infinite set of frequencies: $\sigma_0^2 < \sigma_1^2 < ...$, with $\sigma_n^2 \to \infty$ when $n \to \infty$.
- The oscillation nodes of the eigenfunctions ξ_n are interlaced. This means that between every node of ξ_n, there will always be a node of ξ_{n+1}. The eigenfunction of order $n = 0$ is the lowest order mode. It does not have any node between $0 < r < R$. This mode is called the *fundamental mode.*

Solving Eq. (2.47) numerically in the adiabatic approximation yields the squared frequencies σ^2 of the star's radial oscillation modes. Remarkably, the frequencies obtained from the adiabatic development are very close to those that can be derived from a non-adiabatic analysis. They can therefore serve as initial estimates for non-adiabatic algorithms to converge towards more refined values.

It is important to note, however, that an adiabatic treatment cannot accurately determine the eigenfunctions in the stars' outer non-adiabatic layers. In these regions, a full non-adiabatic approach, which accounts for energy exchange processes, is required. The non-adiabatic case is presented in Section 2.7.

Finally, the adiabatic treatment can provide some information on the *dynamical stability* of the star, which should not be confused with the *stability of the oscillation modes.* The former gives information on the star's overall response to perturbations—its behaviour under compression or expansion—and indicates whether it is likely to maintain equilibrium or collapse. The latter, directly related to the non-adiabatic case as presented above, provides information on which modes are likely to be amplified and become observable, and which will be damped. Further developments on dynamical stability, as derived from the adiabatic treatment of radial oscillations, are provided in Appendix A.

2.5 Non-radial adiabatic oscillation modes

Radial oscillations is only a small fraction of the vast variety of oscillation modes that can exist for a star. Still considering an unperturbed, non-rotating, spherically symmetric star in an equilibrium configuration, one can also compute *non-radial adiabatic* oscillation modes. These modes create a rich spectrum of oscillations and are key to the probing of the star's interior.

As the oscillations are no longer spherically symmetric, we must fully work in spherical coordinates. The dynamical equations can be re-written accordingly and projected along the different axis. We obtain a system of partial derivative equations:

$$\frac{\partial \psi'}{\partial r} + \frac{\rho'}{\rho}\frac{Gm}{r^2} + \frac{1}{\rho}\frac{\partial P'}{\partial r} = \sigma^2 \xi_r \tag{2.48}$$

$$\frac{\delta\rho}{\rho} + \frac{1}{r^2}\frac{\partial}{\partial r}\left(r^2\xi_r\right) - \frac{1}{\sigma^2 r^2}\mathcal{L}^2\left(\psi' + \frac{P'}{\rho}\right) = 0 \tag{2.49}$$

$$\frac{1}{r^2}\frac{\partial}{\partial r}\left(r^2\frac{\partial \psi'}{\partial r}\right) - \frac{1}{r^2}\mathcal{L}^2\psi' = 4\pi G\rho' \tag{2.50}$$

where $\mathcal{L}^2$ is a linear operator called the *Legendrian* and is defined as

$$\mathcal{L}^2 = -r^2\nabla_h^2 = -\frac{1}{\sin\theta}\frac{\partial}{\partial\theta}\left(\sin\theta\frac{\partial}{\partial\theta}\right) - \frac{1}{\sin^2\theta}\frac{\partial^2}{\partial\phi^2}\,. \tag{2.51}$$

Eq. (2.48) is obtained from the radial component of the conservation of momentum, Eq. (2.49) is obtained from the horizontal (θ, ϕ) components of the conservation of momentum and from the conservation of mass, and Eq. (2.50) is obtained from Poisson's equation.

Solving this system of equations directly would be very computationally expensive. However, this problem can be simplified without any approximation by using *variable separation* and searching for solutions of the form: $X'(r,\theta,\phi,t) = X'(r)F(\theta,\phi)\cos(\sigma t)$. This is possible as the derivatives relative to θ and ϕ only appear in the operator $\mathcal{L}^2$, and as the other derivatives in Eq. (2.48) to (2.50) only imply r.

The eigenfunctions of the Legendrian operator are called the *spherical harmonics* and written $Y_l^m(\theta,\phi)$. We have

$$\mathcal{L}^2 Y_l^m(\theta,\phi) = l(l+1)Y_l^m(\theta,\phi)\,. \tag{2.52}$$

Hence the problem reduces to solving a system of fourth-order ordinary differential equations in r. The spherical harmonics Y_l^m can be defined in terms of the *associated Legendre polynomials* P_l^m as

$$Y_l^m(\theta,\phi_0) = NP_l^m(\cos\theta)e^{im\phi}, \tag{2.53}$$

where N is a normalisation coefficient.

We therefore know that the behaviour of the angular part of non-radial oscillations is governed by the spherical harmonics $Y_l^m(\theta, \phi)$. Non-radial modes are hence characterised by the two parameters m and l. These values are related to the number of nodal lines, on which there is no displacement of mass: $|m|$ gives the number of meridional nodal lines[4], directly related to the periodicity of $e^{im\phi}$ in Eq. (2.53), and l gives the total number of nodal lines. The number of equatorial nodal lines is therefore given by $(l - |m|)$, which corresponds to the number of zeros of the associated Legendre polynomial P_l^m. Radial modes are thus the $m = 0$, $l = 0$ modes, for which there is no nodal line on the surface. The sign of m can either be positive or negative, depending on the direction of the motion of the wave relative to the rotation of the star:

- *Prograde modes* $(m < 0)$ travel in the same direction as the star's rotation.
- *Retrograde modes* $(m > 0)$ travel in the opposite direction to the star's rotation.

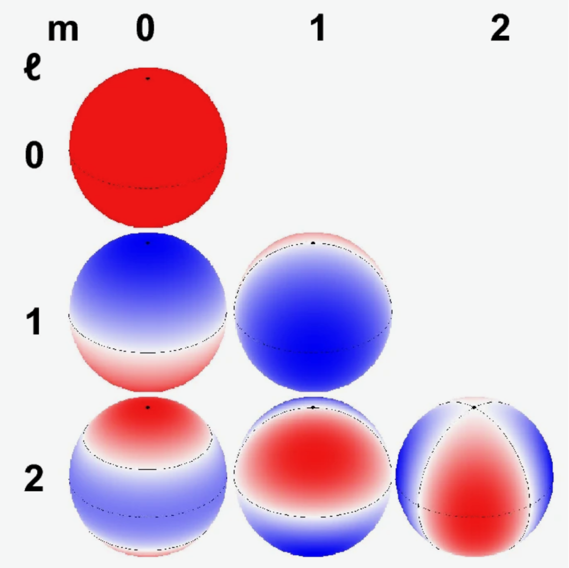

Figure 2.1: Visualisation of different non-radial oscillation modes. Credit: García & Ballot (2019)

Solving the remaining problem will yield solutions for r and allow to characterise modes by their number of radial nodes. To simplify the problem, one can use the Cowling approximation, which neglects the perturbation of the gravitational potential $(\psi' = 0)$. This approximation is particularly well justified for modes with a large number of radial nodes, where the influence of the potential perturbation on the oscillation frequencies is minimal. Under this approximation, the equation to solve is:

$$\frac{d^2\bar{\xi}_r}{dr^2} + k(r)^2\bar{\xi}_r \simeq 0, \quad k(r)^2 = \frac{1}{c^2(r)}\left(1 - \frac{L_l^2}{\sigma^2}\right)\left(\sigma^2 - N^2\right) \tag{2.54}$$

with

$$\bar{\xi}_r \equiv \frac{\rho^{1/2} r c}{\left|L_l^2/\sigma^2 - 1\right|^{1/2}}\xi_r \tag{2.55}$$

---

[4] One meridional line circles the star by crossing its poles.

and where we introduced the *Brunt-Vaïsälä frequency* N defined as

$$N^2 = \frac{Gm}{r^2}\left(\frac{1}{\Gamma_1}\frac{d\ln P}{dr} - \frac{d\ln \rho}{dr}\right) \simeq \frac{\rho g^2}{P}\left(\nabla_{\rm ad} - \nabla + \nabla_\mu\right) \tag{2.56}$$

and the *Lamb frequency* L_l defined as

$$L_l^2 = \frac{l(l+1)c^2}{r^2}\,. \tag{2.57}$$

Eq. (2.54) is a wave equation if $k^2 > 0$. This condition is fulfilled in two cases which defines two families of oscillations:

- $\sigma^2 > N^2$ and $\sigma^2 > L_l^2$: the restoring force is the pressure, the oscillations are called *pressure modes.*
- $\sigma^2 < N^2$ and $\sigma^2 < L_l^2$: the restoring force is the buoyancy, the oscillations are called *gravity modes.*

Regions where $k^2 > 0$ are called *propagation cavities*, in opposition to *evanescent zones* where $k^2 < 0$.

Analytical solutions to Eq. (2.54) can be obtained using the *JWKB approximation.* This method assumes that the characteristic length scale over which the star's structure—and hence the wave number k—varies is much larger than the wavelength of the oscillation modes. Consequently, the wave equation can be expressed in terms of oscillatory or exponential functions. Under this approximation, we obtain in propagation cavities:

$$\bar{\xi}_r(r) \simeq \frac{A}{k(r)^{1/2}}\cos\left(\int k(r)dr\right) \tag{2.58}$$

where A is the amplitude of the oscillation.

Pressure modes predominantly propagate in the outer layers of nuclear-burning stars. They form a discrete infinity of frequencies tending towards infinity for each l. These modes are comparable to acoustic standing waves. At high frequencies, ($\sigma^2 \gg L_l^2, N^2$), we have:

$$k^2(r) \simeq \frac{\sigma^2}{c^2(r)} \quad \Rightarrow \quad \frac{d^2\bar{\xi}_r}{dr^2} + \frac{\sigma^2}{c^2(r)}\bar{\xi}_r \simeq 0 \tag{2.59}$$

Hence, their spectrum mainly depends on the sound speed profile, which is given inside of stars by

$$c^2(r) = \frac{P(r)\Gamma_1}{\rho(r)} \propto \frac{\Gamma_1 T(r)}{\mu(r)} \tag{2.60}$$

Within the JWKB approximation, pressure modes are approximately evenly spaced in frequency, with a separation given by

$$\Delta\nu_{n,l} = \nu_{n,l} - \nu_{n-1,l} \approx \text{constant} \tag{2.61}$$

This quantity, known as the *large separation*, is inversely proportional to the dynamical timescale of the star and provides a direct measure of the mean density. A more refined analysis reveals a second frequency spacing, the *small separation*, defined as

$$\delta\nu_{n,l} = \nu_{n,l} - \nu_{n-1,l+2} \tag{2.62}$$

Both the large and small separations are sensitive to the internal structure and composition of the star, making pressure modes powerful probes of stellar interiors.

Gravity modes are found in the deep, dense layers of nuclear-burning stars, where buoyancy acts as the restoring force. They form a discrete, infinite sequence of frequencies tending towards zero as l increases. At low frequencies ($\sigma^2 \ll L_l^2, N^2$), gravity modes are evenly spaced in *period.* In these conditions, the wave number k can be approximated as:

$$k(r)^2 \simeq \frac{l(l+1)}{\sigma^2 r^2} N^2 \tag{2.63}$$

Hence, the spectrum of gravity modes mainly depends on the Brunt-Vaïsälä frequency $N(r)$. A more refined analysis reveals deviations from a perfectly constant spacing due to structural changes in the core. These deviations contain valuable information about *core rotation*, *mixing processes*, and the presence of a convective core in earlier evolutionary stages. In white dwarfs, these period-spacing variations arise from the partial reflection of waves at sharp chemical composition transitions (see Figure 1.3).

Because white dwarfs possess a fundamentally different internal structure than nuclear-burning stars, their oscillation modes propagate differently. Figure 2.2, reproduced from Fontaine & Brassard (2008), illustrates the propagation cavities of three families of pulsating white dwarfs as well as for the Sun. In white dwarfs, gravity modes dominate and propagate through the outer layers. Although pressure modes are theoretically possible in these regions, they have never been observed in white dwarfs. Hence, we will restrict our computations to gravity modes in our codes.

As a final note, in evolved stars—particularly in red giants—pressure and gravity modes can couple, leading to *mixed modes.* These modes have a more complicated spectrum and allow for the simultaneous probing of both regions.

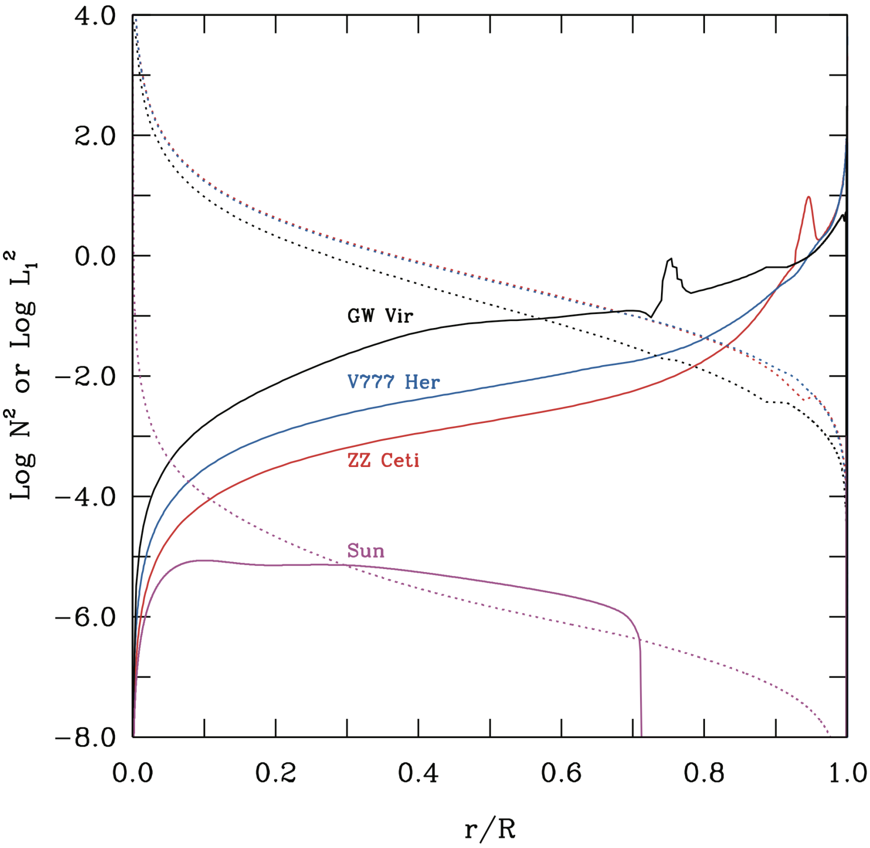

Figure 2.2: Propagation diagram for (1) a solar model (*magenta curves*), (2) a GW Vir star model (*black curves*), (3) a V777 Her star model (*blue curves*), and (4) a ZZ Ceti model (*red curves*). For each model, the profile of the logarithm of the square of the Brunt-Väisälä frequency (solid curve) and that of the logarithm of the square of the Lamb frequency for modes with $l = 1$ (*dotted curve*) are shown as functions of the normalized radius. The well in the Brunt-Väisälä frequency for the solar model corresponds to the outer convection zone, while the peak structure seen in both the GW Vir and the ZZ Ceti curves is associated with a composition transition zone. The three white dwarf models all have a mass of $M = 0.6M_\odot$. Figure and caption reproduced from: Fontaine & Brassard (2008).

2.6 Effect of rotation on oscillation modes

Accounting for the effect of rotation significantly complicates the computation of oscillation modes. Rotation breaks the spherical symmetry at equilibrium of the star, on which the previous developments relied. In particular, for sufficiently fast rotation, stars can show a non-negligible flattening. When working in a corotating frame, two additional fictitious forces must be considered: the centrifugal and Coriolis forces. Including all these effects in the oscillation equations leads to complicated partial differential equations that are difficult to solve numerically and impossible to solve analytically.

In first approximation, one can entirely neglect the centrifugal and Coriolis force and consider a star in rigid rotation. We simply consider the previously derived oscillations in a corotating frame. If we have an inertial frame of reference with the spherical coordinates (r, θ, ϕ), we have in the corotating frame:

$$(r', \theta', \phi') = (r, \theta, \phi - \Omega t)$$

with Ω the angular frequency of rotation of the star. If we write σ_0 for the frequencies computed for a non-rotating star, we can write the solutions in this corotating frame of reference similarly as in the non-rotating case:

$$X'(r, \theta, \phi', t) = X'(r) \operatorname{Re}\left\{Y_l^m(\theta, \phi') \exp(i\sigma_0 t)\right\} \tag{2.64}$$

We can then re-express them in the inertial frame of reference, which yields:

$$X'(r, \theta, \phi, t) = X'(r) \operatorname{Re}\{Y_l^m(\theta, \phi - \Omega t) \exp(i\sigma_0 t)\} \tag{2.65}$$

We can re-express the spherical harmonics Y_l^m using the Legendre polynomials through the relation:

$$Y_l^m(\theta, \phi_0) = P_l^{|m|}(\cos\theta) e^{im\phi_0} \,. \tag{2.66}$$

We therefore have:

$$X'(r, \theta, \phi', t) = X'(r) \operatorname{Re}\left\{P_l^{|m|}(\cos\theta) \exp(i(m(\phi - \Omega t) + \sigma_0 t))\right\} \tag{2.67}$$

$$= X'(r) P_l^{|m|}(\cos\theta) \cos(m\phi + (\sigma_0 - m\Omega)t) \,. \tag{2.68}$$

The frequencies measured from an inertial observer's point of view are therefore $\sigma_m = (\sigma_0 - m\Omega)$. This is actually a remarkable result as just by considering the rotation of the star's frame of reference, the observed frequencies become dependent on m. This *rotational splitting* of the modes can therefore serve as a measure of rotation.

So far, we have not considered the effect of the centrifugal and Coriolis forces. To obtain some analytical solutions, the *traditional approximation* is often introduced to reduce the mathematical complexity. This approximation neglects the deformation of the star due to the centrifugal force and assumes a uniformly rotating star.

In the following, we consider a new family of oscillations, the *gravito-inertial modes*, for which both buoyancy and the Coriolis force act as restoring forces. Accounting for the Coriolis force, the equation of motion is given by:

$$\frac{\partial^2 \delta\vec{r}}{\partial t^2} = -\nabla\psi' - \frac{\nabla P'}{\rho} + \frac{\rho'}{\rho^2}\nabla P - 2i\sigma_c \vec{\Omega} \times \delta\vec{r} \,, \tag{2.69}$$

where σ_c is the frequency of the oscillation mode in the corotating frame.

The traditional approximation applies to low-frequency gravito-inertial modes in stellar regions where buoyancy dominates over the Coriolis force in radial direction. Mathematically, this requires both the wave frequency and the rotation frequency to be much smaller than the Brunt-Väisälä frequency in the propagation region. Under these conditions, one may neglect both the radial component of the Coriolis acceleration and the influence of the radial motion on the Coriolis force. Consequently, the wave motion is treated as nearly horizontal, simplifying the analysis of gravito-inertial modes in strongly stratified layers or rotating stars.

Under the traditional approximation, the problem becomes separable again. The spatial dependence of any perturbed quantity can be separated as:

$$X'(r,\theta,\phi) = X'(r)\,\Theta_\nu(\mu)\,e^{im\phi}\,, \tag{2.70}$$

where $\mu = \cos\theta$. The linear operator acting on $\Theta_\nu(\mu)$ is the *Laplace tidal operator* defined as:

$$\begin{aligned}\mathcal{L}_\nu\left[\Theta_\nu(\mu)\right] &\equiv -\frac{d}{d\mu}\left[\frac{1-\mu^2}{1-\nu^2\mu^2}\frac{d\Theta_\nu(\mu)}{d\mu}\right] + \frac{1}{1-\nu^2\mu^2}\left[\frac{m^2}{1-\mu^2} + m\nu\frac{1+\nu^2\mu^2}{1-\nu^2\mu^2}\right]\Theta_\nu(\mu)\\ &= \lambda\,\Theta_\nu(\mu)\,.\end{aligned} \tag{2.71}$$

The eigenfunctions of this operator are the *Hough functions* $\Theta_\nu(\mu)$, which play a similar role as the spherical harmonics in the non-rotating case. ν is called the *spin parameter*, defined as:

$$\nu \equiv \frac{2\Omega}{\sigma_c}\,. \tag{2.72}$$

As shown by Eq. (2.71) compared to Eq. (2.52), in the rotating case the eigenvalues of the Laplace tidal operator are no longer $l(l+1)$ but are replaced by λ. For typical gravito-inertial modes, λ tends towards infinity as the stellar rotation increases. However, there exists a particular group of modes, known as the *Kelvin modes* (the prograde modes with $m = -l$), for which λ asymptotically approaches a constant value as the rotation of the star increases. Moreover, there exist additional eigensolutions to the Laplace tidal operator that do not have counterparts in the non-rotating limit. These modes, which are primarily influenced by the Coriolis force, are known as the *Rossby modes*.

Overall, the physical interpretation of the modes remains analogous to that in the non-rotating case. In fact, when $\nu = 0$, the Laplace tidal operator reduces to the Legendre operator, and the resulting solutions coincide with the standard spherical harmonics obtained in the absence of rotation.

2.7 Non-adiabatic oscillations

As mentioned previously, oscillations remain close to adiabatic in most of the star's interior. The adiabatic approximation therefore yields relevant results while being significantly simpler than a full non-adiabatic treatment. In some situations, exchanges of energy can become significant in a part of the star during one oscillation cycle. The energy exchanges must therefore be taken into account to properly model the oscillations. This is the case in regions where the local thermal timescale becomes comparable or lower than the dynamical timescale ($t_{\mathrm{HK}} \lesssim t_{\mathrm{dyn}}$), which typically happens in the superficial regions of the stars where the heat exchanged per unit mass is of the same order as the internal energy:

$$|\Delta q| \simeq \left|\frac{dL}{dm}\right| t_{\mathrm{dyn}} \simeq u = c_v T \tag{2.73}$$

$$\Rightarrow \frac{|\Delta s|}{c_v} = \frac{|\Delta q|}{c_v T} \simeq 1 \tag{2.74}$$

To account for non-adiabatic processes, the equation of conservation of energy (Eq. (2.9)) and the equation of transport of energy by radiation (Eq. (2.10)) must be perturbed. These equations replace the perturbed adiabatic relation (Eq. (2.35)) used in the adiabatic treatment. To reduce the complexity of the developments, we limit ourselves to **radial non-adiabatic oscillations**. Using the conservation of mass, the perturbed equation of transport of energy by radiation can be written as:

$$\frac{\delta L}{L} = -\frac{\delta\kappa}{\kappa} + 4\frac{\delta r}{r} + 3\frac{\delta T}{T} + \frac{d\delta T/dm}{dT/dm} \tag{2.75}$$

Assuming the entropy varies as $\delta s = \delta s \cdot e^{i\sigma t}$, we have for the conservation of energy:

$$\left.\begin{aligned} \delta\left(T\frac{Ds}{Dt}\right) &= T\frac{D\delta s}{Dt} = T\frac{\partial \delta s}{\partial t} = i\sigma T\delta s \\ \delta\left(\epsilon - \frac{d\delta L}{dm}\right) &= \delta\epsilon - \frac{d\delta L}{dm} \end{aligned}\right\} \quad \Rightarrow \quad i\sigma T\delta s = \delta\epsilon - \frac{d\delta L}{dm} \tag{2.76}$$

This result has an important consequence. Since the left-hand side of Eq. (2.76) has an imaginary part, we shall now consider complex solution to the problem:

$$\begin{aligned} \delta X(r,t) &= \mathrm{Re}\left\{\delta X(r)e^{i\sigma t}\right\} \\ &= |\delta X(r)|\cos(\sigma_R t + \phi(r))e^{\eta t} \end{aligned} \tag{2.77}$$

where η denotes the mode's growth rate and $\phi(r)$ the phase of the considered quantity. The sign of η determines the stability of the mode. It shows whether a mode is excited (and thus observed) or damped. Moreover, the presence of $\phi(r)$ implies that phase shifts may occur between various physical quantities, providing additional means to compare theoretical predictions with observations.

This set of equations must be completed by equations of state from thermodynamics:

$$\rho = \rho(P, s) \implies \frac{\delta\rho}{\rho} = \left.\frac{\partial \ln \rho}{\partial \ln P}\right|_s \frac{\delta P}{P} + \left.\frac{\partial \ln \rho}{\partial \ln s}\right|_P \delta s = \frac{1}{\Gamma_1}\frac{\delta P}{P} - \frac{\nabla_{\rm ad}\rho T}{P}\delta s \tag{2.78}$$

$$T = T(P, s) \implies \frac{\delta T}{T} = \left.\frac{\partial \ln T}{\partial \ln P}\right|_s \frac{\delta P}{P} + \left.\frac{\partial \ln T}{\partial \ln s}\right|_P \delta s = \nabla_{\rm ad}\frac{\delta P}{P} + \frac{\delta s}{c_p} \tag{2.79}$$

$$\kappa = \kappa(\rho, T) \implies \frac{\delta\kappa}{\kappa} = \left.\frac{\partial \ln \kappa}{\partial \ln \rho}\right|_T \frac{\delta \rho}{\rho} + \left.\frac{\partial \ln \kappa}{\partial \ln T}\right|_\rho \frac{\delta T}{T} = \kappa_\rho\frac{\delta \rho}{\rho} + \kappa_T\frac{\delta T}{T}. \tag{2.80}$$

These equations typically admit only numerical solutions. For white dwarfs, their values are therefore tabulated within evolutionary codes.

Finally, while the nuclear timescale defined in Eq. (2.3) always remains much larger than both $t_{\rm dyn}$ and $t_{\rm HK}$, it is important to note that the characteristic times associated with intermediate reactions can vary significantly. For example, the characteristic timescale of deuterium burning is of the order of $\sim 1\,$s (much smaller than typical oscillation timescales), whereas ^{3}He burning takes much longer than the dynamical time. Consequently, the variation in the abundance of the different nuclei depends on the oscillation period:

$$\frac{\delta\epsilon}{\epsilon} = \epsilon_\rho(\rho, T, \sigma)\frac{\delta\rho}{\rho} + \epsilon_T(\rho, T, \sigma)\frac{\delta T}{T} \tag{2.81}$$

For white dwarfs, this aspect is naturally absent as no nuclear burning occurs.

Non-adiabatic processes can excite oscillation modes through mechanisms such as the κ mechanism. In a layer where the opacity κ peaks—typically in a partial ionisation zone—compression raises κ above its equilibrium value, trapping radiation and building up thermal energy during the so-called *hot phase.* As the layer subsequently expands, κ falls below the peak, allowing that energy to escape during the *cold phase.* If the layer's thermal time $t_{\rm HK}$ is comparable to the oscillation period, this heat-trapping and release form a thermodynamic cycle—similarly to a heat engine—that converts thermal energy into mechanical work and drives the oscillations. The κ mechanism is responsible for the pulsation instabilities observed in classical Cepheids, δ Scuti stars, and some other variable stars shown in Figure 1.4.

The mechanism driving ZZ Ceti pulsations is known as *convective driving* (Brickhill, 1991). Once the white dwarf cools into the ZZ Ceti instability strip, a convection zone forms in its outer layers, driven by hydrogen ionization. This opaque zone traps heat during compression and releases it during expansion. The resulting phase lag between heat build-up and release provides the net driving that sustains the oscillations.

As an oscillation mode propagates through the star, it therefore creates variations of energy. The energy of a mode is given by

$$E = \frac{\sigma^2}{2}\int_0^M \delta r(r)^2 dm, \tag{2.82}$$

where we integrate over the full volume. Over a complete oscillation cycle, the global work performed is

$$W = -\pi \int_0^M \mathrm{Im}\left\{ \frac{\delta P \overline{\delta \rho}}{\rho^2} \right\} dm. \tag{2.83}$$

Integrating the equation of motion multiplied by $\overline{\delta r} dm$ and taking the imaginary part, one obtains

$$\eta = \frac{dW/dt}{2E}. \tag{2.84}$$

If we replace the work and the total energy in this equation with the above expressions, we can separate the contribution of gas and turbulence to the pressure and apply the equation of conservation of energy. We can then separate further the contribution of radiation and convection, which yields:

$$\eta = -\frac{1}{2\sigma_R} \left[\int_0^M \mathrm{Re}\left\{ \frac{1}{\sigma} \frac{d(\delta L_R + \delta L_C)}{dm} \right\} + \int_0^M \mathrm{Im}\left\{ \frac{\delta P_{\mathrm{turb}} \overline{\delta \rho}}{\rho^2} \right\} dm \right] \Big/ \int_0^M |\delta r|^2 dm. \tag{2.85}$$

This equation shows the contribution to the work integral of radiation, convection and turbulent motion.

2.8 Effect of convection treatment on oscillations

Convection and pulsations are coupled in stars (Houdek & Dupret, 2015). Hence, a proper modelling of convection is essential to accurately compute oscillation modes. However, the treatment of convection is vast and complex, and in practice the results can be very model-dependent.

Various approaches exist to model convection, each with differing levels of complexity and accuracy. The most widely used method in stellar evolution and oscillation models is the *Mixing-Length Theory (MLT)*, which provides a simplified, local description of convective transport. Although MLT facilitates efficient computation, most treatments neglect important time-dependent effects that can be crucial for oscillations. Indeed, the typical timescale of convective flow can be of the same order as the oscillation timescale. To account for this coupling, a **time-dependent** version of mixing-length theory was developed by Grigahcène et al. (2005), which has shown promising results for δ Scuti and γ Doradus stars (Dupret et al., 2005). This is the time-dependent convection treatment that is used in this work.

Beyond time-dependent MLT, an alternative way to model the convection-pulsation coupling is through 3D hydrodynamic simulations, which inherently account for the full coupling between oscillations and convection. While early models were restricted to the superficial layers of stars (e.g. Nordlund & Stein 2001, Tremblay et al. 2015), more recent simulations are gradually extending to deeper stellar regions. Yet, despite these advancements, achieving full-star 3D simulations that accurately capture both convection and oscillations remains a significant computational challenge.

To illustrate the importance of the treatment of convection, we can compare the theoretical blue edge of ZZ Ceti computed by *frozen convection* MLT, which is *not* time-dependent, and the time-dependent convection MLT mentioned above. The former model predicted a blue edge at $\sim$ 11750 K, while the latter predicts a value of $\sim$ 11970 K, in closer agreement with empirical values of $\sim$ 12000 K. Figure 2.3 shows the distribution of the periods of excited modes of a white dwarf using both treatments of convection. While the blue edge given in these figures correspond well to the empirical values, this is not the case of the red edge: models predict a red edge below 6000 K, significantly lower than the empirical values of $\sim$ 11000 K (Van Grootel et al., 2012).

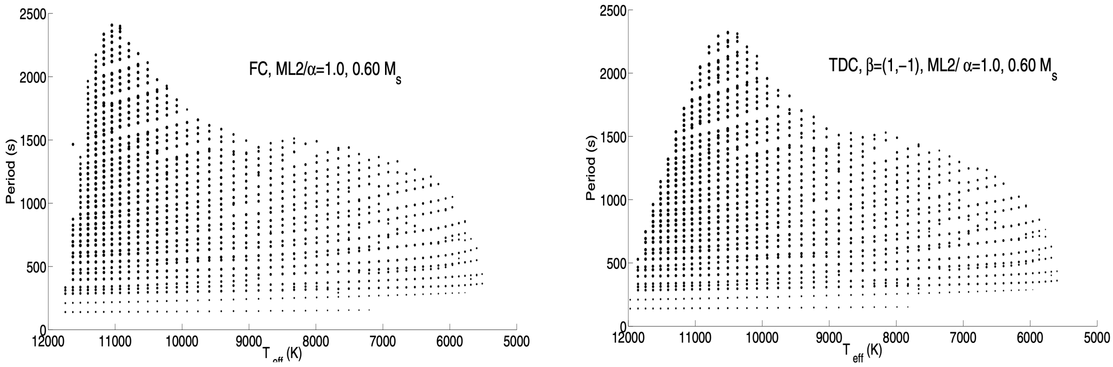

Figure 2.3: *Periods (in seconds) of the excited l=1 g-modes as functions of the effective temperature along the* $0.6\,M_\odot$ *evolutionary sequence computed with the detailed atmosphere modelling. The size of a dot is a measure of the excitation of that particular mode.* The figure on the left shows the result of frozen convection and the figure on the right from time-dependent convection. Figures and caption adapted from Van Grootel et al. (2012).

Chapter 3

Tidal Interactions in Binary Systems

Multiple star systems are prevalent throughout the universe. The majority of stars form with at least one companion, with the likelihood of multiplicity increasing statistically for stars of higher ZAMS mass as shown in Figure 3.1 (Offner et al., 2023). While many binaries have large orbital separations and therefore interact weakly, close companions can significantly influence each other's evolution through various dynamical processes.[1,2] This includes the tidal effect, studied in this chapter, and the emission of gravitational waves presented in Chapter 4.

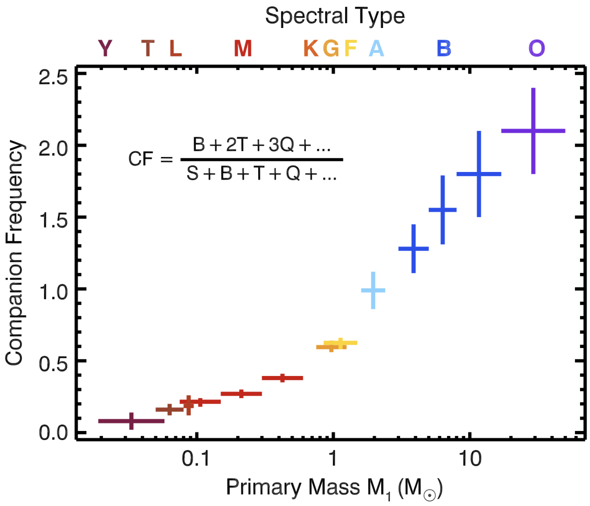

Figure 3.1: Frequency of stellar companion as a function of their mass. Credit: Offner et al. (2023)

To illustrate tidal interactions, consider the Earth-Moon system. By definition, the Earth has a rotational period of one day, while the Moon orbits the Earth in approximately 28 days. Notably, the Moon rotates about its own axis in the same time that it takes to orbit the Earth—which is why it always presents the same face towards our planet—this is referred to as *synchronisation*. The Moon's gravitational pull induces tidal forces on the Earth, most visibly demonstrated by the attraction of large water bodies that give rise to

---

[1] The understanding of the evolution of multiple star systems has grown into a dedicated field of research.

[2] As mentioned in section 1.5, such interactions are crucial to explain the existence of low-mass white dwarfs, exclusively found in binary systems.

the tides in the seas and oceans. However, because the Earth rotates more rapidly than the Moon orbits it, the tidal bulge is carried slightly ahead of the Earth-Moon axis. This misalignment results in a gravitational torque from the Moon that acts to re-align the tidal bulge with the Earth-Moon axis, thereby slowing the Earth's rotation and driving it toward synchronisation with the Moon's orbital period. Conversely, the Earth exerts an equal and opposite torque on the Moon's orbit, which accelerates the Moon and gradually increases its semi-major axis at a rate of 3.8 cm yr^{-1} (Williams & Boggs, 2016). This interaction in schematised on Figure 3.2:

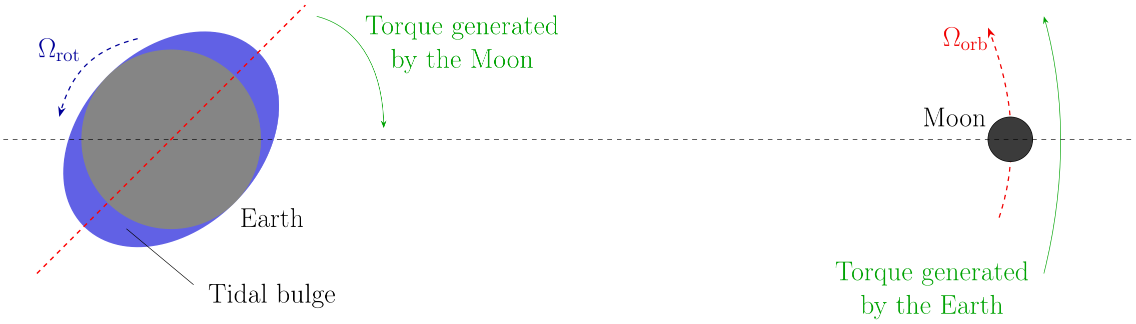

Figure 3.2: Diagram representing the effect of the tidal interaction in the Earth-Moon system.

As the Earth-Moon distance increases and the Earth's rotation gradually slows, the tidal forces weaken. This *dissipative* example demonstrates the impact of tidal interactions on a system's dynamics. In binary star systems, the tidal potential generated by the companion produces similar effects, and in addition, it influences the dynamics of stellar oscillations.

In this chapter, we first present a brief mechanical description of binary systems and how their orbital elements evolve under the action of a perturbative force. We then derive the expression of the centrifugal and tidal potentials which will be responsible for perturbations of the orbital elements. We will then present the behaviour of stellar oscillations under these conditions and their effect on the orbits.

3.1 Mechanical description of the orbit

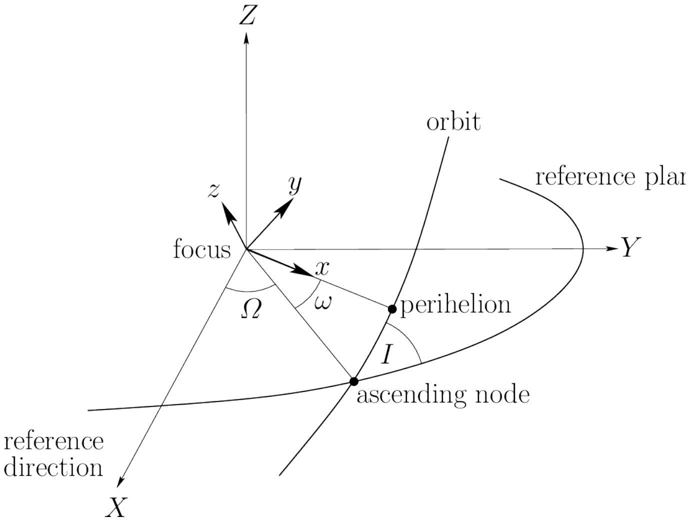

Figure 3.3: The classical orbital elements. Credit: Fitzpatrick (2021)

[3]In classical mechanics, the trajectory of a mass around the system's centre of mass is a conic. For closed orbits (the only ones considered here), these conics are ellipses and can be described using six parameters. First, we introduce a reference direction X and a reference plane XYZ. The orbital plane xyz intersects the reference plane, defining the *line of nodes.* The angle between the reference plane and the orbital plane defines the *inclination* I. The angle between the ascending node (the node corresponding to the crossing in the $+Z$ direction) and the reference direction defines the *longitude of the ascending node* Ω. The angle between the periastron, the point of closest approach of the mass to the centre of mass of the system, and the ascending node is called the *argument of the periastron* and is denoted ω. These angles are depicted in Figure 3.3. The remaining orbital elements are the *semi-major axis* a, the *eccentricity* e, and the *mean anomaly* $\mathcal{M}_0$, , which represents the fraction of an orbit's period that has elapsed since the body passed through periastron, expressed as an angle ranging from 0 to 2π.

If the orbit of the mass is not perturbed, the mean anomaly is the only parameter than will evolve over time. However, under the action of a perturbing force $\vec{F} = F_r\vec{e}_r + F_\theta\vec{e}_\theta + F_z\vec{e}_z$, the other orbital elements may evolve over time. In classical mechanics, the evolution of the orbital elements of an elliptic orbit is described by the *Gauss planetary equations*:

$$\frac{\dot{a}}{a} = \frac{2h}{\mu(1-e^2)}\left[e\sin\theta F_r + (1+e\cos\theta)F_\theta\right] \tag{3.1}$$

$$\dot{\mathcal{M}}_0 = \frac{h}{\mu}\frac{(1-e^2)^{1/2}}{e}\left(\left[\cos\theta - \frac{2e}{(1-e^2)}\frac{r}{a}\right]F_r - \left[1+\frac{1}{(1-e^2)}\frac{r}{a}\right]\sin\theta F_\theta\right) \tag{3.2}$$

$$\dot{e} = \frac{h}{\mu}\left[\sin\theta F_r + (\cos\theta + \cos E)F_\theta\right] \tag{3.3}$$

---

[3] In this section, we use the same usual formalism as Fitzpatrick (2021) to provide a mechanical description of the perturbation of orbits.

$$\dot{\omega} = -\frac{h}{\mu}\frac{1}{e}\left[\cos\theta F_r - \left(\frac{2+e\cos\theta}{1+e\cos\theta}\right)\sin\theta F_\theta\right] - \frac{\cos I\sin(\omega+\theta) r F_z}{h\sin I} \tag{3.4}$$

$$\dot{I} = \frac{\cos(\omega+\theta) r F_z}{h} \tag{3.5}$$

$$\dot{\Omega} = \frac{\sin(\omega+\theta) r F_z}{h\sin I} \tag{3.6}$$

where, $\mu = G(M_1 + M_2)$ and $h = \sqrt{\mu a(1-e^2)}$.

In this work, we will mainly consider circular orbits. In that specific case, the orbital elements and equations presented above are not directly applicable[4]. New orbital elements are typically introduced to treat circular motions. Notably, an equivalent of the mean anomaly will be employed later to express the tidal potential. The semi-major axis, however, remains well defined and is the principal quantity of interest. Its evolution is given by the same equation as Eq. (3.1), with $e = 0$:

$$\frac{\dot{a}}{a} = \frac{2h}{\mu}F_\theta \tag{3.7}$$

We have thus shown that in the presence of a perturbing force, the semi-major axis of a circular orbit evolves according to Eq. (3.7). In a binary system with two stars, M_1 and M_2, where M_1 is the primary, *tidal forces cause orbital perturbations*: the gravitational influence of M_2 distorts the shape of M_1, modifying the potential it generates and affecting the orbit of M_2. Likewise, M_1 deforms M_2, altering its gravitational potential and thereby influencing the orbit of M_1.

3.2 Tidally excited stellar oscillations

In binary systems, the companion's presence plays a key role on stellar oscillations. Indeed, additional contributions must be included in the equation of motion. First, one must account for the Keplerian and centrifugal potentials. Since a star both orbits the binary system's centre of mass and rotates about its own axis, two distinct motions must be considered when analysing the motion of an element of mass within the star. In addition to the effects of rotation, the gravitational potential of the companion must also be included. In the following, we develop the equations for M_1, accounting for the various effects induced by the presence of M_2. Naturally, these developments should similarly be applied on M_2 accounting for the presence of M_1. The equation of motion in the comoving frame is therefore written as:

$$\frac{\partial^2\delta\vec{r}}{\partial t^2} = -\nabla\psi' - \frac{\nabla P'}{\rho} + \frac{\rho'}{\rho^2}\nabla P - 2i\sigma_c\vec{\Omega}\times\delta\vec{r} + \nabla\psi_{\mathrm{orb},1} + \nabla\psi_{\mathrm{rot},1} + \nabla\psi_{\mathrm{grav},2:1}\,, \tag{3.8}$$

where $\psi_{\mathrm{orb},1}$ is the centrifugal potential due to the Keplerian (orbital) motion of M_1 about the system's centre of mass, $\psi_{\mathrm{rot},1}$ is the centrifugal potential resulting from the rotation of M_1 about its own axis, and $\psi_{\mathrm{grav},2:1}$ is the gravitational potential exerted by M_2 on M_1. By definition, the tidal potential $\psi_{\mathrm{tides},2:1}$ generated by M_2 on M_1 is given by

$$\psi_{\mathrm{tides},2:1} = \psi_{\mathrm{orb},1} + \psi_{\mathrm{grav},2:1}\,. \tag{3.9}$$

---

[4] Indeed, with $e = 0$ there is no periastron, and hence ω and $\dot{\mathcal{M}}_0$ are not defined.

Since the tidal potential is periodic (the period being the orbital period), we can decompose it into a Fourier series. This periodic forcing leads to mode frequencies that are integer multiples of the orbital frequency—a significant difference compared to the free oscillations discussed in earlier sections, whose frequencies depend exclusively on the star's intrinsic properties. In the corotating frame of M_1, these forcing frequencies are given by

$$\sigma_{k,m} = k\Omega_{\text{orb}} + m\Omega_{\text{rot}}, \tag{3.10}$$

where k is the index of the Fourier expansion (see Eq. (3.36) below), and where m is the number of meridional lines of the spherical harmonics.[5,6]

Mathematically, the problem to solve is therefore different. In the free non-adiabatic case, the set of equations and unknowns can be represented as

$$Ax = \sigma_{\text{free}} x\,, \tag{3.11}$$

where the matrix A contains the equations of the problem, x denotes the eigenfunctions, and σ_{free} the eigenvalues, which are directly related to the free oscillation frequencies and may be complex in the non-adiabatic case. Solving this eigenvalue problem yields both the frequencies and the oscillation amplitudes.

In binary systems, however, the eigenvalues are real and known—they correspond to the forcing frequencies $\sigma_{k,m}$ in the corotating frame of reference. In this work, the contribution of the centrifugal potential to the equation of motion ($\nabla\psi_{\text{rot}}$) will be negligible. Hence, the only additional term to account for is the tidal component $\nabla\psi_{\text{tides}}$ of the equation of motion, denoted here as b. Since this term depends on the orbital motion and not on the star's internal physics, it acts as an independent forcing term. Consequently, the matrix A from the non-adiabatic case remains unchanged relative to the free oscillations, and the problem is reformulated as

$$(A - \sigma_{k,m} I)\, x = b\,, \tag{3.12}$$

where I is the identity matrix. The solution to this inhomogeneous equation will provide the amplitudes corresponding to each integer multiple of the forcing frequency. The fact that A remains the same in both cases has an important consequence, as it leads to resonances between the star's free oscillations and the forcing due to the orbital motion. As it will be discussed in Section 3.2.7, if the forcing frequency perfectly matches a free oscillation frequency, the amplitudes of the oscillations may increase sharply until dynamical effects rapidly change the physical configuration of the system.

In the following sections, we derive expressions for these potentials in terms of orbital and stellar parameters. We will make the developments for an eccentric orbit and then present the simplifications brought by the circular case, which is the one that will be implemented further. *Note that throughout this work, we assume that each star's rotation axis is perpendicular to the orbital plane.*

---

[5] The number of meridional lines yields the degree of symmetry of rotation of the mode about the star's rotational axis, which is why the frequency measured in the corotating frame of reference is dependent on m.

[6] Thus, the frequencies of the tidally excited oscillations depend solely on these known forcing frequencies, independently of the stars' internal structures.

3.2.1 Keplerian and centrifugal potential

Let us consider an element of mass of M_1, situated at a distance $\vec{r}$ from the centre of mass of the star. We choose a set of axis centred on M_1 such that the x axis always points towards the centre of mass of the system as represented by the unitary vectors $(\vec{e}_x, \vec{e}_y)$ on Figure 3.4. The $\vec{e}_z$ vector, not represented, points out of the xy plane. We write the components of the vector $\vec{r} = (x_1, y_1, z_1)$. This vector forms an angle θ with the $\vec{e}_z$ axis and its projection $\vec{s}$ in the xy plane forms an angle ϕ_0 with the binary axis or, equivalently, with the $\vec{e}_x$ vector.

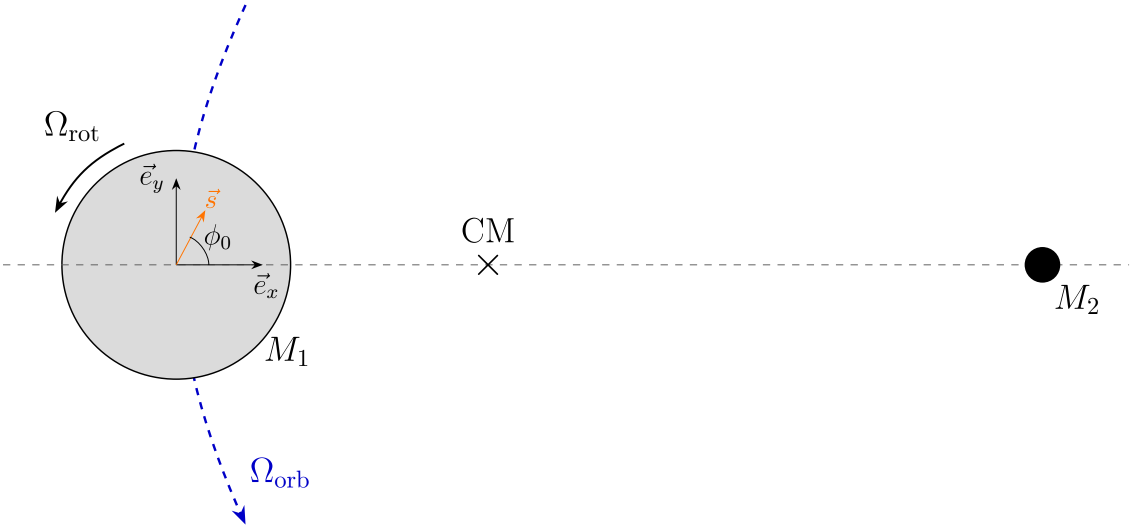

Figure 3.4: Diagram representing the orbital motion of M_1 around the centre of mass of the system M_1 - M_2 system and the rotation of M_1 about its own axis. The binary axis is represented by the horizontal dashed line, with the centre of mass (CM) represented by the cross.

In an inertial frame of reference, the total acceleration $\vec{a}$ experienced by an element of mass of M_1 is given by:

$$\vec{a} = \vec{a}_{\rm rot} + \vec{a}_{\rm orb}, \tag{3.13}$$

with $\vec{a}_{\rm rot}$ the acceleration due to the rotation of M_1 about its own axis, and $\vec{a}_{\rm orb}$ the acceleration of the centre of mass of M_1 due to its orbital motion about the centre of mass of the system. We therefore have:

$$\vec{a}_{\rm rot} = -\Omega_{\rm rot}^2 \sqrt{x_1^2 + y_1^2} \cdot \frac{\vec{s}}{|\vec{s}|} \tag{3.14}$$

$$\vec{a}_{\rm orb} = \frac{GM_2}{r_2^2} \cdot \vec{e}_x \tag{3.15}$$

where r_2 is the distance from the centre of mass of M_1 to the centre of mass of M_2. These accelerations can be written as the gradient of a potential. Using $x_1 = r \sin\theta \cos\phi_0 = r\lambda$, we can write the corresponding potentials as:

$$\psi_{\rm rot} = -\Omega_{\rm rot}^2 \frac{(x_1^2 + y_1^2)}{2} \tag{3.16}$$

$$\psi_{\rm orb} = \frac{GM_2}{r_2^2} x_1 = \frac{GM_2}{r_2} \left(\frac{r}{r_2} \right) \lambda \,. \tag{3.17}$$

Adding any purely time-dependent function $f(t)$ to these potentials has no effect, as the gradient operates on spatial coordinates.

3.2.2 Tidal potential in a binary system

The tidal potential arises from the gravitational forces exerted by one body on another. Since gravity varies with distance, different parts of M_1 experience slightly different gravitational forces from M_2, leading to tidal effects. The tidal potential quantifies these variations. We will derive the expression of the tidal potential in terms of *Legendre polynomials*, which are directly related to the spherical harmonics, by decomposing the perturbing gravitational potential. As before, we will develop the expressions for the effect of M_2 on M_1, but the same reasoning applies to the tidal effect of M_1 on M_2. In the following developments, we also consider M_2 to point-like. Finally, we keep working in a referential centred on M_1 and using the same notations as shown on Figure 3.4.

The gravitational potential $\psi_{\text{grav},2:1}$ exerted in $\vec{r}$ by M_2 is given by:

$$\psi_{\text{grav},2:1}\left(\vec{r},t\right) = -\frac{GM_2}{|\vec{r_2}-\vec{r}|}\,. \tag{3.18}$$

The denominator of Eq. (3.18) can be developed in Legendre polynomials, which are defined through the generating function

$$\left(1-2\gamma t+t^2\right)^{-\frac{1}{2}} = \sum_{n=0}^{\infty} t^n P_n(\gamma)\,. \tag{3.19}$$

Indeed, the denominator can be expressed as

$$\frac{1}{|\vec{r_2}-\vec{r}|} = \left((\vec{r_2}-\vec{r})\cdot(\vec{r_2}-\vec{r})\right)^{-\frac{1}{2}} = \left(r^2-2\vec{r}\cdot\vec{r_2}+\vec{r_2}^2\right)^{-\frac{1}{2}} = \frac{1}{r_2}\left(1-2\frac{\vec{r}\cdot\vec{r_2}}{r_2^2}+\frac{r^2}{r_2^2}\right)^{-\frac{1}{2}}\,. \tag{3.20}$$

From the geometry of the problem, we have $\vec{r}\cdot\vec{r_2} = rr_2\sin\theta\cos\phi_0 = rr_2\lambda$. Therefore, Eq. (3.20) becomes

$$\frac{1}{|\vec{r_2}-\vec{r}|} = \frac{1}{r_2}\left(1-2\frac{r}{r_2}\lambda+\frac{r^2}{r_2^2}\right)^{-\frac{1}{2}}\,. \tag{3.21}$$

The second factor of the right-hand side of this equation is of the form of Eq. (3.19), with $\gamma=\lambda$ and $t=r/r_2$. Therefore, we have

$$\frac{1}{|\vec{r_2}-\vec{r}|} = \frac{1}{r_2}\sum_{l=0}^{\infty}\left(\frac{r}{r_2}\right)^l P_l(\lambda). \tag{3.22}$$

A detailed derivation leading to this result is given in Appendix B, where it is obtained through a Taylor expansion about the centre of mass of the affected body. The gravitational potential of M_2 on M_1 can therefore be written as

$$\psi_{\text{grav},2:1}(\vec{r},t) = -\frac{GM_2}{r}\sum_{l=0}^{\infty}\left(\frac{r}{r_2}\right)^{l+1} P_l(\lambda), \tag{3.23}$$

where we factor out the term r^{-1}. The two first terms of this expression are:

$$l = 0 : -\frac{GM_2}{r_2} \tag{3.24}$$

$$l = 1 : -\frac{GM_2}{r_2}\left(\frac{r}{r_2}\right)\lambda. \tag{3.25}$$

The term $l = 0$ of the potential is independent of the spatial coordinates and can therefore be safely removed from the potential for the same reasons as previously. The term in $l = 1$ is exactly the opposite of the Keplerian potential given in Eq. (3.17). We can therefore write:

$$\psi_{\text{tides},2:1} = \psi_{\text{orb},1} + \psi_{\text{grav},2:1}(\vec{r}, t) \tag{3.26}$$

$$= -\frac{GM_2}{r}\sum_{l=2}^{\infty}\left(\frac{r}{r_2}\right)^{l+1} P_l(\lambda). \tag{3.27}$$

In general, the Legendre polynomials $P_l(\lambda)$ are related to the spherical harmonics $Y_l^m(\theta, \phi_0)$ through the relation

$$P_l(\lambda) = \sum_{m=-l}^{l} c_{lm} Y_l^m(\theta, \phi_0). \tag{3.28}$$

In Eq. (3.27), we have thus obtained a first decomposition of the potential in terms of Legendre polynomials, or equivalently, spherical harmonics. This decomposition is made with respect to the binary axis (as indicated by the Legendre polynomials' dependence on λ). However, to study the oscillations we prefer to work relative to the star's rotation axis. Since any spherical harmonic defined with respect to one axis can be expanded into $2l + 1$ spherical harmonics with respect to a different axis, we can decompose the potential relative to the rotational axis. The projection along the rotation axis is given by $\mu = \cos\theta$.

As will be shown later in this work, the orbital evolution occurs on timescales significantly longer than the orbital period. Therefore, the motion of M_2 around M_1 can be considered periodic over the timescale of a few revolutions. This is often referred to as *secular* evolution in the literature, meaning a slow evolution of the orbital parameters. Under this approximation, we can expand the expression for $\psi_{\text{tides},2:1}$ in a Fourier series. To this end, the potential can be expressed in terms of the *associated Legendre polynomial* through the relation

$$Y_l^m(\theta, \phi_0) = c'_{lm} P_l^m(\mu) e^{im\phi_0}, \tag{3.29}$$

where the c'_{lm} are normalization coefficients. Therefore, the potential can be expressed relative to the star's rotational axis as

$$\psi_{\text{tides},2:1}(\vec{r}, \nu) = -\frac{GM_2}{r}\sum_{l\geq 2}^{\infty}\sum_{m=-l}^{l}\left(\frac{r}{r_2}\right)^{l+1} d_{lm} P_l^m(\mu) e^{im\phi_0}, \tag{3.30}$$

where the d_{lm} coefficients are given by

$$d_{lm} = \frac{(l-m)!}{(l+m)!} P_l^m(0). \tag{3.31}$$

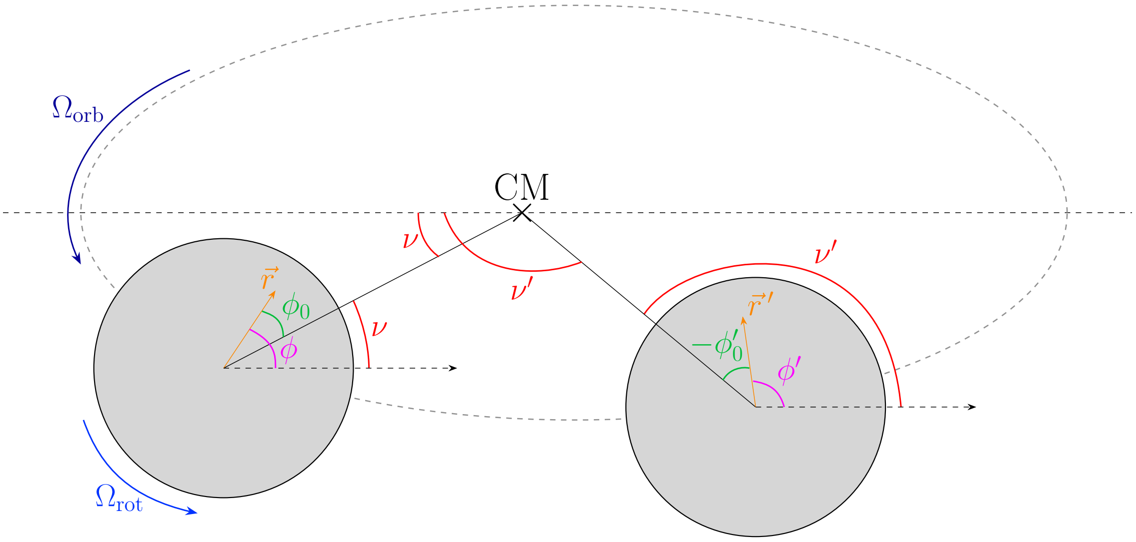

Figure 3.5: The different angles defined in this analysis at two positions on the orbit, which represented by the dashed ellipse. The dashed horizontal arrows are parallel to the semi-major axis, from which the angle ϕ is defined.

Note that the $P_l^m(0)$ are equal to zero when the sum of l and m is odd, which removes several terms contributing to the tidal potential (Willems et al., 2010). Indeed, the *odd terms* represent deformations that are asymmetric about the equatorial-orbital plane, which is impossible in regard to the symmetry of the problem. The remaining terms are called *even terms*.

Instead of using ϕ_0, we can use the true anomaly ν by defining the angle ϕ as the angle between the vector $\vec{r}$ and a parallel to the semi-major axis. These angles are represented on Figure 3.5. We thus have that $\phi_0 = \phi - \nu$ and therefore we can write

$$\psi_{\rm tides,2:1}(\vec{r},\nu) = -\frac{GM_2}{r}\sum_{l\geq 2}^{\infty}\sum_{m=-l}^{l}\left(\frac{r}{r_2}\right)^{l+1} d_{lm}P_l^m(\mu)e^{im(\phi-\nu)}. \tag{3.32}$$

The decomposition in Fourier series of a time-dependent function f can be defined as

$$f(\mathcal{M}) = \sum_{k=-\infty}^{\infty} f_k e^{-ik\mathcal{M}}, \qquad f_k = \frac{1}{2\pi}\int_0^{2\pi} f(\mathcal{M})e^{ik\mathcal{M}}d\mathcal{M}, \tag{3.33}$$

with the mean anomaly $\mathcal{M} = \Omega_{\rm orb}(t-t_0)$ as a linear function of time. In order to obtain an expression of this form for the potential $\psi_{\rm grav,2:1}$, the time-dependent terms of Eq. (3.32) can be written as

$$e^{-im\nu}\left(\frac{r}{r_2}\right)^{l+1} = \left(\frac{r}{a}\right)^{l+1} e^{-im\nu}\left(\frac{a}{r_2}\right)^{l+1} = \left(\frac{r}{a}\right)^{l+1}\sum_{k=-\infty}^{\infty} X_k^{-(l+1),-m}e^{-ik\mathcal{M}}, \tag{3.34}$$

where the $X_k^{-(l+1),-m}$ are the Hansen coefficients defined such that

$$X_k^{n,-m}(e) = \frac{(1-e^2)^{n+3/2}}{2\pi}\int_0^{2\pi}\frac{\cos(m\nu + k\mathcal{M})}{(1+e\cos\nu)^{n+2}}d\mathcal{M}\,. \tag{3.35}$$

Injecting this result in Eq. (3.32), we obtain:

$$\psi_{\text{tides},2:1}(\vec{r},\nu) = -\frac{GM_2}{r}\sum_{l=2}^{\infty}\sum_{m=-l}^{l}\sum_{k=-\infty}^{\infty}\left(\frac{r}{r_2}\right)^{l+1} X_k^{-(l+1),-m} d_{lm} P_l^m(\mu) e^{i(m\phi - k\mathcal{M})}. \quad (3.36)$$

Thanks to our decomposition of the potential in spherical harmonics, the problem is *separable* (see Section 2.5). Including the rotation of M_1 about its axis requires further development, notably by expanding the Hough functions in series. This extension is implemented in the *MAD_ tides* code used further in this work (see Fellay et al. 2024).

3.2.3 Effect of tidal interaction on the orbit

With the expression of $\psi_{\text{tides},2:1}$, it is now possible to solve the forced oscillation problem as formulated in Eq. (3.12), which is usually done using dedicated non-adiabatic codes. This yields the values of the perturbed potential ψ_1' of M_1 across the star and, in particular, at its surface. From this potential, we can then obtain the perturbation of the orbit of M_2.

In practice, it is useful to obtain a dimensionless expression the star's response $\text{Im}(F_{l,m,k})$ to the tidal forcing:

$$\text{Im}(F_{l,m,k}) = -\frac{1}{2}\frac{R_1}{GM_1}\,\text{Im}(\psi'_{l,m,k}(R_1)), \quad (3.37)$$

where R_1 is the radius of M_1. The evolution of the semi-major axis is given by

$$\frac{da}{dt} = 4\Omega_{\text{orb}}\frac{M_2}{M_1}a\sum_{l=2}^{\infty}\sum_{m=-l}^{l}\sum_{k=-\infty}^{\infty}\left(\frac{R_1}{a}\right)^{l+3}\text{Im}(F_{l,m,k})G^{(2)}_{l,m,k}(e) \quad (3.38)$$

where the $G^{(2)}_{l,m,k}(e)$ are defined as (Willems et al., 2010):

$$\begin{aligned} G^{(2)}_{l,m,k}(e) = & \quad \frac{2}{\pi(1-e^2)^{l+1}}c_{l,m,k}(e)P_l^{|m|}(0) \\ & \times\left[(l+1)e\int_0^{\pi}(1+e\cos\nu)^l\sin(m\nu+k\mathcal{M})\sin\nu d\nu\right. \\ & \left. -m\int_0^{\pi}(1+e\cos\nu)^{l+1}\cos(m\nu+k\mathcal{M})d\nu\right], \end{aligned} \quad (3.39)$$

with

$$c_{l,m,k}(e) = X_k^{-(l+1),-m} d_{lm}\left(\frac{R_1}{a}\right)^{l-2}. \quad (3.40)$$

One remarkable feature of Eq. (3.38) is that it depends on the imaginary part of the tidal response, *whose sign is directly related to the stability of the oscillation modes.* Hence, **stable modes have the opposite effect of unstable modes on the evolution of the semi-major axis of the system**. This also shows a direct link between the orbital evolution due to tides and the non-adiabaticity of the tides. In the adiabatic conservative case, there would be no orbital evolution. Similarly, the eccentricity of the orbit evolves following

$$\frac{de}{dt} = 4\Omega_{\text{orb}}\frac{M_2}{M_1}\sum_{l=2}^{\infty}\sum_{m=-l}^{l}\sum_{k=-\infty}^{\infty}\left(\frac{R_1}{a}\right)^{l+3}\text{Im}(F_{l,m,k})G^{(3)}_{l,m,k}(e), \quad (3.41)$$

which shares similar conclusion as the equation of evolution of the semi-major axis. The expression of $G^{(3)}_{l,m,k}(e)$ is given by (Willems et al., 2010):

$$\begin{aligned} G^{(3)}_{l,m,k}(e) = & \frac{2}{\pi(1-e^2)^{l+1}} c_{l,m,k}(e) P_l^{|m|}(0) \\ & \times \left[(l+1)e \int_0^\pi (1+e\cos\nu)^l \sin(m\nu + k\mathcal{M}) \sin\nu d\nu \right. \\ & \left. -m \int_0^\pi (1+e\cos\nu)^{l-1} \left[(1+e\cos(e\cos\nu)^2) - (1-e^2) \right] \cos(m\nu + k\mathcal{M}) d\nu \right]. \end{aligned} \tag{3.42}$$

We can define $\tau_{a,\text{tides}} = a/|da/dt|$ and $\tau_{e,\text{tides}} = e/|de/dt|$ as the typical timescale of evolution of the semi-major axis and the eccentricity due to the effect of tides. Taking the ratio between these two quantities thus yields:

$$\Rightarrow \quad \frac{\tau_{e,\text{tides}}}{\tau_{a,\text{tides}}} = e \cdot \frac{\sum_{l=2}^{\infty} \sum_{m=-l}^{l} \sum_{k=-\infty}^{\infty} \left(\frac{R_1}{a}\right)^{l+3} \text{Im}(F_{l,m,k})\, G^{(2)}_{l,m,k}(e)}{\sum_{l=2}^{\infty} \sum_{m=-l}^{l} \sum_{k=-\infty}^{\infty} \left(\frac{R_1}{a}\right)^{l+3} \text{Im}(F_{l,m,k})\, G^{(3)}_{l,m,k}(e)} \tag{3.43}$$

The dominant term are the $l = 2$, $m = \pm 2$ for which we thus have

$$\frac{\tau_{e,\text{tides}}}{\tau_{a,\text{tides}}} = e \cdot \frac{G^{(2)}_{2,\pm 2,k}(e)}{G^{(3)}_{2,\pm 2,k}(e)} \tag{3.44}$$

Inspecting Eqs. (3.39) and (3.42) reveals that the dependence of the $G_{l,m,k}$ on R_1 and a cancels out. Thus, this ratio is independent of the radius of the white dwarfs and of their separation.

3.2.4 Effect of tidal interactions on the rotation

As with the Earth and the Moon, any change in the semi-major axis of a stellar system is always accompanied by a counterbalancing effect on the rotation of the stars. This is a key difference that distinguishes the effect of tides from the effect of gravitational waves on the dynamics of binary systems. This aspect is crucial to properly model the evolution of the system. The evolution of a star's angular velocity Ω_{rot} is by (Willems et al., 2010):

$$\frac{dI\Omega_{\text{rot}}}{dt} = 4\Omega_{\text{orb}} \left(\frac{Ga}{M_1 + M_2} \right)^{1/2} M_2^2 \sum_{l=2}^{\infty} \sum_{m=-l}^{l} \sum_{k=-\infty}^{\infty} \left(\frac{R_1}{a} \right)^{l+3} \text{Im}(F_{l,m,k}) G^{(4)}_{l,m,k}(e), \tag{3.45}$$

where the values of the $G_{l,m,k}$ coefficients are given in Willems et al. (2010). Notice that the dependency on the stability of the oscillation mode is also present.

3.2.5 Simplifications for circular orbits

As explained in Section 3.1, certain orbital elements are undefined in the circular case. This applies to the mean anomaly and the true anomaly, both of which are defined relative to the pericentre of elliptical orbits—a point that is indeterminate for circular orbits. Nevertheless, one may adopt a fixed reference direction instead. Since the angular velocity remains constant throughout an orbital revolution, the circular equivalents of the mean and true anomaly coincide. This quantity is referred to as the *true longitude*. In the following, we shall retain the notation $\mathcal{M}$ to denote the true longitude, as they encapsulate the same concept. For circular orbits, the Hansen coefficients (Eq. (3.35)) therefore become

$$X_k^{n,-m}(e=0) = \frac{1}{2\pi}\int_0^{2\pi} \cos((m+k)\mathcal{M})d\mathcal{M} = \delta_{k,-m}. \tag{3.46}$$

These coefficients are hence always equal to zero except if $k=-m$. Therefore, the only non-zero terms of the tidal potential in the circular case are the $k=-m$ terms and Eq. (3.36) becomes:

$$\begin{aligned}\psi_{\mathrm{tides},2:1}(\vec{r},\mathcal{M}) &= -\frac{GM_2}{r}\sum_{l=2}^{\infty}\sum_{m=-l}^{l}\sum_{k=-\infty}^{\infty}\left(\frac{r}{r_2}\right)^{l+1}\delta_{k,-m}d_{lm}P_l^m(\mu)e^{i(m\phi-k\mathcal{M})} &(3.47)\\ &= -\frac{GM_2}{r}\sum_{l=2}^{\infty}\sum_{m=-l}^{l}\left(\frac{r}{r_2}\right)^{l+1}d_{lm}P_l^m(\mu)e^{im(\phi+\mathcal{M})}. &(3.48)\end{aligned}$$

The expression of the evolution of the semi-major axis therefore reduces to

$$\frac{da}{dt} = 4\Omega_{\mathrm{orb}}\frac{M_2}{M_1}a\sum_{l=2}^{\infty}\sum_{m=-l}^{l}\left(\frac{R_1}{a}\right)^{l+3}\mathrm{Im}(F_{l,m,-m})G^{(2)}_{l,m,-m}(e), \tag{3.49}$$

and similarly

$$\frac{dI\Omega_{\mathrm{rot}}}{dt} = 4\Omega_{\mathrm{orb}}\left(\frac{Ga}{M_1+M_2}\right)^{1/2}M_2^2\sum_{l=2}^{\infty}\sum_{m=-l}^{l}\left(\frac{R_1}{a}\right)^{l+3}\mathrm{Im}(F_{l,m,-m})G^{(4)}_{l,m,-m}(e) \tag{3.50}$$

for the evolution of the rotation of the star. For both equations, we notice a strong dependence on R_1 and a through the factor $(R_1/a)^{l+3}$. Finally, for the dominant mode ($l=2, m=\pm 2$) discussed further, we have: $G^{(2)}_{2,\pm2,\mp2}(0) = \mp 3/2$ and $G^{(4)}_{2,\pm2,\mp2}(0) = \pm 3/4$ (Willems et al., 2010).

3.2.6 Oscillation modes

The main effect of the tidal potential is to generate two tidal bulges on the stars, one facing the companion and the other on the opposite side. In the circular case, this corresponds to the $l=2$, $k=-m=\pm 2$ term, as illustrated in Figure 2.1. Mathematically, this term dominates the tidal potential. For circular orbits, this can be obtained from the analysis of Eq. (3.48): the factor $(r/r_2)^{l+1}$ decreases rapidly with increasing l. Since only even terms remain, the only $l=2$ terms left are those for which $m=0$ and $m=\pm 2$. For the $m=0$ term, the exponential $\exp(im(\phi-\nu)) = \exp(im\phi_0)$ equals 1 and the potential is thus independent of ϕ. This term is axisymmetric and corresponds to a flattening of the star along its rotational axis. Hence, it cannot be responsible for the tidal torque and the subsequent effects on the orbital and rotational frequencies. In contrast, for the $m=\pm 2$ term, the exponential $\exp(im(\phi-\nu)) = \exp(im\phi_0)$ reaches its maximum in the directions facing and opposite the companion, corresponding to the tidal deformation along the binary axis. This term can therefore generate the tidal torque in the system.

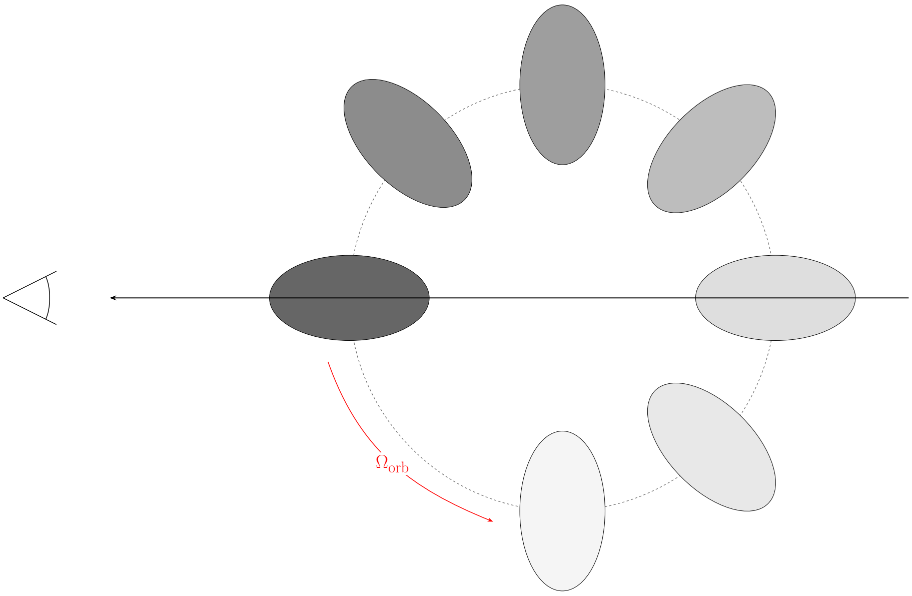

Figure 3.6: Orbital motion of a star with a tidal bulge. From the point of view of an external observer, represented by the eye on the left, the same deformation is observed twice over an orbital revolution.

From the point of view of an external observer, the same deformation of the star is observed twice over a full orbital revolution as schematised on Figure 3.6. Hence, the frequency of the tidal oscillation observed by an inertial observer is

$$\sigma_0 = |k\Omega_{\mathrm{Orb}}| = |\pm 2\Omega_{\mathrm{Orb}}|. \tag{3.51}$$

Since $k = -m$ in the circular case, the frequency observed from the point of view of an observer corotating with the star, which is the frequency of tidal excitation, is

$$\sigma_{k,m} = k\Omega_{\mathrm{Orb}} - m\Omega_{\mathrm{rot}} = m(\Omega_{\mathrm{rot}} - \Omega_{\mathrm{Orb}}) \tag{3.52}$$

From the expression of the tidal potential, we have therefore shown that the $(l = 2, k = -m = \pm 2)$ terms are responsible for the oscillation of the tidal bulges. Based on the orbital and rotation frequencies, three important cases must be examined. For *stable* modes, we have *in the dissipative case*:

- If $\Omega_{\mathrm{rot}} = \Omega_{\mathrm{Orb}}$, the star is said to be *synchronised* with its companion. In this case, the star always shows the same face to its companion and the tidal bulges remain static relative to the stellar surface ($\sigma_{k,m} = 0$).
- If $\Omega_{\mathrm{rot}} > \Omega_{\mathrm{Orb}}$, the star's motion is said to be *super-synchronous.* This situation is analogous to that of the Earth-Moon system. Here, the tidal bulge is lying slightly ahead of the line of perfect synchronisation in the direction of the rotation. Consequently, the tides act against the star's rotation, slowing it down. These tides are *retrograde* in the corotating frame. In response, **the semi-major axis of the orbit increases**.
- If $\Omega_{\mathrm{rot}} < \Omega_{\mathrm{Orb}}$, the star's motion is said to be *sub-synchronous.* In this case, the tidal bulge lags behind the line of perfect synchronisation. Consequently, the tides act to increase the rotation of the star. These tides are *prograde* in the corotating frame. In response, **the semi-major axis of the orbit decreases**.

In the two latter cases, the tides are called *dynamical tides* in opposition to the *static tides* of the synchronised case. These different scenarios are schematised on Figure 3.7. For *unstable* modes, the same logic applies, except that the sign of the imaginary part of the star's potential response is reversed, and consequently so is the sign of da/dt. As a final note, in highly eccentric systems the contributions from terms with $|k| \gg |m|$ become increasingly important.

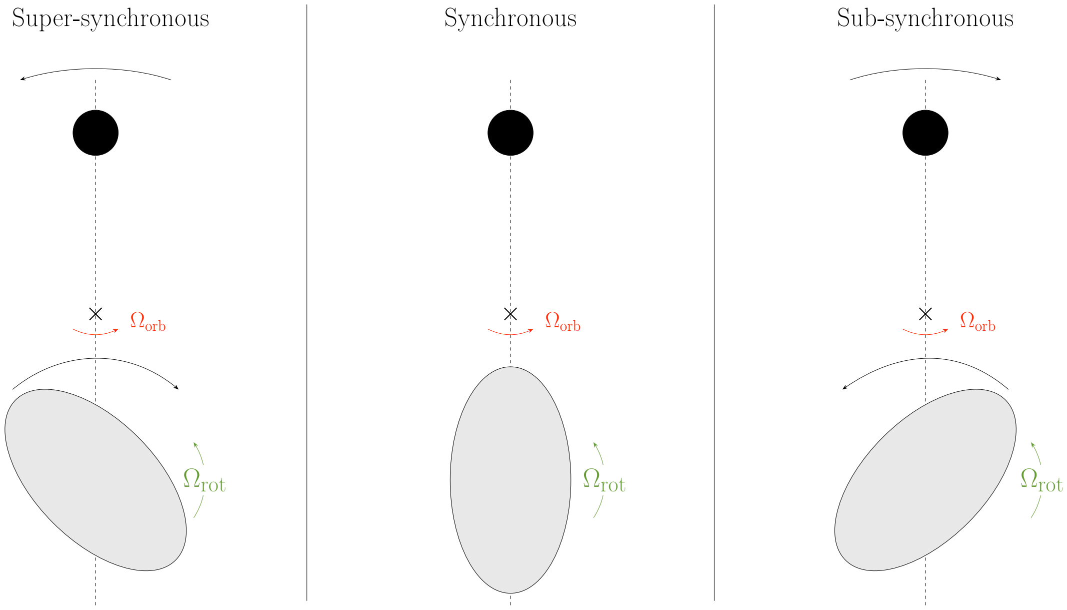

Figure 3.7: Different scenarios depending on Ω_{orb} and Ω_{rot} for *stable* oscillation mode. The grey ellipse represents the studied star M_1, the black circle represents the companion M_2 and the cross represents the centre of mass. The unlabelled black arrows above the companion and above M_1 represent the torque applied by M_1 on the orbital motion of M_2 and the torque applied by M_2 on the rotation of M_1 respectively. No torque is generated by the tidal force in the synchronous case. One can see that the tide is retrograde in the super-synchronous case and prograde in the sub-synchronous case.

3.2.7 Orbital evolution and resonance phenomenon

In this work, we study the joint effect of gravitational wave and tides on binary systems. As it will be presented in Chapter 4, the impact of gravitational waves on the mechanics of the system is limited to the reduction of the semi-major axis. Gravitational waves cannot lead to an increase in the semi-major axis, nor can they act on the rotation of the stars. *The effect of gravitational waves and tides on the semi-major axis combine linearly* because we use a perturbative approach. Therefore, gravitational waves can either work against tides or together with tides to modify the semi-major axis but *only tides will act on the rotation of the stars.* The resulting variation in stellar separation will depend on the dominating phenomenon.

As the distance between the two stars evolves, the system may encounter peculiar configurations. As mentioned at the beginning of Section 3.2, a *resonance* between a free oscillation frequency of the star and the tidal forcing can occur when the orbital frequency matches a free oscillation frequency. A perfect resonance drastically amplifies the amplitude of the tides and their impact on the system's dynamics. To illustrate, consider a system whose orbital dynamics is initially dominated by gravitational waves. As the orbital frequency gradually increases, several scenarios may occur upon encountering a resonance. If the amplified tides act in the same direction as the gravitational waves, they will contribute to a more rapid reduction of the separation between the two stars, with the passage through the resonance peak eventually providing a "*kick*" towards a shorter separation. If the tides act against the gravitational waves, two cases may arise. If the effect of gravitational waves remains stronger than that of the tides even at the peak of resonance, the tides will slow the decrease in separation but not prevent it. However, if the tidal effect eventually increases to counterbalance the effect of gravitational waves as the system approaches resonance, the evolution of the semi-major axis may become temporarily frozen. We call such a situation a *resonance locking.* **This situation, however, does not remain stable indefinitely.** As the tides act to preserve the distance between the two components, they also affect their rotation, which will eventually unfreeze the situation by modifying the synchronisation and free oscillation frequencies.

3.2.8 Roche Lobe Constraint

Several assumptions and simplifications in the above developments may lead to inaccuracies when the semi-major axis is small. Consequently, it is necessary to impose a lower limit on a, below which the results are considered unreliable. In practice, this threshold is not rigorously defined. A fully three-dimensional model of the oscillations could, in principle, provide a more precise criterion, but such models remain to be implemented. Nevertheless, a commonly used limit in stellar astrophysics serves as an indicator: the point at which one of the binary components fills its *Roche lobe.* The Roche lobe defines the region around a star within which material remains gravitationally bound. It corresponds to the outermost equipotential surface that encloses only one star. Hence, this surface passes through the *L1 Lagrange point* of the binary system. The equipotential lines and the Roche lobes are represented on Figure 3.8.

Geometrically, the shape of the Roche lobe depends on the mass ratio $q = M_1/M_2$, and in general, its exact form can only be determined numerically. Nevertheless, approximate analytical solutions exist. One approach is to define an *effective radius* R_1 for the star, which corresponds to the radius of a spherical of the same volume as the one that would fill the Roche lobe. A commonly used approximation, derived by Eggleton (1983), is given by

$$\frac{a}{R_1} \approx \frac{0.6\, q^{2/3} + \ln\left(1 + q^{1/3}\right)}{0.49\, q^{2/3}}, \tag{3.53}$$

so that for a binary system of equal-mass stars ($q = 1$) one obtains $a/R_1 \approx 2.7$. When a star fills its Roche lobe, material may transfer to its companion via the L1 Lagrange point. Even prior to this stage, the star can undergo significant deformation as shown on Figure 3.9, indicating that the underlying assumptions of our treatment may no longer be valid. For this reason, we choose to disregard the results of models if

$$\frac{a}{R_{L1}} < 5\,. \tag{3.54}$$

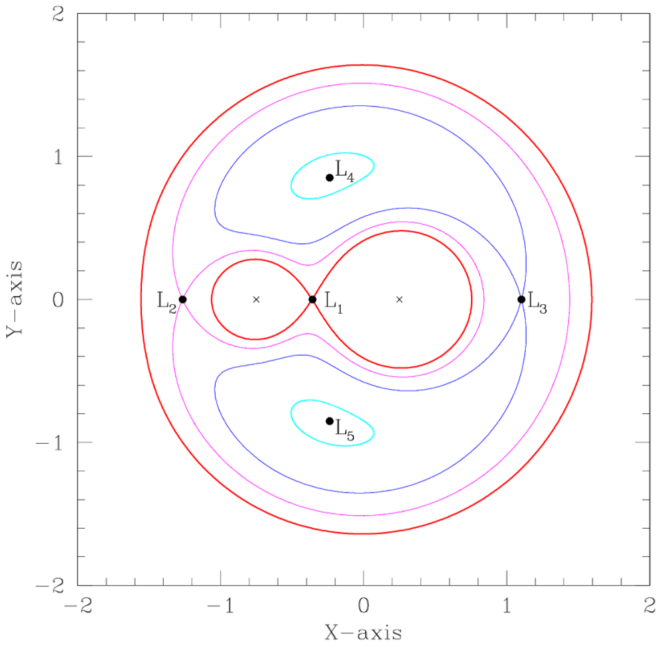

Figure 3.8: Equipotential lines in a binary systems. The inner red curve passing through the Lagrange point $L1$ represent the Roche lobes. Any equipotential within these lobes only circles one of the stars. Image credit: Boffin (2014)

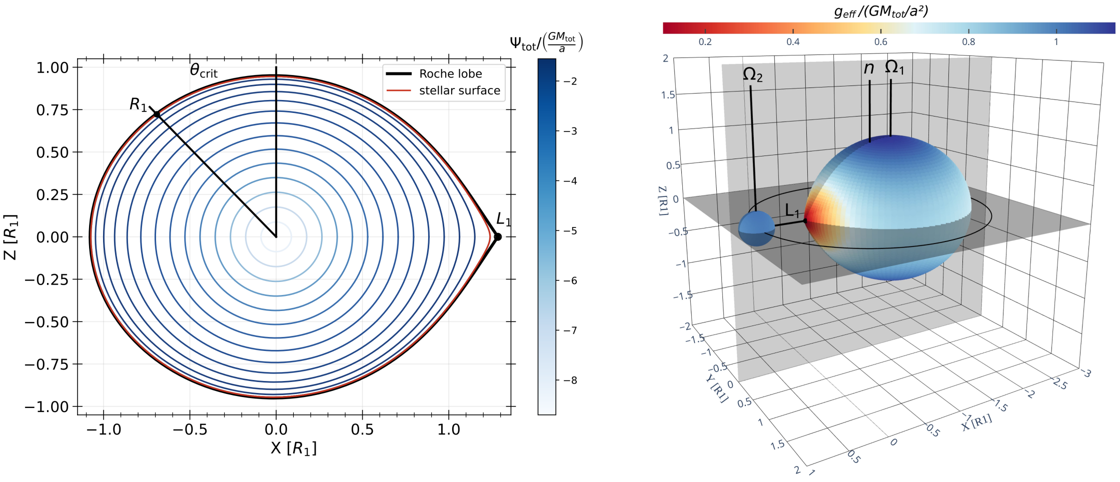

Figure 3.9: Two figures representing the effect of strong tidal deformation in binary systems. Credit: Fellay et al. (2024)

Chapter 4

Gravitational Waves

The history of gravitational waves is closely tied to the development of special and general relativity. An early analogy between gravitational and electromagnetic fields was proposed by Heaviside (1894-1912), suggesting that changes in a gravitational field might propagate similarly to electromagnetic waves.[1] Following Lorentz's work on transformations, Poincaré proposed in 1905 that gravitational interactions propagate at the speed of light. Consequently, a sudden displacement of a massive body would only be observed after a delay corresponding to the time taken for the gravitational signal—travelling at the speed of light—to reach the observer. Poincaré named the corresponding wave *'ondes gravifiques'* in French, or *gravitational waves* in English (Pointcaré, 1905).

Einstein obtained a first mathematical description of gravitational waves as a consequence of his general theory of relativity published in 1916. According to his equations, massive objects can create waves in space-time propagating at the speed of light. In 1918, he published a paper dedicated to the theoretical exploration of gravitational waves where he developed key concepts still used to this day (Einstein, 1916, 1918).

4.1 Sources of gravitational waves

In theory, any moving mass is a source of gravitational waves. However, space-time is extremely stiff and large amounts of energy is required to produce even the smallest detectable signal. Detectable signals are hence only generated in extreme astrophysical events and phenomena. Among these figure the merger of massive compact bodies, black holes and neutron stars. These so-called *compact binary coalescent*—or *CBC*—are to this day the only gravitational wave events ever recorded. These events are very short and well modelled in most situations. The first such event was GW150914, a merger of two black holes of ~ 29 and $36\ \mathrm{M}_\odot$ about 410 Mpc away from Earth. Approximately $3\ \mathrm{M}_\odot$ of mass was converted into gravitational energy, with a power 50 times exceeding the power output of all the stars in the visible universe. Yet, at the peak of emission the gravitational strain—the fractional distortion of space-time caused by a gravitational wave—was only of 10^{-21} (Abbott et al., 2016). This shows the incredible engineering achievement behind this first detection as the detectors must show unprecedented sensitivity. More information on this event is summarised on Figure 4.1. Since this first observation, the sensitivity of the detectors is constantly improving. By 2020, over 90 such events have been recorded

---

[1] The idea that gravitation propagates at a finite speed had been explored by earlier authors, such as Laplace in the 18th century, though none formulated a complete mathematical framework.

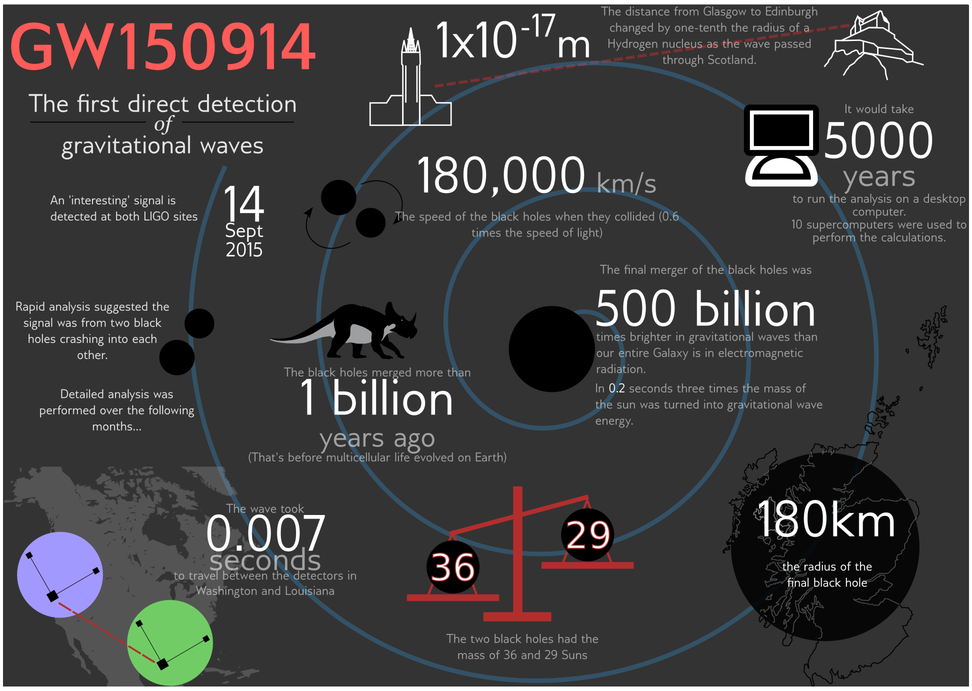

Figure 4.1: Infographic of the first detection of gravitational waves, GW150914. Credit: Williams (2016)

with various confidence levels (Abbott et al., 2023). Most of them are binary black hole mergers and a few are neutron-star-black-hole mergers. Only two neutron star mergers have ever been recorded. Due to the lower masses and larger radius of neutron stars compared to black holes, these events emit less powerful gravitational waves and are therefore more difficult to observe. The first, and most significant, was GW170817. This event was the first ever to be observed through both its gravitational waves emission and its electromagnetic counterpart, being the first example of *multi-messenger astronomy* (Abbott et al., 2017).

There are a few factors impacting the detectability of gravitational waves. Naturally, the distance to the source and the amount of energy radiated are key factors. Additionally, the source must also emit gravitational waves with frequencies detectable by the detectors. Current ground-based detectors can detect signal with frequencies from ~ 30 to 2000 Hz. The sensitivity of the detector varies depending on the frequency band considered. Future ground-based detectors are expected to both improve the overall sensitivity of the detectors but also to extend the range of measurable frequencies to ~ 3 to 8000 Hz.

To this day, only CBC events have ever been observed through their emission of gravitational waves. Indeed, it is at the merger that the gravitational waves are the strongest. However, binary systems still radiate a significant amount of energy as gravitational waves on longer timescales—exceeding the observation timescale—before the merger. These waves, classified as *continuous waves*, are yet to be observed with future detectors. The gravitational wave emission studied in this work is of this nature. Indeed, white dwarf binaries are expected to emit gravitational waves very similarly to black hole and neutron stars binaries but at significantly lower frequencies (below 1 Hz). Detecting such low-frequency signal from ground-base detectors is currently impossible due to the seismic noise. However, the future space-based *Laser Interferometer Space Antenna* (LISA) detector will be dedicated to the exploration of this part of the gravitational wave spectrum. The study of white dwarf binaries is among the key objectives of this mission:

> *"LISA will survey WD binaries with orbital periods of less than ∼15 minutes across the entire Milky Way volume, allowing us to reconstruct the stellar mass distribution of our Galaxy using evolved stars invisible to EM telescopes." (ESA, 2023, p.32)*

For a source to emit gravitational waves, a non-axis-symmetric distribution of mass must be accelerated.[2] This condition is naturally fulfilled by binary systems. An asymmetric neutron star can also meet this criterion. With their fast rotation and the proximity of some of them, it has been shown that a faint gravitational wave emission could be measured from such objects. These would also be categorised as continuous wave emission since their period varies slowly over the timescale of the observations. In the search of such sources, pulsars are of prime interest since their period is already known from electromagnetic measurements.

Finally, supernovae may also emit detectable gravitational waves. However, these signals are difficult to model, their detection relies on identifying short, unmodelled, coherent bursts—typically lasting only a few seconds—in gravitational-wave detectors (Ott, 2009). At very low frequencies, it has been proposed that a stochastic background of gravitational waves exists, primarily arising from the mergers of binary supermassive black holes (Detweiler, 1979; Sesana et al., 2008). Furthermore, it has been hypothesised that a *fossil gravitational wave background*, analogous to the cosmic microwave background observed in electromagnetic radiation, may persist as a relic of the Big Bang.

4.2 Evolution of a binary system under the effect of gravitational waves

Before we limiting ourselves to the circular orbits treated in this work, for which we only need the expression of the derivative of the semi-major axis, let us present the derivative of a and e in the eccentric case. These expressions were first derived by Peters (1964) in his PhD thesis and are now often called *Peters' formulas*:[3]

$$\left\langle \frac{da}{dt} \right\rangle = -\frac{64}{5}\frac{G^3 M_1 M_2 (M_1+M_2)}{c^5 a^3 (1-e^2)^{7/2}}\left(1+\frac{73}{24}e^2+\frac{37}{96}e^4\right). \tag{4.1}$$

This expression depends notably on a^{-3}, showing that the effect of gravitational waves on the semi-major axis becomes particularly significant as short separations. The eccentricity evolves following

$$\left\langle \frac{de}{dt} \right\rangle = -\frac{304}{15}e\frac{G^3 M_1 M_2 (M_1+M_2)}{c^5 a^4 \left(1-e^2\right)^{5/2}}\left(1+\frac{121}{304}e^2\right), \tag{4.2}$$

showing again a strong dependence on the semi-major axis. These two equations are **always negative**, which implies that gravitational waves always act towards the shrinkage of the orbit and its circularisation. To illustrate, we show on Figure 4.2 the timescale of evolution of the semi-major axis $\tau_{a,\mathrm{gw}} = a/|da/dt|$ and of the eccentricity $\tau_{e,\mathrm{gw}} = e/|de/dt|$.

---

[2] The distribution of mass is said to have a *quadrupolar moment.*

[3] These expressions yield the *secular change* of the parameters, which are thus shown between brackets.

To compare determine which evolves the fastest, we can take the ratio between $\tau_{a,\mathrm{gw}}$ and $\tau_{e,\mathrm{gw}}$, which yields:

$$\frac{\tau_{e,\mathrm{gw}}}{\tau_{a,\mathrm{gw}}} = \frac{192}{304} \frac{\left(1 + \frac{73}{24}e^2 + \frac{37}{96}e^4\right)}{(1-e^2)\left(1 + \frac{121}{304}e^2\right)}. \tag{4.3}$$

This result, which surprisingly only depends on the eccentricity, is shown on Figure 4.3. At low eccentricity ($e \to 0$), $\tau_{e,\mathrm{gw}}/\tau_{a,\mathrm{gw}} \approx 0.632$ and the eccentricity evolves slower than the semi-major axis.[4] At larger eccentricities, the semi-major axis evolves on shorter timescales than the eccentricity. This implies that gravitational waves might not be able to circularise systems with large initial eccentricities by the time they merge. In order to obtain a definitive solution, we need to solve the system made of Eq. (4.1) and Eq. (4.2) as done in Chapter 7.

Since $e = 0$ in the circular case, da/dt is independent of the position on the orbit and we have:

$$\frac{da}{dt} = -\frac{64}{5}\frac{G^3M^2\mu}{c^5a^3} \tag{4.4}$$

with $\mu = M_1M_2/(M_1+M_2)$ the reduced mass and $M = M_1 + M_2$. We can directly integrate this equation to obtain the evolution of the separation as a function of time:

$$a^4(t) = a_0^4 - \frac{256}{5}\frac{G^3M^2\mu}{c^5}t = a_0^4\left(1 - \frac{t}{\tau_\mathrm{c}}\right), \tag{4.5}$$

where a_0 is the separation in $t = 0$ and τ_c is the *coalescence time* of the system, which corresponds to the time needed for the semi-major axis to reach 0 solely due to the effect of gravitational waves. It is thus given by

$$\tau_\mathrm{c} = \frac{2}{256}\frac{c^5a_0^4}{G^3M^2\mu}. \tag{4.6}$$

---

[4] Note that $e/|de/dt|$ is undefined when $e = 0$ since $de/dt = 0$.

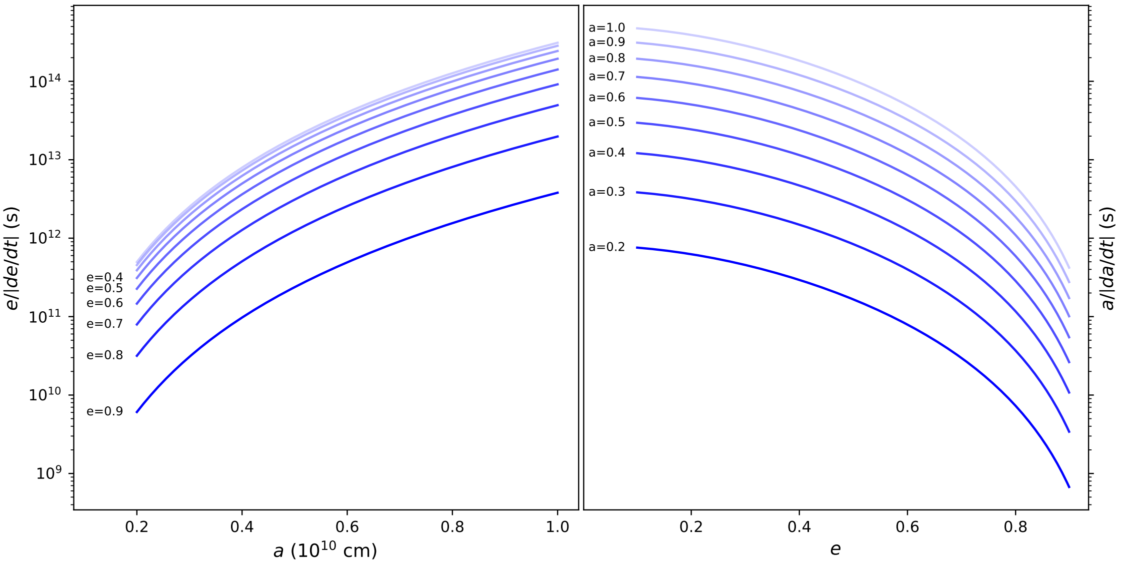

Figure 4.2: Characteristic evolution timescales for a compact binary under gravitational wave emission. **Left:** Eccentricity damping timescale as a function of a. Each curve is separated by 0.1 in eccentricity. **Right:** Orbital shrinkage timescale as a function of e. All distances are given in 10^{10} cm.

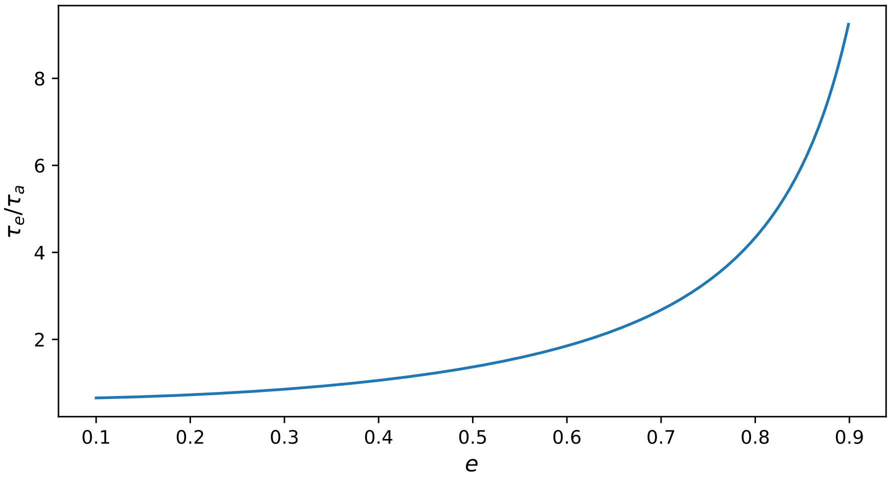

Figure 4.3: Dependence of the ratio of the eccentricity evolution timescale to the semi-major axis evolution timescale on eccentricity.

Part II

Methods and Results

Chapter 5

White Dwarf Models and Free Oscillations

Before modelling the competition between tidal forces and gravitational wave emission, we must first compute the white dwarf structures and their free oscillation modes. In this chapter, we present the codes used to obtain the white dwarf models as well as the non-adiabatic code used to determine their free oscillation modes.

5.1 White dwarf structure models

The white dwarf models used in this work were computed with a version of the code first presented in Fontaine et al. (2001). For a given choice of mass and core composition, this code yields a sequence of ~ 150 models covering the white dwarf's full evolution, from its formation to its cooler stages. Thus, we obtain models at different effective temperatures (or equivalently, at different ages). The code assumes spherical symmetry and provides all physical quantities as a function of depth within the star. In this work, we selected 0.2, 0.25, 0.4 and 0.6 $M_\odot$ models with a *pure carbon core* to represent carbon-oxygen white dwarfs.[1] This choice is rather arbitrary as the precise carbon-oxygen ratio in C-O white dwarfs is largely uncertain (Giammichele et al., 2022). We also include a 0.2 $M_\odot$ helium core model to explore the effect of core composition on the oscillation modes and on binary evolution. All models have a *hydrogen atmosphere* and thus are DA white dwarfs.

When studying the evolution of white dwarf binary systems, it is important to account for the cooling timescale of the stars. Indeed, oscillation modes are directly related to the temperature of the white dwarfs and its effect on their structure. If a white dwarf cools on timescales much longer than the typical timescale of semi-major axis evolution, the position of the resonance peaks will not change significantly as the system evolves towards them because the free oscillation frequencies are a function of the nearly frozen internal structure. However, if the cooling timescale is significantly shorter than the timescale of evolution of the semi-major axis, the stars may cross the instability strip so fast that very few to no resonance has had the time to arise by the time the stars leave the strip and the orbital parameters would have in principle no time to change significantly during this crossing.

---

[1] Although our pure carbon core models do not contain oxygen, they are still part of the carbon-oxygen core white dwarfs. We will thus continue to designate them as such for most of this work.

We define the cooling timescale of a white dwarf as the time required for it to cool by 1000 K at its current rate, a reference chosen to match the typical temperature width of the instability strip. For a model i, we compute the cooling timescale $t_{\mathrm{cool},i}$ by taking:

$$t_{\mathrm{cool},i} = \frac{t_{i+1} - t_i}{T_{\mathrm{eff},i} - T_{\mathrm{eff},i+1}} \cdot 1000\,\mathrm{K}, \tag{5.1}$$

where the fraction represents the rate of temperature change between model i and the following, cooler, model $i+1$.

White dwarf cooling is strongly impacted by convection and the thickness of the atmosphere. Hence, the cooling timescales depend on the convective treatment and the parameters of the atmosphere adopted in the models. In Bédard et al. (2020), the authors present a new version of the code used to produce the white dwarf structure models used in this work. On the website of the University of Warwick, one can access the summary files of these new cooling sequences for models with a thin and a thick atmosphere (Bédard, 2020). For these models, the core composition was chosen to be 50% carbon, 50% oxygen in mass fraction, which is an important difference with the models used in this work. In Figure 5.1, we compare the cooling timescale of the 0.2 $M_\odot$ carbon core model used in this work (the reference model) with the corresponding new carbon-oxygen models with thin and thick atmosphere in a range of effective temperatures covering the instability strip. While there are noticeable differences in the cooling timescale of these different models, they remain within the same order of magnitude.

At higher effective temperatures, the new models have significantly shorter cooling timescales than the reference model. On Figure 5.2, the upper panel represents the evolution of the temperature of the same 0.2 $M_\odot$ models with each model shifted such that they all reach 10000 K at the same time, at which point all these models should be within the instability strip. This reference temperature is represented by the grey dashed line. There is thus an uncertainty on the cooling timescales of our models which has to be borne in mind when considering the evolution of a system beginning at higher effective temperatures.

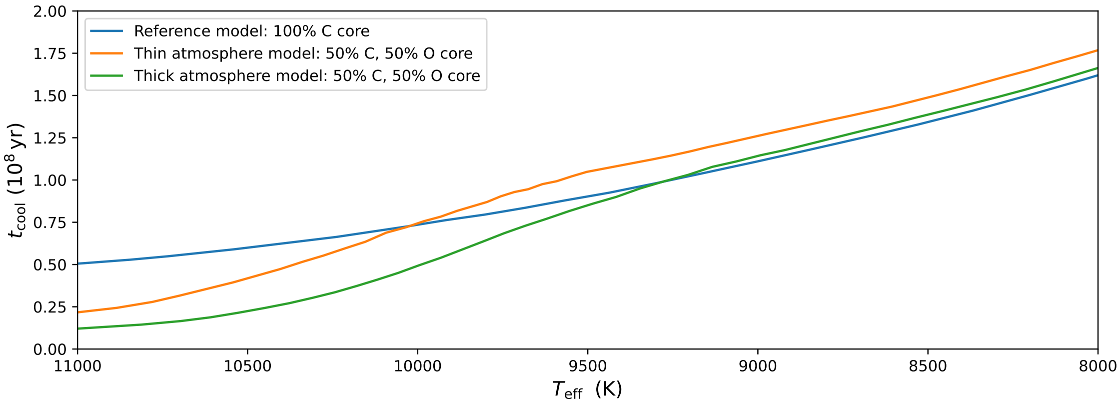

Figure 5.1: Comparison of the cooling timescale of the different 0.2 $M_\odot$ carbon-oxygen core models as a function of the effective temperature. The reference model corresponds to the models based on Fontaine et al. (2001) while the thin and thick atmosphere models are based on Bédard (2024).

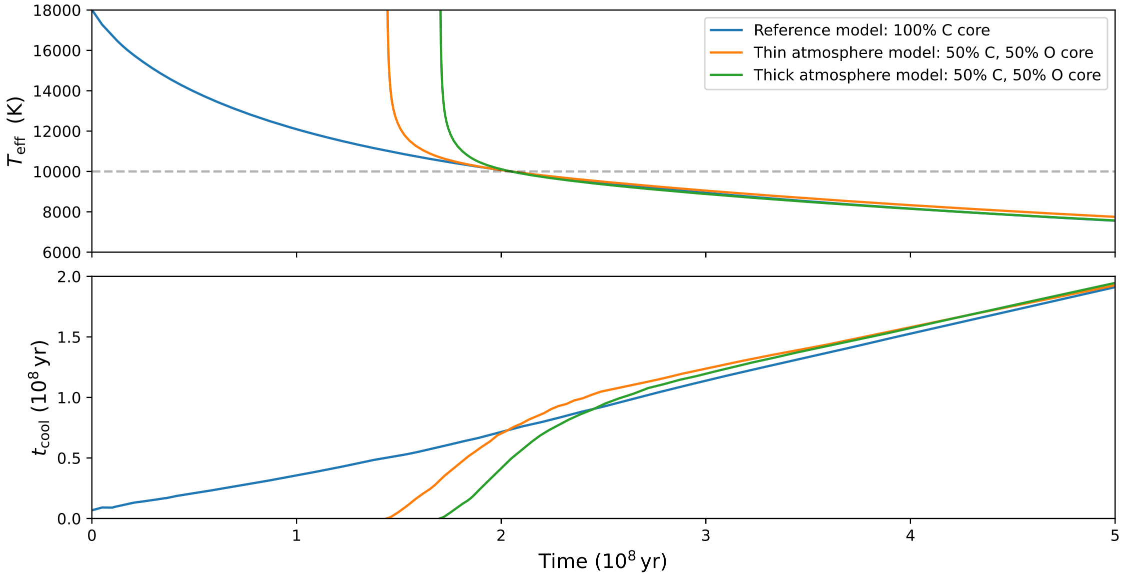

Figure 5.2: **Upper panel:** Evolution of the effective temperature of the three 0.2 $M_\odot$ models as a function of time. The curves have been shifted such that the model reach a temperature of 10000 K simultaneously. The grey dashed line corresponds to 10000 K. **Lower panel:** Comparison of the cooling timescale of the three 0.2 $M_\odot$ models as a function of time. The reference model corresponds to the models based on Fontaine et al. (2001) while the thin and thick atmosphere models are based on Bédard (2024).

5.2 Non-adiabatic stellar oscillation models

In order to properly model the impact of stellar oscillations on white dwarf binary evolution, it is essential to work with a non-adiabatic code as a simple adiabatic treatment is notably unable to yield information on mode stability. In this work, we will be specifically working with the non-adiabatic *MAD* code, detailed in Dupret (2001).

Van Grootel et al. (2012) used MAD and white dwarf structure models based on Fontaine et al. (2001) to determine the instability strip of ZZ Ceti white dwarfs as previously shown on Figure 2.3. For a given white dwarf, reproducing these figures allows to determine which of its model is the first to be within the instability strip as the effective temperature decreases. This can be done by directly computing all the g-modes at the different effective temperatures and localising the first to become unstable. Figure 5.3 shows our result for the 0.6 $M_\odot$ model. Similarly to Van Grootel et al. (2012), we obtain a well defined entry in the instability strip at around 12000 K, in agreement with empirical blue edge values. However, the red edge is still not well defined.

In Appendix D, additional figures are provided for non-rotating 0.2 and 0.4 $M_\odot$ C-O models, for a rotating 0.2 $M_\odot$ C-O model, and for a non-rotating 0.2 $M_\odot$ He model. These figures can be briefly commented. While adding rotation did not appear to have a significant impact on the entry of the 0.2 $M_\odot$ C-O model in the instability strip, we note that the spectrum of unstable modes is noticeably modified. The core composition also appears to play an important role in the oscillation spectra but does not significantly affect

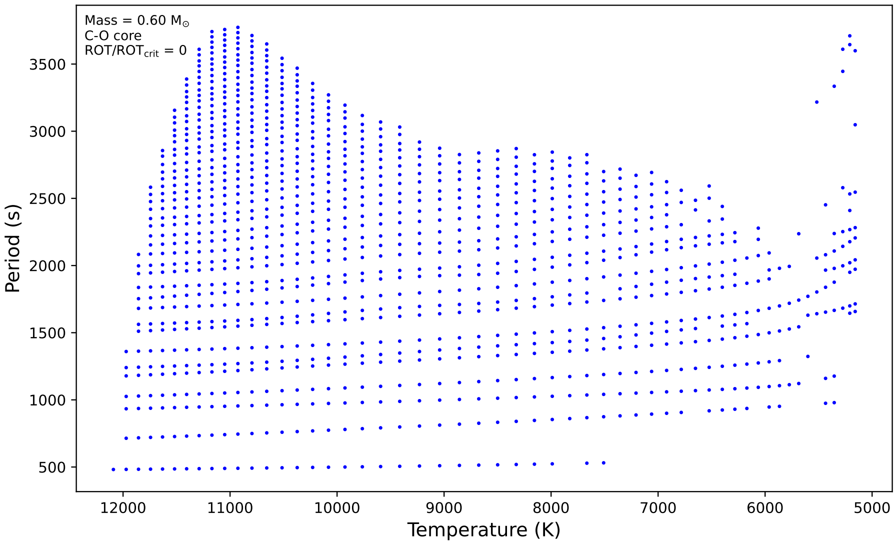

Figure 5.3: Period of unstable g-modes (blue) for a 0.6 $M_\odot$ C-O model as a function of its effective temperature.

the temperature of the ZZ Ceti blue edge of the our 0.2 $M_\odot$ model. Overall, mass is clearly the dominant factor influencing the temperature of blue edge crossing.

The stability of a mode is directly related to its work integral as it propagates through the white dwarf. To illustrate this, we select one stable and one unstable mode for the 0.6 $M_\odot$ model just below 12000 K and plot their work integrals from the centre to the surface in Figure 5.4. Note that the work integral represented here is a running integral, evaluated from the star's centre up to the layer corresponding to each value of q. Similarly to Figure 1.3, the abscissa is defined as

$$q \equiv 1 - \frac{M(r)}{M_{\text{tot}}}, \tag{5.2}$$

where M_{tot} is the total mass of the white dwarf. Thus, q directly represents the fraction of the white dwarf's mass lying above radius r, and the envelope of white dwarfs thus correspond to $q < 10^{-2}$ (see Section 1.5). Since the work integral of the two modes remains equal to zero in the entirety of the core, this implies that it is adiabatic. We can only see the non-adiabaticity at play in the outermost layers. When the work integral decreases in a region of the star, it means that the mode is damped there. On the other hand, when it increases, that region drives the mode. For a stable mode, the work integral remains negative all the way to the surface, indicating net damping. In contrast, for an unstable mode the work integral becomes positive near the surface, showing that excitation has outweighed damping as the mode travelled through the star.

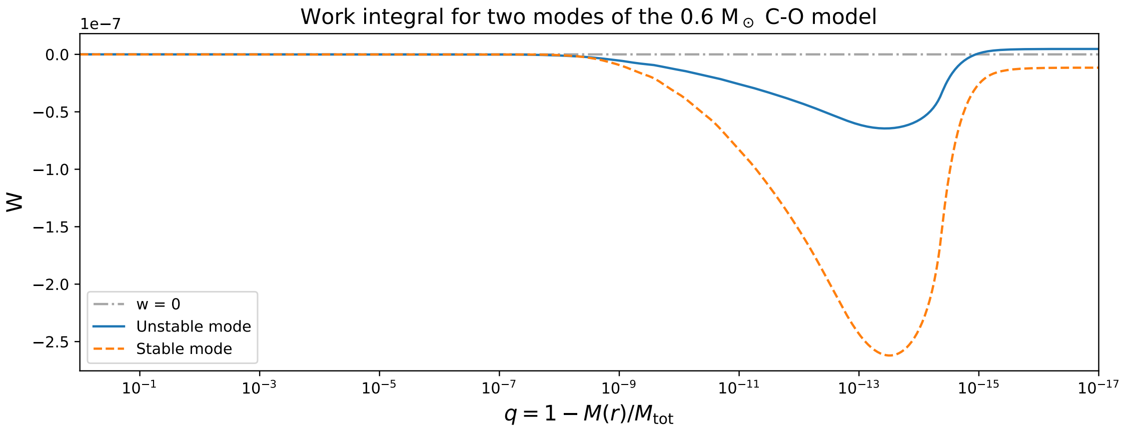

Figure 5.4: Work integral of a stable and an unstable mode of a 0.6 $M_\odot$ C-O white dwarf.

Chapter 6

Modelling Tidal and Gravitational Wave Effects on Semi-Major Axis

In this chapter, we describe the codes employed and the results of modelling the tidal and gravitational wave effects on the semi-major axis of white dwarf binary systems. We identify which parameters favours resonance locking by examining the effect of mass, rotation rate, effective temperature, and core composition. In addition, we explore the influence of orbital eccentricity. Finally, we provide a brief overview of the orbital evolution code tested in this work and discuss the limitations encountered when applying it to our systems.

6.1 Tidally excited oscillation and gravitational wave codes

6.1.1 Presentation of the Codes

To compute the rate of change of the semi-major axis, we adapted the code **MAD_tides**, originally presented in Fellay & Dupret (2025), for white dwarfs. This non-adiabatic code yields the imaginary part of the star's perturbed potential in response to the periodic tidal forcing of its companion by solving the problem outlined in Chapter 3. **The companion is treated as a point-like mass, so only the effect on the primary is computed.**[1]

MAD_tides was modified to sample a range of orbital and stellar rotation frequencies.[2] We also ran the code on white dwarf models of various masses and temperatures to explore the parameter space. The code requires the following inputs:

- A white dwarf model at a specified mass and temperature,
- A range of orbital frequencies and the number of sample points (typically 1000 to 2000),
- A set of stellar rotation frequencies,
- The eccentricity (set to 0 unless stated otherwise),
- The oscillation mode (l, m, k).

As justified in Section 3.2.6, the ($l = 2$, $k = -m = \pm 2$) modes dominate the tidal response. We therefore restrict our computations to these modes.

---

[1] As the tidal effects on the semi-major axis combine linearly, one could run MAD_tides for the secondary and combine the results to model a scenario in which both components experience tidal oscillations.

[2] We do not include evolutionary effects at this stage.

As noted in the code's original presentation, the tidal interaction problem can be solved without specifying the secondary mass or system eccentricity. Thus, MAD_tides is independent of these parameters, allowing their effects to be explored without rerunning the code and saving substantial computational time.

MAD_tides outputs *the dimensionless tidal response of the star* due to the presence of its companion. To obtain modelled values of da/dt, this output must be combined with the white dwarf model properties, and secondary mass and eccentricity values must be specified. Unless stated otherwise, **we present results for twin systems ($M_1 = M_2$)**. In the circular case, these values can be inserted into Eq. (3.49), which further simplifies when considering only the ($l = 2$, $k = -m = \pm 2$) modes. When exploring the effect of eccentricity, we integrate the full expression for da/dt, including the $G^{(2)}_{l,m,k}(e)$ factor (see Eqs. (3.38) and (3.39) and their integration in Section 6.2).

Finally, computing the gravitational wave effect on the semi-major axis is straightforward, requiring only the implementation of Eq. (4.1). All gravitational wave and tidal calculations based on MAD_tides outputs were performed with a new *Python* code, provided in Appendix C.

6.1.2 Results and effect of the main parameters

In the plots presented in this section we show $a/(da/dt)$, rather than da/dt directly, as a function of the orbital period for a fixed model (mass and temperature) and a fixed rotation of the star. In practice, this means that, for each plot, MAD_tides solves the problem $(A - \sigma_{k,m} I)x = b$, presented in Chapter 3, for a range of forcing frequencies $\sigma_{k,m}$ directly related to the orbital frequencies through the relation:

$$\sigma_{k,m} = k\Omega_{\text{orb}} + m\Omega_{\text{rot}}. \tag{6.1}$$

The advantage of using $a/(da/dt)$ is that it represents the time required for the semi-major axis to change by an amount equal to itself at the evolution rate computed at this value of the semi-major axis. Hence, the strongest the effect of the tides or gravitational waves, the lower the value of $a/(da/dt)$. This notably allows to compare the orbital evolution timescale to the white dwarfs' cooling timescale (see Section 5.1). The cooling timescale is represented by the green dash-dotted horizontal line in the plots.

We restrict our scans to a narrow range around the orbital synchronisation frequency. Extended scans show that the tidal effect on the semi-major axis diminishes rapidly both just below and just above synchronisation and further away from it, producing two "*bucket*" regions where tides have their maximal impact on the semi-major axis.

Let us illustrate by taking a first example, given in Figure 6.1. This plot shows the value of $a/(da/dt)$ from gravitational waves and tides as a function of the period close to system synchronisation. Note that the axes are on a log-log scale and the horizontal axis is inverted, so that as the binary evolves towards shorter orbital periods—and thus smaller separations—it moves from left to right in the plot. The system is made of a primary white dwarf of 0.6 $M_\odot$ with an effective temperature of 20059 K, and a secondary component of the same mass treated as a point mass. The rotation of the primary (0.40 in this example) is given as the rotation frequency of the star divided by its *critical rotation* frequency, defined

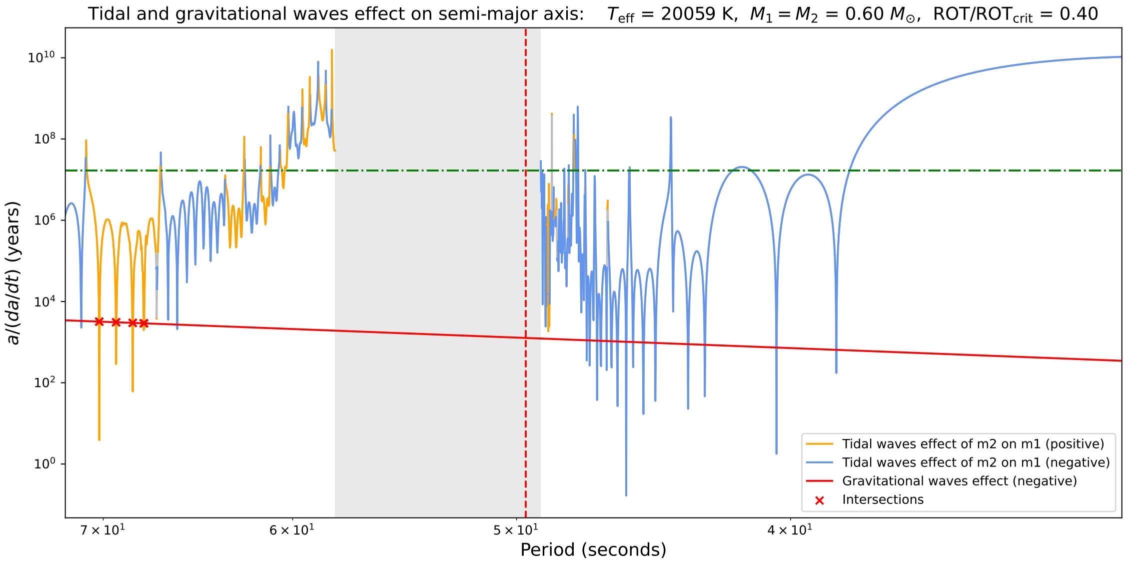

Figure 6.1: Example of a period scan of the $a/(da/dt)$ from gravitational waves and tides for a binary system of white dwarfs where the secondary is treated as a point mass.

as the rotation needed for the centrifugal force to equal the gravitational attraction at equator. Mathematically, the critical rotation is given by $\mathrm{ROT}_{\mathrm{crit}} = 1/t_{\mathrm{dyn}}$. $\mathrm{ROT}/\mathrm{ROT}_{\mathrm{crit}}$ can therefore be seen as the relative importance of the centrifugal and gravitational force on the oscillation modes. More massive white dwarfs are more compact and can thus reach higher rotation frequencies before the centrifugal force surpasses the gravitational force at equator. To isolate the importance of the mass of rotating white dwarfs on their oscillations, it is thus more relevant to keep the same $\mathrm{ROT}/\mathrm{ROT}_{\mathrm{crit}}$—or, equivalently, the same relative importance of centrifugal to gravitational force—rather than the same rotational frequency.

Since we keep the star's rotation frequency constant on the plots of orbital frequency scans, the star is super-synchronous at large separations (left side of the vertical line) and sub-synchronous for short orbital periods (right side of the vertical line). The vertical red dashed line on the plots separates these two regimes, representing the system's period at which synchronisation is achieved.[3] Very close to synchronisation, the amplitude of the modes decrease by several orders of magnitude and the effect of tides therefore becomes negligible, even at resonances. To understand this behaviour, note that in the circular case Eq. (6.1) reduces to

$$\sigma_{k,m} = m\left(\Omega_{\mathrm{rot}} - \Omega_{\mathrm{orb}}\right). \tag{6.2}$$

At synchronisation, $\sigma_{k,m} = 0$, so the corresponding tide is the static equilibrium tide. By our sign convention, positive m corresponds to retrograde modes while negative m corresponds to prograde modes. Hence, the super-synchronous dynamical tides on the left are retrograde, and the sub-synchronous dynamical tides on the right are prograde. As the orbital period approaches the rotation period ($\Omega_{\mathrm{orb}} \to \Omega_{\mathrm{rot}}$), $\sigma_{k,m} \to 0$. In that limit, the radial order of the resonant modes and the spin parameter both tend to infinity (since

---

[3] i.e. when the orbital period of the scan equals the white dwarf's rotation period.

$\sigma_{k,m}$ appears in the denominator of the spin parameter, Eq. (2.72)), causing the resonance amplitudes to drop.[4] For retrograde modes, the eigenvalue λ (see Section 2.6 on rotation and the traditional approximation) increases with the spin parameter and also tends to infinity. In contrast, for prograde modes λ decreases as the spin parameter grows. Thus, at any given small $\sigma_{k,m}$, retrograde modes have much higher radial order than prograde modes. Around synchronisation, this suppresses retrograde dynamical tide amplitudes (left) more strongly, rendering their impact on the orbit negligible.

Since gravitational waves always act to reduce the semi-major axis of the system, we plot its **negative** with a solid red line, which appears as a straight line in a log-log diagram. We use a log-log scale because both gravitational wave and tidal rates span several orders of magnitude. As tides can either increase or decrease the semi-major axis depending on the mode excitation, da/dt changes sign. Wherever $da/dt = 0$, $a/\left(da/dt\right)$ is undefined, and Python represents this as a vertical plunge to zero—potentially suggesting a spurious enhancement of the tidal effect at these sign changes. To avoid this artefact, we plot $a/|da/dt|$ in *orange* when $a/(da/dt) > 0$ and in *blue* when $a/(da/dt) < 0$.[5] Consequently, a counterbalance with gravitational waves only occurs when the positive (orange) curve crosses the always negative red curve. These *intersections* are of prime interest, as they correspond to the onset of *resonance locking* discussed in Section 3.2.7. Figure 6.1 shows one such intersection, represented by the red cross. When the negative (blue) tide curve crosses the gravitational wave curve, it corresponds to *kicks* for which the tidal effect exceeds that of gravitational waves. Note, however, that a crossing is not strictly necessary for a kick to occur. Since the boundary between what constitutes a kick and what does not is not rigorously defined, any resonance resulting in sufficient orbital decay may play this role.

Since this model is before the entry in the instability strip, *all the oscillation modes are stable.* Hence, following the discussion on the effect of oscillation modes on the semi-major axis presented in Section 3.2.6, $a/(da/dt)$ should be exclusively positive (orange) for super-synchronous rotation (at large orbital periods) and negative (blue) for sub-synchronous rotation (at short orbital periods). Yet, Figure 6.1 shows many sign changes, in particular in the super-synchronous case. We currently suspect that they are caused by numerical errors in the tidal interaction code. Indeed, the free oscillation code used by MAD_tides exclusively computes stable oscillation modes.

Another limitation of these computations is that the amplitude of the tidal response at a resonance peak is underestimated. Since $a/(da/dt)$ is computed on a fixed grid of orbital frequencies, the calculation cannot converge to the true peak value at a resonance. Consequently, we may miss some intersections of the positive (orange) tidal curve with the gravitational wave (red) curve. This arises because resonance widths in white dwarfs, directly related to damping rates, are extremely narrow compared to those in main-sequence stars (Fellay 2025, submitted). In fact, as seen from Eq. (2.83), the inertia of the mode (denominator) dominates over the excitation and damping terms (numerator), which are confined to the superficial, negligible-mass layers of the star (see also Figure 5.4). Although

---

[4] The fact that high order radial modes lead to weaker tides can be explained with a *modal decomposition approach*, as in Fuller (2017). Note that this approach differs from our *direct simulation* method, which is more precise than the modal decomposition but less straightforward to interpret.

[5] As the resulting plots is disjoint, we also plot $a/|da/dt|$ in grey in the background regardless of the sign in order to obtain a continuous curve.

increasing the grid resolution improves our sampling of those peaks, it introduces numerical artefacts and substantially increases the computation time. A similar issue arises in regions very close to synchronisation, where the tidal amplitude varies rapidly with the orbital period. Nonetheless, these plots still capture the overall behaviour and provide valuable physical insight for a fixed rotation rate and temperature. *We should hence note that the number of potential resonance locking points is likely underestimated.*

As a final remark on Figure 6.1, the "*bucket*" behaviour of the tidal effect on the semi-major axis is clearly seen on the right. The corresponding decline in tidal efficiency at larger separations (left side of the plot) has been omitted from the figure because it was significantly less pronounced. In Figure 6.2, we show a scan of the same system at 10% of critical rotation, extending to larger orbital periods. This supplementary figure clearly displays the bucket behaviour on the left. In both cases, the decline of tidal efficiency at larger separations still falls off more rapidly than the gravitational wave contribution, making intersections there unlikely.

We will now review how the mass, temperature and rotation of C-O white dwarfs affect the combined influence of tides and gravitational waves on the semi-major axis. We will also compare these models to the He core white dwarf model, mostly to investigate the effect of core composition on the oscillations. As before, the companion is treated as a point mass of the same mass as the primary, so only tides raised on the primary are included. This simplification does not alter our conclusions.[6] Due to the sign-related problem encountered in the super-synchronous regime, we will only consider the sub-synchronous regime in the next section.

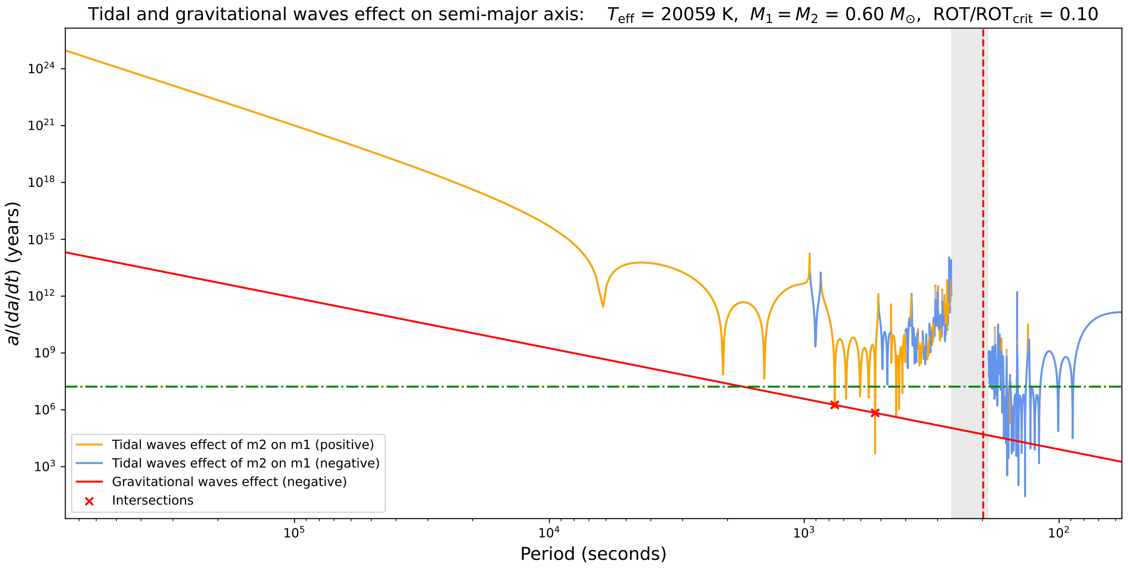

Figure 6.2: Extended plot of a period scan of the $a/(da/dt)$ from gravitational waves and tides for a binary system of 0.6 $M_\odot$ white dwarfs where the secondary is treated as a point mass. The rotation of the primary is set to 10% of its critical rotation.

---

[6] If the companion was also deformed, the total number of potential resonance locking points and kicks would merely double, and the peak amplitudes would increase by at most a factor of two—negligible given the orders of magnitude over which tidal effects vary.

Effect of temperature

For our white dwarf models of various masses, the full cooling sequence is available, allowing each effective temperature to be associated with a corresponding stellar age. To compare the different sequences, we initially selected four models per sequence: one before entry into the ZZ Ceti instability strip (around 20000 K), one on the blue edge (around 13000 K), and two within the strip (around 11500 and 10800 K). No models were chosen near the red edge, as its precise location is uncertain and our results in that region may therefore be less reliable. This model selection works well for the 0.4 and 0.6 $M_\odot$ white dwarfs. However, as the entry temperature into the instability strip also depends on $\log g$, and thus on mass, this selection was not suitable for the 0.2 $M_\odot$ model. Lower-mass white dwarfs enter the instability strip at lower temperatures, and in addition, according to the evolutionary models, 0.2 $M_\odot$ white dwarfs never reach temperatures as high as $\sim$ 20000 K. Consequently, we selected the first and warmest available 0.2 $M_\odot$ model at $\sim$ 18000 K and added a model at $\sim$ 10100 K to include a case within the instability strip.

To isolate the effect of temperature on the oscillations, let us focus on the 0.6 $M_\odot$ white dwarf evolution sequence. Models of this white dwarf sequence at the four selected effective temperatures are shown in Figure 6.3, the last two lying within the instability strip. For these models, we kept the ratio of the star's rotation rate to its critical rotation fixed. As a result of the cooling and contraction of the star, the critical rotation frequency and thus angular frequency of the star varies slightly between models. However, this nuance does not affect our overall conclusions.

The primary effect of cooling appears as the star enters the instability strip, where the prograde modes become unstable. Hence, the intersections before synchronisation can only be *kicks*, whereas the intersections correspond to resonance locking points within the instability strip. No significant change in the absolute amplitude of the tidal effects is observed. While the cooling timescale naturally increases as the star cools, this variation remains modest and should not substantially alter the overall behaviour of the systems when studying orbital evolution.

From our results, it appears that the typical cooling timescale near synchronisation is slower by several orders of magnitude than the timescale of evolution of the semi-major axis. *As a consequence, the orbital evolution will be faster than the instability strip crossing.*

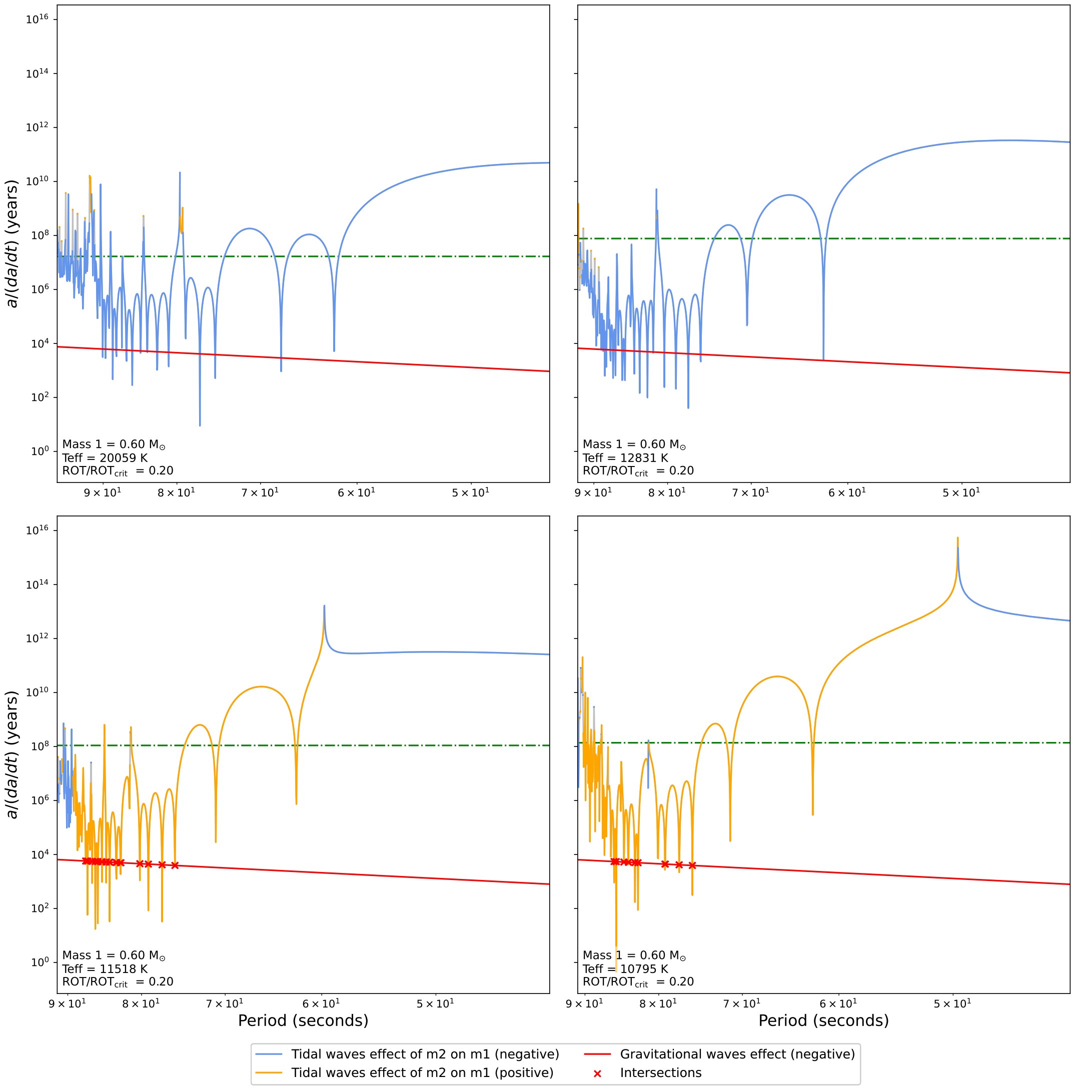

Figure 6.3: Comparison of $a/(da/dt)$ for different temperature of the 0.6 $M_\odot$ model, with constant fraction of the critical rotation.

Effect of mass and rotation

To illustrate the effects of mass and rotation on the semi-major axis evolution timescale, Figure 6.4 presents four panels summarising these two parameters. In each row the mass (and effective temperature) is held fixed, while the rotation fraction ($\mathrm{ROT}/\mathrm{ROT}_{\mathrm{crit}}$) increases from left to right. The temperatures were chosen so that every model lies within the instability strip.

In Figure 6.4, when decreasing the mass, the gravitational wave curve for $a/(da/dt)$ rises by roughly three orders of magnitude in the two left panels and by two orders of magnitude in the two right panels. The tidal curve also rises, but more slowly, so it approaches the gravitational wave curve more closely at lower masses, leading to more intersections. For the rapidly rotating, low-mass model, the tidal curve even appears stronger than the gravitational wave curve over a small range of periods, creating a *locking region* where the system can lock without the aid of resonance. A precise quantification using the MAD_tides outputs is challenging, however, because there is no natural reference level for the tidal response.

A theoretical argument helps to explain this behaviour. Restricting to circular orbits and the $l = 2$, $m = \pm 2$ modes, Eqs. (3.49) and (4.4) reduce to:

$$\left(\frac{da}{dt}\right)_{\mathrm{GW}} = -\frac{64}{5}\,\frac{G^3\,M_1\,M_2\,(M_1+M_2)}{c^5\,a^3}, \tag{6.3}$$

$$\left(\frac{da}{dt}\right)_{\mathrm{Tides}} = 4\,\Omega_{\mathrm{orb}}\,\frac{M_2}{M_1}\,\frac{R_1^5}{a^4}\,\mathrm{Im}(F_{2,\pm2,\mp2})\,G^{(2)}_{2,\pm2,\mp2}(0). \tag{6.4}$$

Increasing the mass affects both tides and gravitational waves directly and indirectly via the radius: more massive white dwarfs have smaller radii (for example, the 0.2 $M_\odot$ model has twice the radius of the 0.6 $M_\odot$ model). Since the fraction of critical rotation is held constant, the synchronisation frequency, and hence the sub-synchronous separations a, also changes with mass and radius. To isolate the mass and radius dependence, we evaluate the expressions at synchronisation, where

$$f \equiv \mathrm{ROT}/\mathrm{ROT}_{\mathrm{crit}} = \Omega_{\mathrm{orb}}\sqrt{\frac{R_1^3}{G\,M_1}} \quad\Longrightarrow\quad a = \left(\frac{M_1+M_2}{f^2\,M_1}\right)^{1/3} R_1, \tag{6.5}$$

using Kepler's third law. Substituting into the two rates gives, for twin systems ($M_1 = M_2 = m$),

$$\left(\frac{da}{dt}\right)_{\mathrm{GW}} = -\frac{64}{5}\,\frac{G^3}{c^5}\,\frac{m^3\,f^2}{R_1^3}, \tag{6.6}$$

$$\left(\frac{da}{dt}\right)_{\mathrm{Tides}} = 2^{2/3}\,G^{1/2}\,\frac{m^{1/2}\;f^{11/3}}{R_1^{1/2}}\,\mathrm{Im}(F_{2,\pm2,\mp2})\,G^{(2)}_{2,\pm2,\mp2}(0). \tag{6.7}$$

This yields for the timescales of evolution of semi-major axis:

$$\frac{a}{(da/dt)_{\mathrm{GW}}} = -\frac{5}{2^{17/3}}\frac{c^5}{G^3}\frac{R_1^4}{m^3\,f^{8/3}}, \tag{6.8}$$

$$\frac{a}{(da/dt)_{\mathrm{Tides}}} = \frac{2^{-1/3}}{G^{1/2}\,\mathrm{Im}(F_{2,\pm2,\mp2})\,G^{(2)}_{2,\pm2,\mp2}(0)}\,\frac{R_1^{3/2}}{f^{13/3}\,m^{1/2}}. \tag{6.9}$$

These scalings explain the trends seen in Figure 6.4: increasing the dimensionless rotation frequency f strengthens more tides than gravitational waves, and thus yields more intersections. While increasing m and decreasing R_1 boost both effects, gravitational waves gain relatively more in intensity. The role of $\mathrm{Im}(F_{2,\pm 2,\mp 2})$ remains similar across the models.

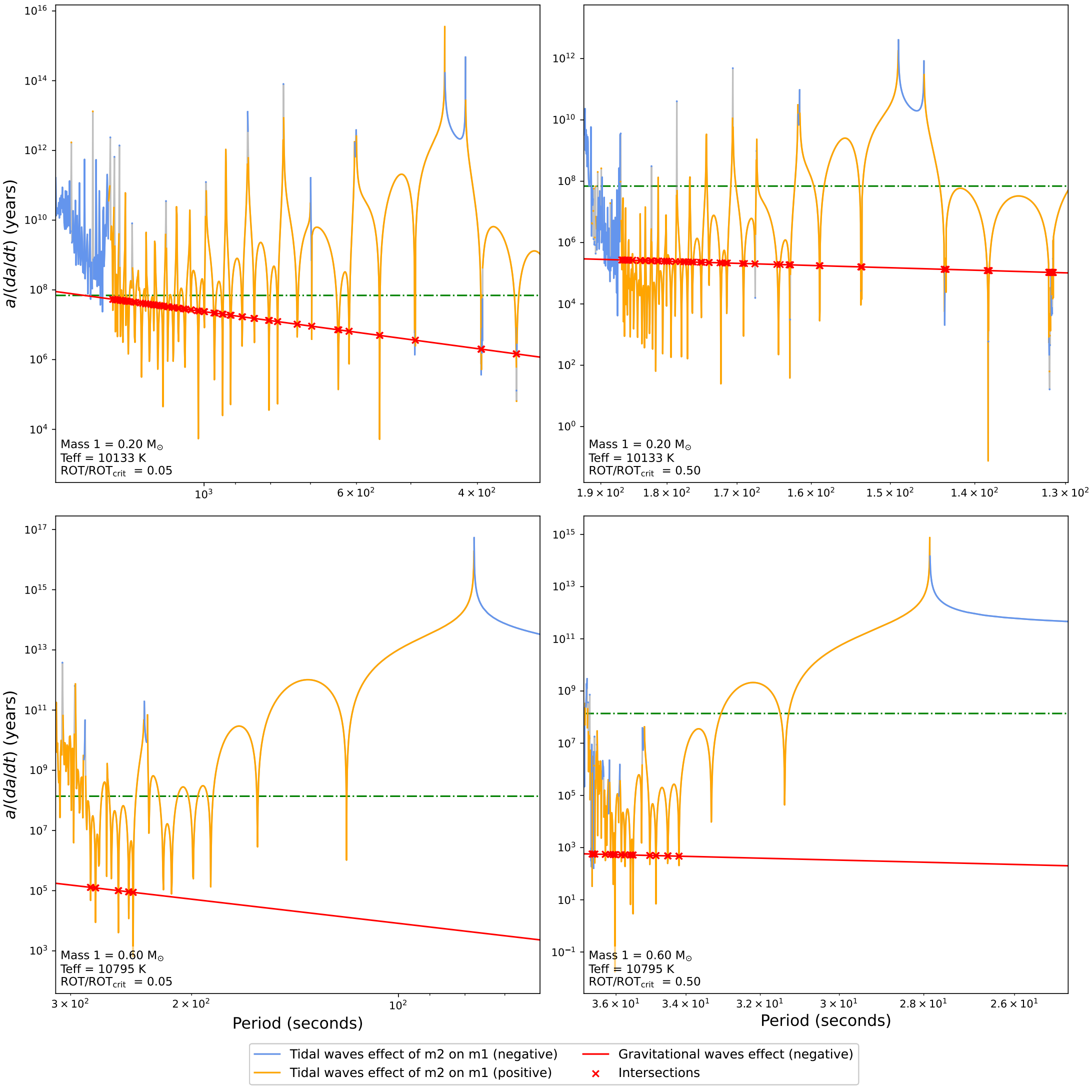

Figure 6.4: Comparison of $a/(da/dt)$ for different masses and rotation $(\mathrm{ROT}/\mathrm{ROT}_{\mathrm{crit}})$. The upper plots corresponds to 0.2 $M_\odot$ and the lower to 0.6 $M_\odot$. The left column corresponds to a slow rotation of $\mathrm{ROT}/\mathrm{ROT}_{\mathrm{crit}} = 0.05$, while the right column corresponds to a fast rotation of $\mathrm{ROT}/\mathrm{ROT}_{\mathrm{crit}} = 0.5$. The effective temperatures were chosen such that each model lies within the instability strip. The period ranges are selected to begin directly after each system reaches synchronisation and cover the region of the sub-synchronous regime where tides are strongest.

To complement this analysis, Figure 6.5 illustrates the effect of mass alone by comparing four different masses at fixed rotation. We see that tidal effects clearly surpass gravitational wave effects only for the $0.2\,M_\odot$ model. As soon as the mass increases—even by $0.05\,M_\odot$ between the two lighter models—tides lose efficiency compared to gravitational waves.

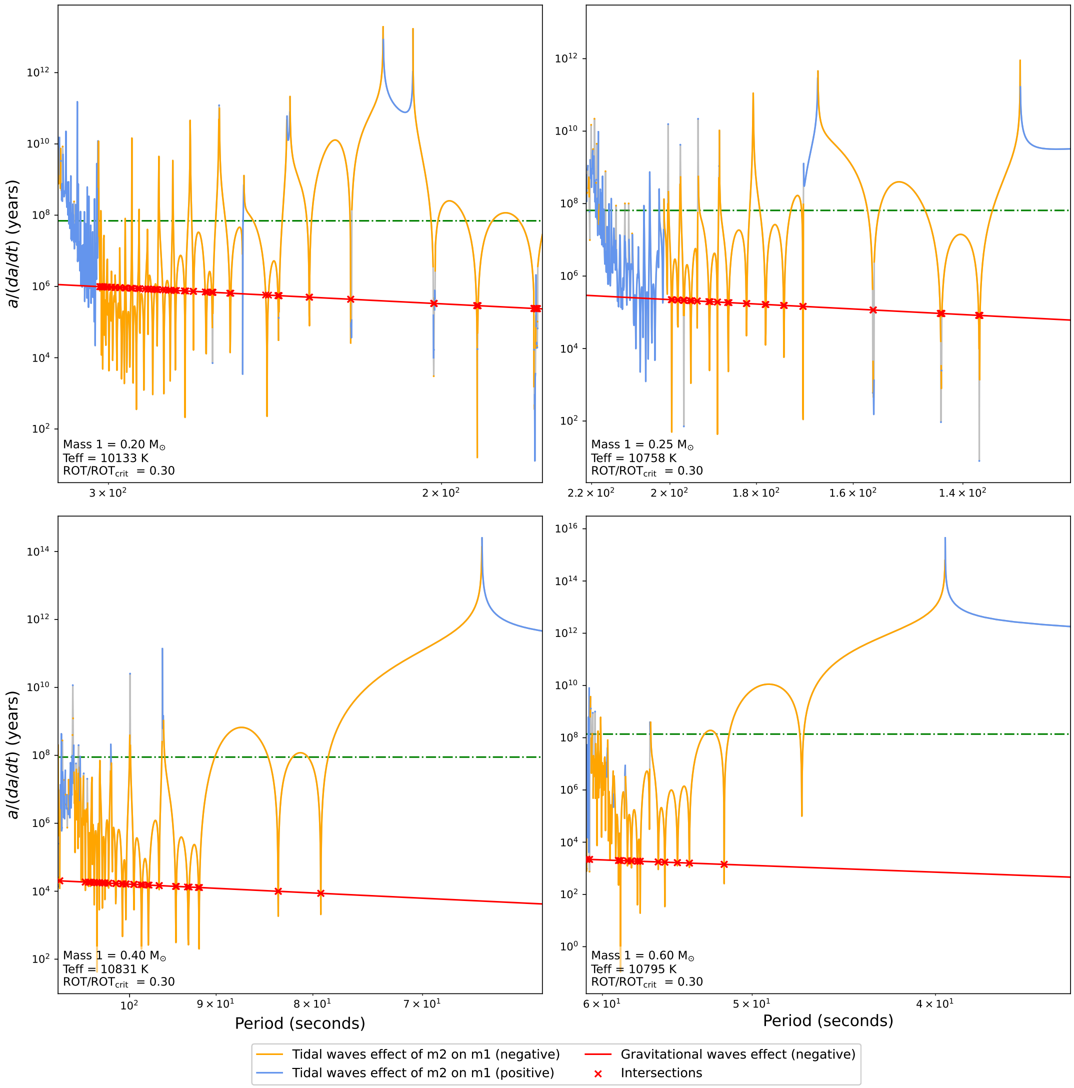

Figure 6.5: Comparison of $a/(da/dt)$ for different values of mass. The rotation ($\mathrm{ROT}/\mathrm{ROT}_{\mathrm{crit}} = 0.3$) is kept the same for all the plots. The effective temperature is chosen such that each model lie within the instability strip. The period ranges are selected to begin directly after each system reaches synchronisation and cover the region of the sub-synchronous regime where tides are strongest.

Figure 6.6 shows, for a given mass, $a/(da/dt)$ for four different fractions of critical rotation. We see that increasing rotation has a more pronounced impact when the rotation is low. At high rotation rates, further increases do not significantly affect the results.

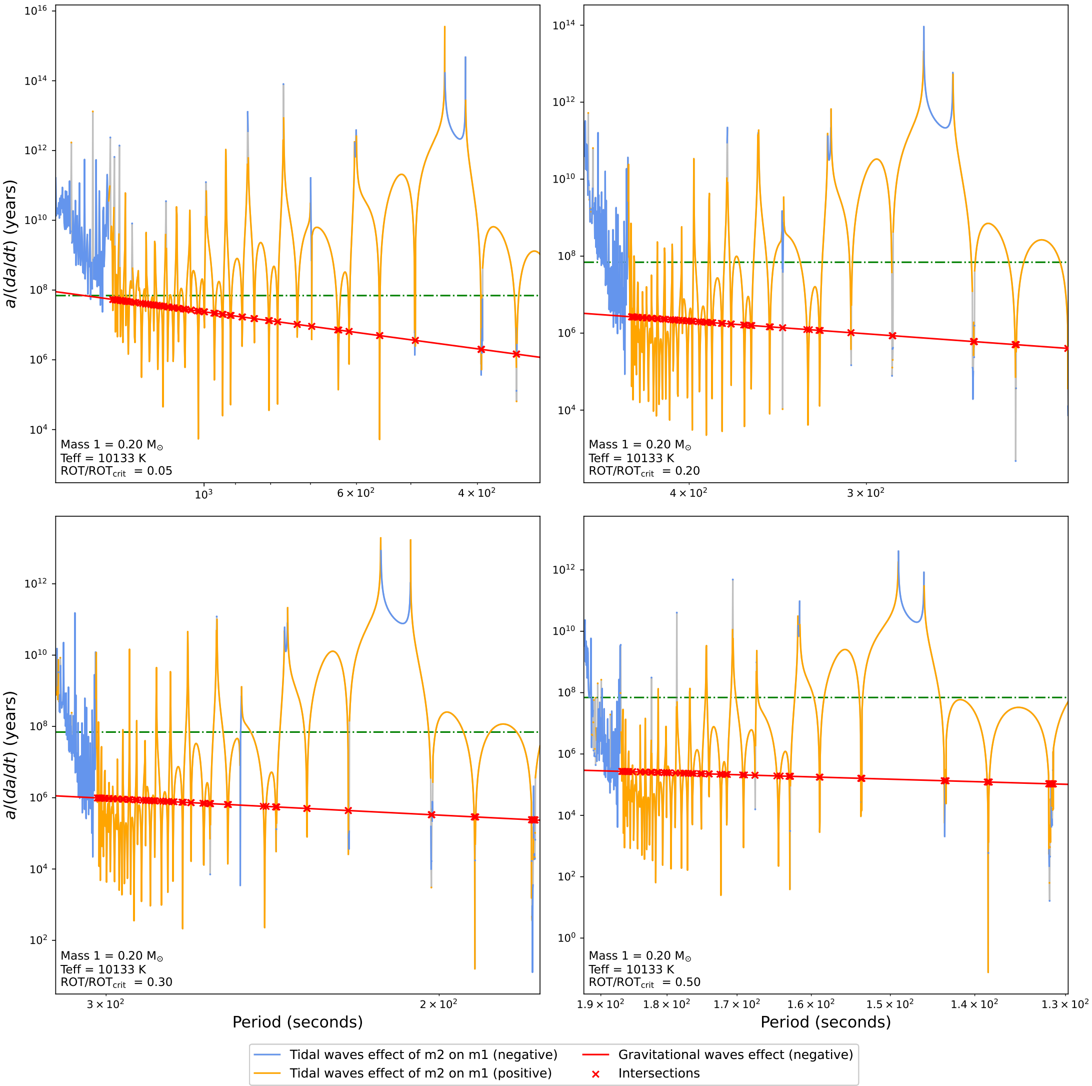

Figure 6.6: Comparison of $a/(da/dt)$ for different values of rotation (ROT/ROT$_{\text{crit}}$). The mass ($0.2\ M_\odot$) and effective temperature (10133 K) are kept the same for all the plots. The period ranges are selected to begin directly after each system reaches synchronisation and cover the region of the sub-synchronous regime where tides are strongest.

Finally, Figure D.5 in Appendix D presents the same comparison as Figure 6.4 but for a system prior to instability strip entry. The conclusions are analogous, with an emphasis on tidal kicks rather than resonance locking points before strip entry.

Effect of core composition

In Figure 6.7, we compare the effect of core composition on the evolution timescale of the semi-major axis. The carbon–oxygen core model clearly yields more resonance locking points than the helium-core model. This difference may be due to their contrasting stellar radii: the C–O white dwarf has a radius of 3.1×10^9 cm, whereas the He white dwarf's radius is 1.8×10^{10} cm. However, at fixed mass and rotation, Eqs. (6.6) and (6.7) indicate that increasing the radius should favour tides more than gravitational waves. Yet in Figure 6.7, tides are stronger for the C–O core white dwarf. Inspecting MAD_tides outputs shows that $\mathrm{Im}(F_{2,-2,2})$ is about three orders of magnitude larger for the C–O core than for the He core, explaining the observed modulation. Core composition therefore affects the tidal response, which influences the effect of tides on the semi-major axis beyond the modification of the stellar radius.

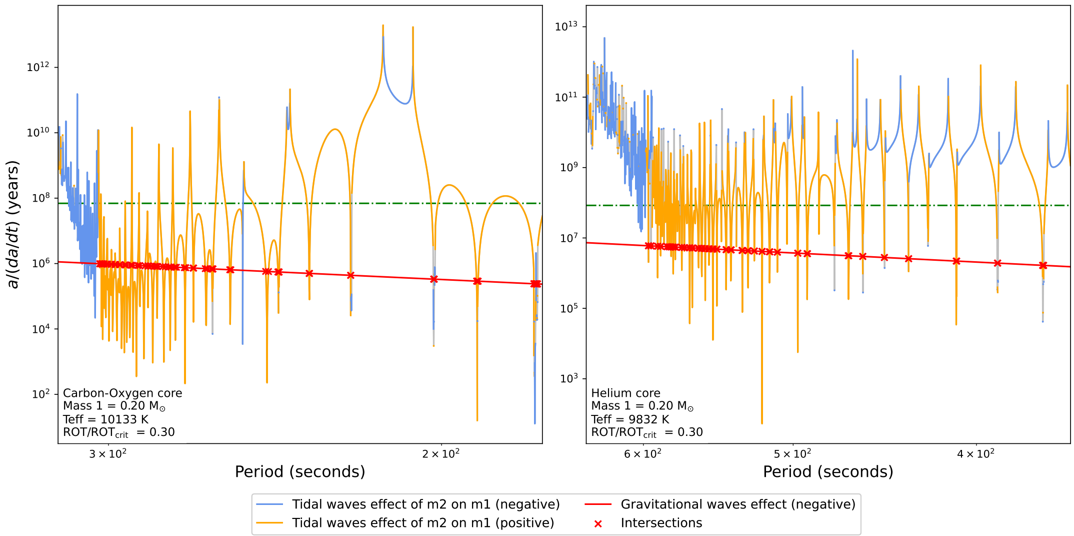

Figure 6.7: Comparison of $a/(da/dt)$ two 0.2 $M_\odot$ white dwarfs of different core composition. The white dwarf on the left has a carbon-oxygen core while the one on the right has a helium core. The effective temperatures were chosen such that each model lies within the instability strip. $\mathrm{ROT}/\mathrm{ROT}_{\mathrm{crit}}$ is kept constant.

6.2 Adding the effect of eccentricity

Going beyond the pure circular case, it is interesting to consider the effect of eccentricity when modelling the effect of tides and gravitational waves on the semi-major axis. Accounting for eccentricity in the calculation of $a/(da/dt)$ due to gravitational waves is straightforward, since Peters' eccentricity-dependent formula for da/dt (Eq. (4.1)) can be implemented directly.

By contrast, eccentricity significantly complicates the computation of the tidal interaction compared to the circular case. Fortunately, MAD_tides already handles arbitrary eccentricity and secondary mass by design, so only the treatment of its outputs needs adjustment. In practice, adding eccentricity in the tidal computation introduces several extra steps beyond the circular case. Indeed, when $e = 0$, the Hansen coefficients reduce to $X_k^{n,-m} = \delta_{k,-m}$, but for $e > 0$ one must consider modes with $k \neq -m$ and compute the full Hansen coefficients.

First, because the Hansen coefficients involve the mean anomaly $\mathcal{M}$, we must recover $\mathcal{M}(\nu)$ exactly from the true anomaly ν by solving Kepler's equation

$$\mathcal{M} \;=\; E \;-\; e\,\sin E. \tag{6.10}$$

This requires obtaining the eccentric anomaly from the true anomaly via

$$E \;=\; 2\,\arctan\left[\sqrt{\frac{1-e}{1+e}}\;\tan\left(\frac{\nu}{2}\right)\right]. \tag{6.11}$$

Since the standard `atan` function returns values in $\left]-\frac{\pi}{2}, \frac{\pi}{2}\right[$ while E spans $[0, 2\pi[$, we use NumPy's quadrant-safe `arctan2` to obtain E unambiguously, and hence $\mathcal{M}$.

With $\mathcal{M}(\nu)$ in hand, we compute the Hansen coefficients via Eq. (3.35), using SciPy's `integrate.quad` for the integral. These coefficients are then substituted into the definition of $c_{l,m,k}$ (Eq. (3.31)), where $P_l^{|m|}(0)$ is evaluated via SciPy's `special.lpmv`.[7] Next, we assemble $g^{(2)}_{l,m,k}$ by combining $c_{l,m,k}$, another factor $P_l^{|m|}(0)$, and performing the two integrals over ν from Eq. (3.39). Finally, the result is inserted into Eq. (3.38) to obtain the tidal da/dt as a function of eccentricity. The Python functions that were implemented in this work to compute da/dt for a given mode (l, m, k) in the eccentric case are provided in Appendix C.

In the following, we apply this approach to the sub-synchronous regime of orbital frequencies. As noted above, for $e > 0$ modes beyond $k = -m$ can be excited. In particular, for $(l = 2,\, m = -2)$, we include the modes for $k \in \{2,\, 3,\, 4\}$. Crucially, we do *not* have to recompute the full tidal response for each new k. Instead, we reuse the MAD_tides output originally generated for $k = 2$. For each orbital period $P_{\rm orb}$, we compute

$$\sigma_{k,m} \;=\; k\,\Omega_{\rm orb} \;+\; m\,\Omega_{\rm rot}, \tag{6.12}$$

then look up (by linear interpolation) the pre-computed value of $\operatorname{Im}\psi$ corresponding to $\sigma_{k,m}$. In other words, MAD_tides already provides a dense table of $\operatorname{Im}\psi(\sigma\, t_{\rm dyn})$ for all relevant σ at $k = 2$, and we simply extract the matching response whenever $\sigma_{k,m}$ lies within that original range for $k > 2$.

---

[7] We also compute d_{lm} at this stage, which likewise requires `special.lpmv`.

As k increases, the entire window of forcing frequencies

$$\sigma_{k,-2} \;=\; k\,\Omega_{\mathrm{orb}} \;-\; 2\,\Omega_{\mathrm{rot}} \tag{6.13}$$

shifts to higher values. Since MAD_tides was run only over a finite interval $\left[\sigma_{\min}^{(2)},\, \sigma_{\max}^{(2)}\right]$, the contribution of each k can be computed only if

$$\sigma_{k,-2} \;\in\; \left[\sigma_{\min}^{(2)},\, \sigma_{\max}^{(2)}\right]. \tag{6.14}$$

For a given rotation Ω_{rot}, one converts these frequency endpoints back into bounds on P_{orb} for each k, denoted $\left[P_{\min}^{(k)},\, P_{\max}^{(k)}\right]$. The only period range where all three modes ($k = 2, 3, 4$) lie within the pre-computed grid is

$$\left[P_{\min}^{(\mathrm{all})},\, P_{\max}^{(\mathrm{all})}\right] \;=\; \bigcap_{k=2}^{4} \left[P_{\min}^{(k)},\, P_{\max}^{(k)}\right]. \tag{6.15}$$

Whenever P_{orb} lies outside this intersection, one or more of the $\sigma_{k,-2}$ has no corresponding tidal response, so its contribution is set to zero. As k grows, the intersection interval shrinks and eventually vanishes.

At large Ω_{rot}, the frequency range for which MAD_tides computed the response at $k = 2$ is already narrow. Consequently, already by $k = 3$, there may be no computed forcing frequencies for any $\sigma_{3,-2}(P)$. For this reason, we restrict our figures to rotation rates up to 25% of critical, where some overlap remains.

In practice, we set $k_{\max} = 4$, since higher k-terms are negligible and lie out of range. For each period where the tidal effect of the $k = 2$ mode was computed, we add the contributions of $k = 3$ and $k = 4$ whenever possible. Because those contributions are small relative to $k = 2$, adding them only locally does not alter our main conclusions.

Before presenting our eccentric case results, Figure 6.8 shows $a/(da/dt)$ for circular systems of $0.2\,M_\odot$ and $0.6\,M_\odot$ white dwarfs at rotation rates of 5% and 25% of critical. We use these same parameters for the eccentric cases, providing a direct basis for comparison.

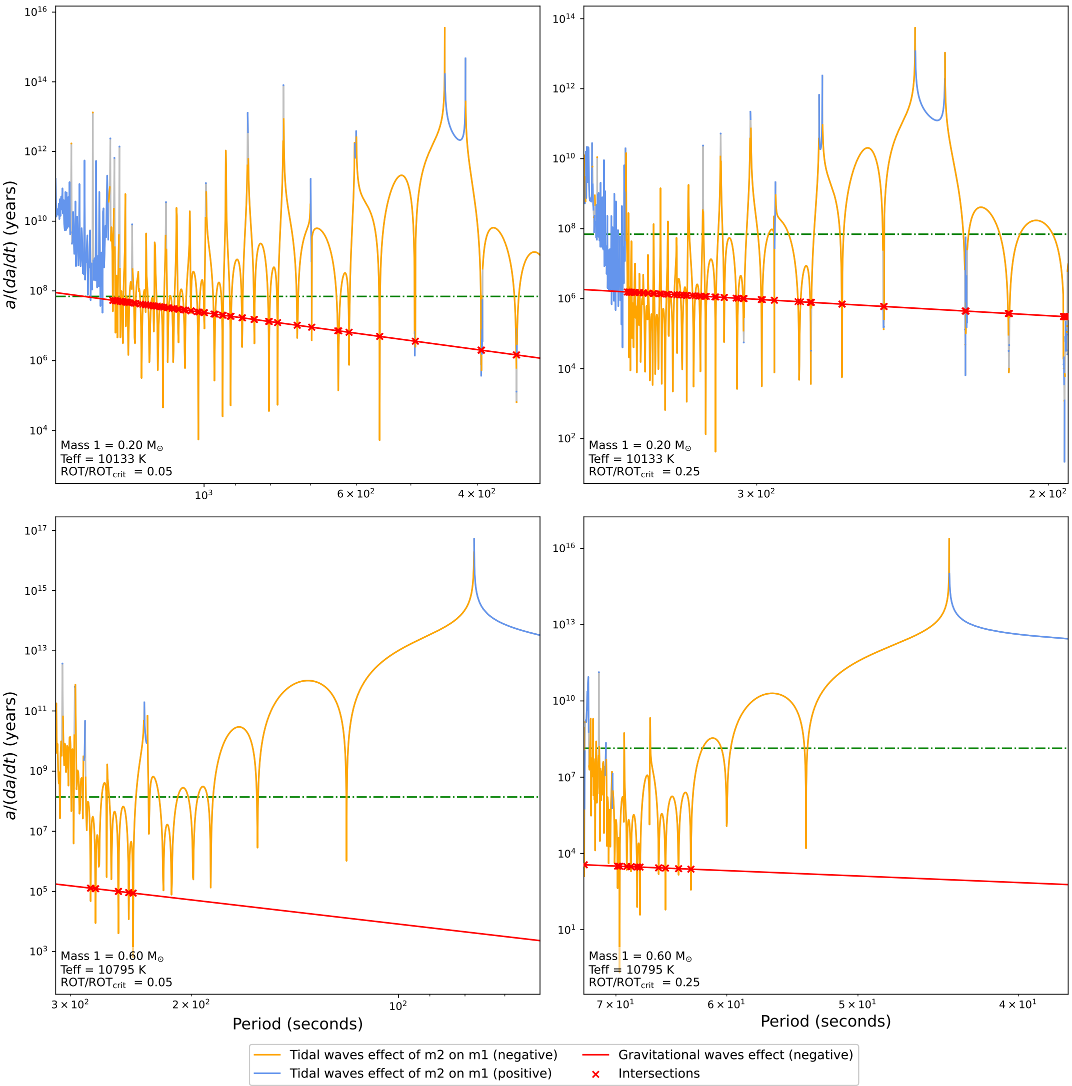

Figure 6.8: Comparison of $a/(da/dt)$ for different masses and rotation ($\mathrm{ROT}/\mathrm{ROT}_{\mathrm{crit}}$) **with no eccentricity** ($e = 0$). The upper plots corresponds to 0.2 $M_\odot$ and the lower to 0.6 $M_\odot$. The left column corresponds to a slow rotation of $\mathrm{ROT}/\mathrm{ROT}_{\mathrm{crit}} = 0.05$, while the right column corresponds to a faster rotation of $\mathrm{ROT}/\mathrm{ROT}_{\mathrm{crit}} = 0.25$. The effective temperatures were chosen such that each model lies within the instability strip. The period ranges are selected to begin directly after each system reaches synchronisation and cover the region of the sub-synchronous regime where tides are strongest.

In Figure 6.9, we set the eccentricity to $e = 0.1$. The overall behaviour remains similar to the circular case, with no noticeable enhancement in either tidal or gravitational wave curves.

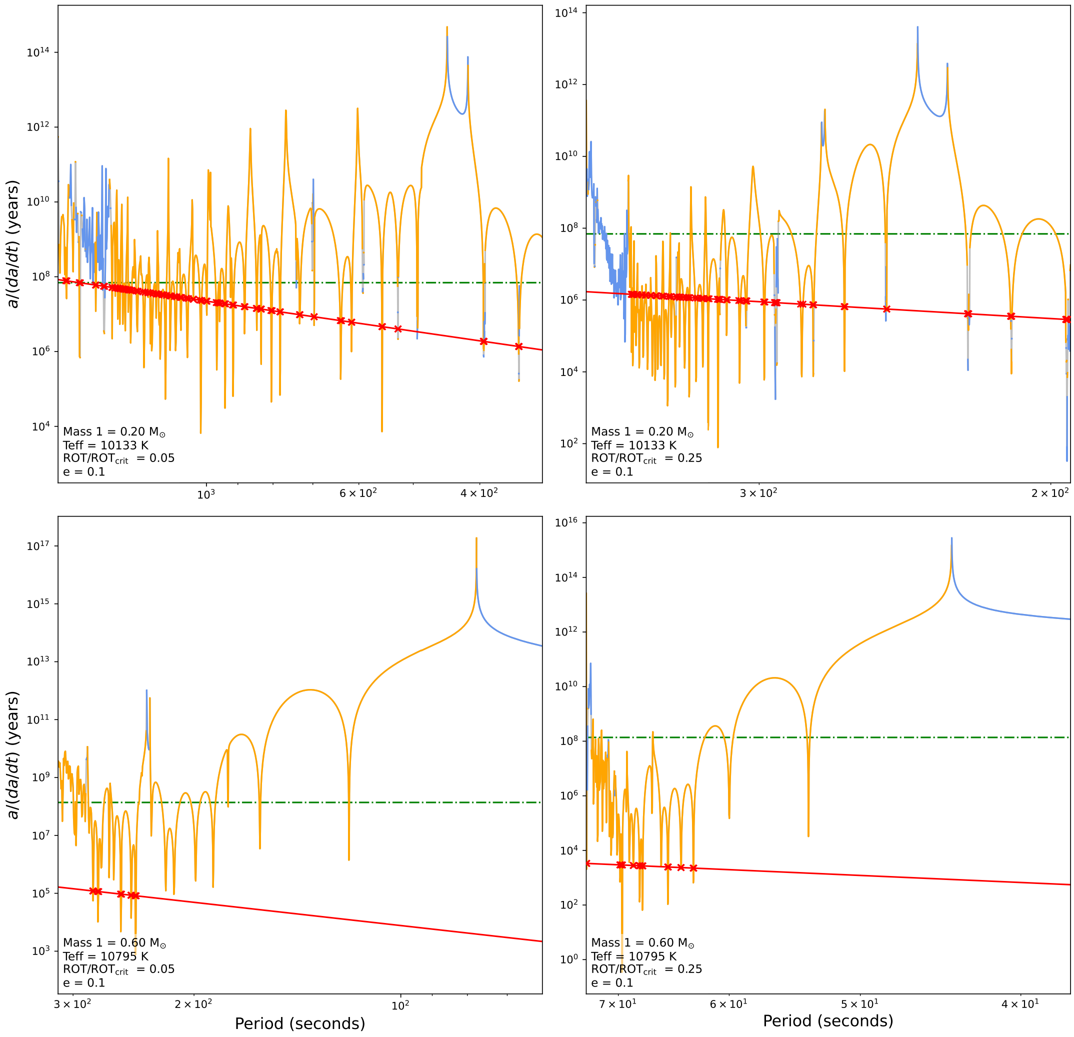

Figure 6.9: Comparison of $a/(da/dt)$ for different masses and rotation (ROT/ROT$_{\rm crit}$) with an eccentricity of $e = 0.1$. The upper plots corresponds to 0.2 $M_\odot$ and the lower to 0.6 $M_\odot$. The left column corresponds to a slow rotation of ROT/ROT$_{\rm crit}$ = 0.05, while the right column corresponds to a faster rotation of ROT/ROT$_{\rm crit}$ = 0.25. The effective temperatures were chosen such that each model lies within the instability strip. The period ranges are selected to begin directly after each system reaches synchronisation and cover the region of the sub-synchronous regime where tides are strongest.

Raising the eccentricity to $e = 0.4$, Figure 6.10 reveals the eccentricity's effect more clearly. The horizontal line marking the cooling timescale remains unchanged across subplots, which can thus be used to facilitate comparison. Both tidal and gravitational wave amplitudes increase, though the enhancement is stronger for gravitational waves than for tides.

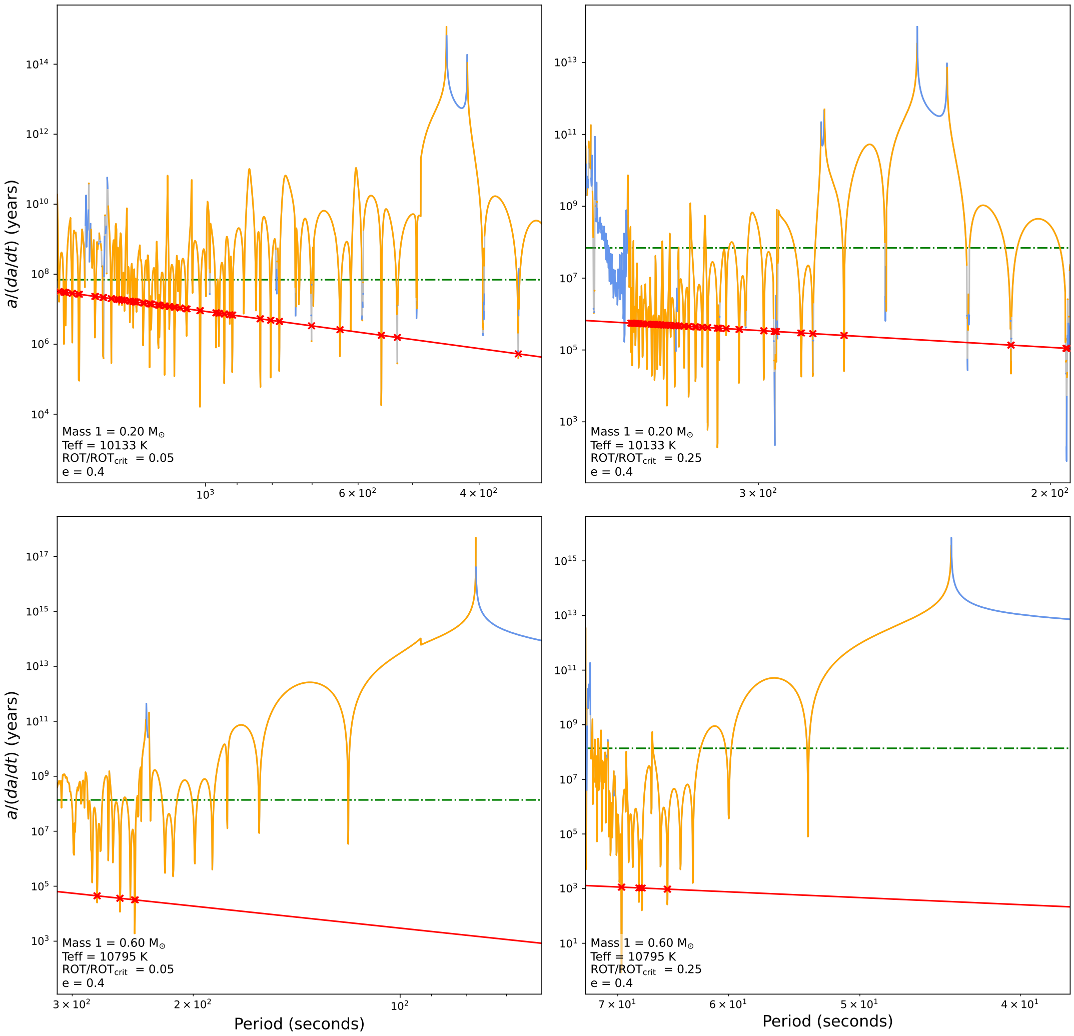

Figure 6.10: Comparison of $a/(da/dt)$ for different masses and rotation ($\mathrm{ROT}/\mathrm{ROT}_{\mathrm{crit}}$) with an eccentricity of $e = 0.4$. The upper plots corresponds to $0.2\ M_\odot$ and the lower to $0.6\ M_\odot$. The left column corresponds to a slow rotation of $\mathrm{ROT}/\mathrm{ROT}_{\mathrm{crit}} = 0.05$, while the right column corresponds to a faster rotation of $\mathrm{ROT}/\mathrm{ROT}_{\mathrm{crit}} = 0.25$. The effective temperatures were chosen such that each model lies within the instability strip. The period ranges are selected to begin directly after each system reaches synchronisation and cover the region of the sub-synchronous regime where tides are strongest.

At even higher eccentricities, one would observe a greater separation between the tidal and gravitational wave curves. However, when e grows, higher k modes begin to contribute significantly, making our results less reliable unless those modes are fully included.

Another consequence of non-zero eccentricity is that the drop in tidal intensity near synchronisation is less pronounced. High order k modes fill in the gap that appears in the circular case. Strictly speaking, genuine synchronisation does not occur in an eccentric orbit—one instead refers to *pseudo-synchronisation*[8]. Moreover, retrograde modes are no longer confined to the super-synchronous regime and should also be accounted for, particularly at large e.

In conclusion, while increasing eccentricity boosts both tidal and gravitational wave strengths, it tends to reduce the number of intersection points—an effect noticeable only at high eccentricities. As a final note, a full study of the evolution of eccentric systems would also require including the tidal and gravitational wave effects on eccentricity (Eqs. (3.41) and (4.2)). It would also be of prime interest to extend the analysis to larger separations—particularly the super-synchronous regime—and to account for a greater variety of modes in future work.

6.3 Orbital evolution code

The most rigorous way to study the behaviour at locking and kick points is to use an iterative evolution code that computes the orbital parameters step by step. In this work, we adapted the TREMOR code originally presented in Fellay, 2025 (submitted), which incorporates the MAD code and was designed for nuclear-burning stars in binaries. At each time step, the code evaluates which oscillation modes have the greatest impact on the orbital parameters, then updates the separation, eccentricity and stellar rotations accordingly.

Unfortunately, adapting TREMOR to white dwarf binaries revealed significant difficulties, most likely due to the extremely strong and narrow resonance peaks in these systems. Away from resonances and kicks, the code performed as expected as gravitational wave emission led smaller separations. However, whenever a strong resonance peak was encountered, either the orbital parameters would change by a large amount within a single iteration, or the code would crash. Drastically reducing the time steps failed to solve the problem. After investigating for potential sources of errors within the code, no solution was found and we decided to concentrate our efforts on other aspects of this work.

---

[8] In an eccentric binary, the star's angular velocity varies as it travels along its orbit. If its instantaneous spin matches the orbital angular velocity at periastron, the system is often said to be in a state of pseudo-synchronisation. Rigorously, we should therefore not speak of super- and sub-synchronous regimes in the eccentric case, but here we use these terms to denote the corresponding ranges as defined for the circularised case.

Chapter 7

Resonance Locking Parameter Space and Observational Comparison

A key objective of this work is to identify the region in parameter space where a white dwarf binary system must lie to encounter locking points during its evolution. Due to the sign problem in the super-synchronous regime mentioned earlier, we do not investigate that case further here. However, it is clear that locking points—though fewer in number—also occur in this regime. Because super-synchronous locking points theoretically appear when the white dwarf is *outside* the instability strip, their initial conditions are likely less restrictive than those presented below.

In this chapter, we therefore determine these constraints for sub-synchronous locking points and compare them to observed binaries to assess whether such systems exist in nature. This methodology could similarly be applied to systems encountering super-synchronous locking points.

7.1 Finding the initial conditions

One could determine the constrained parameter space by running an orbital evolution code backward, since the governing equations are deterministic. However, solutions of good accuracy can be obtained more simply by integrating the gravitational wave evolution equations for da/dt and de/dt (Eqs. (4.1) and (4.2)) only. Indeed, tidal effect on the orbital elements decrease more rapidly with increasing a than gravitational waves (see Eqs. (6.3) and (6.4)). Tides thus remain negligible over most of the inspiral. They become relevant only near synchronisation and, in particular, at resonances. Hence, **we may safely ignore tidal contributions for most of the evolution.**

As explained at the beginning of this chapter, we consider only sub-synchronous locking points, which appear for white dwarfs **within the instability strip**. If a white dwarf remains in the instability strip as it approaches synchronisation, any super-synchronous resonances it encounters can only produce kicks, since super-synchronous (retrograde) dynamical tides act in concert with gravitational waves when the star lies within the instability strip. Hence, such a white dwarf should encounter locking only in the sub-synchronous regime. Encountering a locking inevitably alters the components' rotation and allows additional cooling while the orbital separation remains fixed. Consequently, subsequent resonance locking points may be shifted. As resonance locking points all lie within a narrow range of separations, any sub-synchronous locking point yields nearly identical backward integrations of the gravitational wave equations, leaving our conclusions about the allowed parameter space unchanged. The first locking event is thus of primary interest and is adopted as the starting condition for integrating the gravitational wave evolution equations.

To complete the backward integration, we need to select a target age, or equivalently a target temperature. In order to obtain evolutionary traces, we defined a grid of target temperatures ranging from the resonance locking temperature up to either a pre-determined maximum temperature or the warmest model available. For each temperature, the corresponding age was determined by interpolating linearly between two evolutionary models of known ages. The coupled ordinary differential equations are then solved with SciPy's `solve_ivp` integrator (SciPy Community, 2025).

The influence of different parameters at resonance locking on the integration must be examined. In the circular case these parameters are the mass of the components, their rotation rates and their temperatures. A preliminary analysis based on the MAD_tides results presented in the previous section showed that rotation has only a minor effect on the initial separations. Indeed, for a given mass, the difference in separation required to reach synchronisation—and the subsequent resonance locking points—at 5% or 50% of the critical rotation is negligible compared to the overall range of initial separations. Moreover, the semi-major axis shrinks increasingly rapidly as the separation decreases, so the time needed to evolve between these two synchronisation separations is negligible compared to the evolution timescale from larger separations. The curves in Figure 7.1 are nearly indistinguishable for the different rotation rates.

By contrast, mass and temperature have a much more pronounced impact on the initial conditions. For the 0.2, 0.4 and 0.6 $M_\odot$ C-O models, we computed tidal and gravitational interactions in the sub-synchronous regime for several successive models within the instability strip using MAD_tides. For the 0.6 $M_\odot$ model, we used evolutionary sequences from the instability strip entry down to 2000 K cooler while for the other masses we used sequences down to 1000 K cooler. Cooler temperatures were not considered due to the large uncertainties approaching the red edge. We adopted rotation rates of 30% and 50% of the critical rotation. Indeed, although rotation has little effect on the initial separations, higher rotation increases the number of resonance locking points, and comparing two rates confirms this tendency.

After identifying the first sub-synchronous resonance locking point, we performed backward integration up to 18000 K, a choice motivated by the availability of models at that temperature for all C-O sequences. The results for 50% of the critical rotation are shown on Figure 7.2. Mass affects the evolution of $a(T_{\text{eff}})$ as one would anticipate: more massive systems—being less luminous—cool more slowly and experience stronger gravitational wave–driven orbital decay, allowing them to reside at larger separations at high temperature before evolving towards resonance locking points.[1] The influence of temperature is straightforward: systems that lock at higher temperature must have evolved from smaller separations at 18000 K than those locking at cooler temperatures. For a given mass, we

---

[1] As before, one also observes the effect of mass on the critical rotation on this figure: more massive systems enter the sub-synchronous regime and encounter resonance locking points at shorter separations.

observe that the curves corresponding to different resonance locking temperatures tend to converge at higher temperatures, indicating that the initial separation is a critical factor to encounter resonance locking.[2] On Figure 7.3, we performed a backward integration for the 0.2 $M_\odot$ He core model up to the highest temperature reached by the evolutionary sequence, which is only of 12250 K. On Figure 7.4, we performed backward integration up to the highest temperature available for each C-O sequence, further extending the range of possible initial temperatures for the more massive sequences.

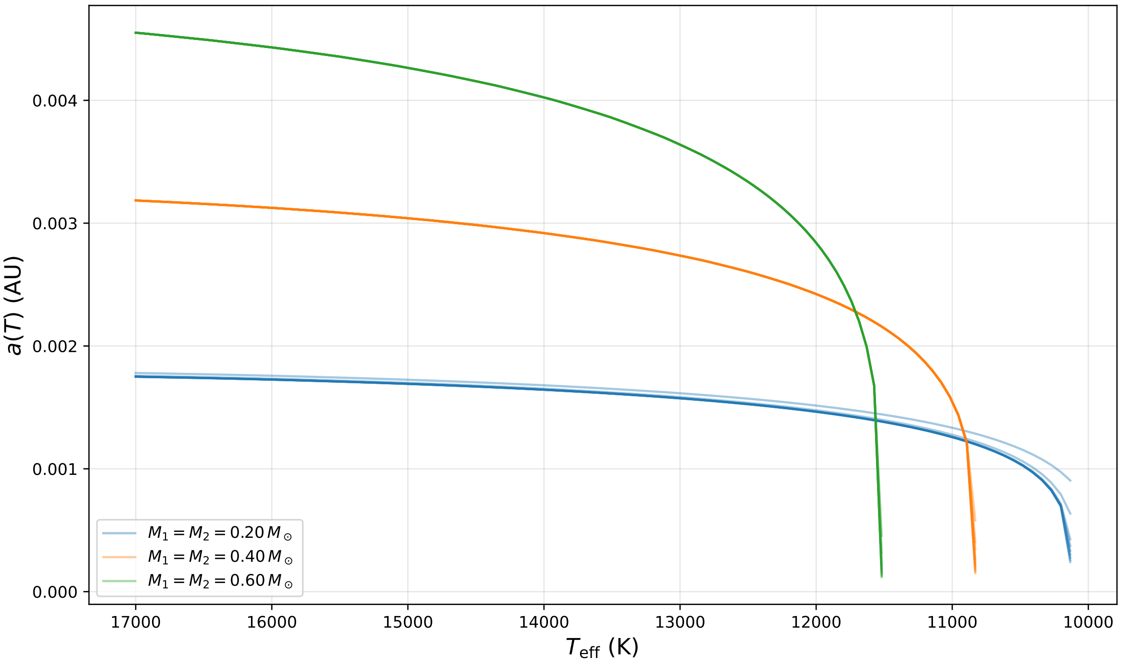

Figure 7.1: Evolution of the separation of binary C-O white dwarfs of different mass, from an initial effective temperature of 17000 K to the first sub-synchronous resonance point encountered at a set temperature for each mass. For each model, the fraction of the critical rotation ranges from 5% to 50%. These different curves are only distinguishable for the 0.2 $M_\odot$ model at resonance locking.

---

[2] A plot at 30% critical rotation, shown in Figure D.6 of Appendix D, shows very similar results for the C-O models.

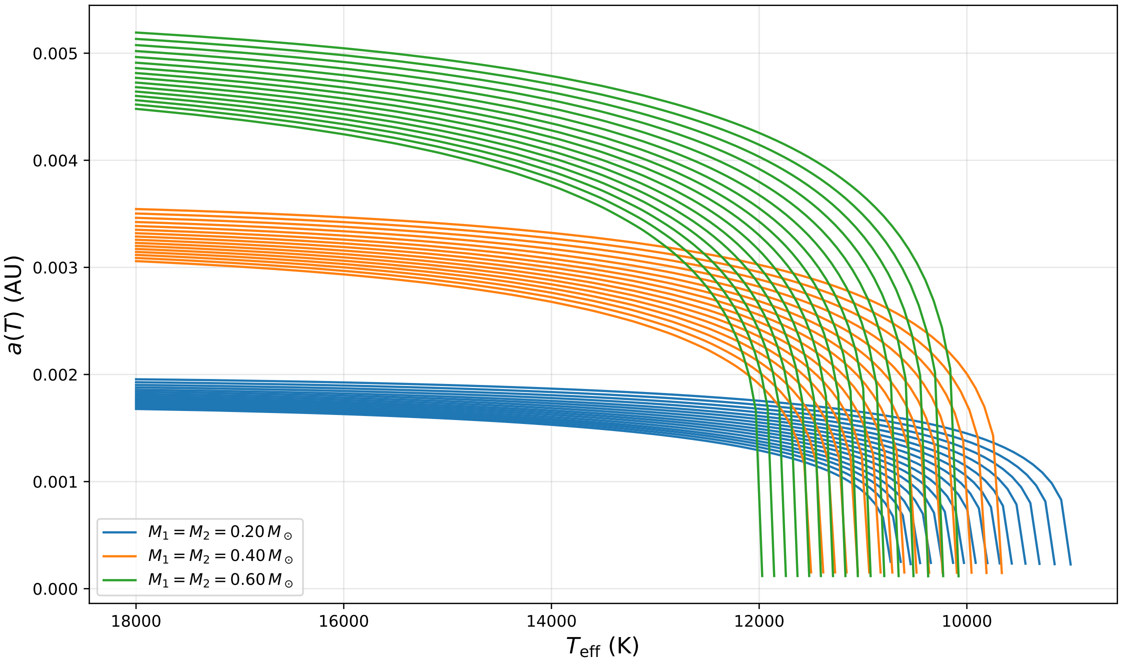

Figure 7.2: Evolution of the separation of binary white dwarfs as a function of effective temperature. The curves are obtained by integrating the gravitational wave equations starting from the first sub-synchronous resonance locking point up to a temperature of 18000 K. The rotation was set to 50% of the critical rotation.

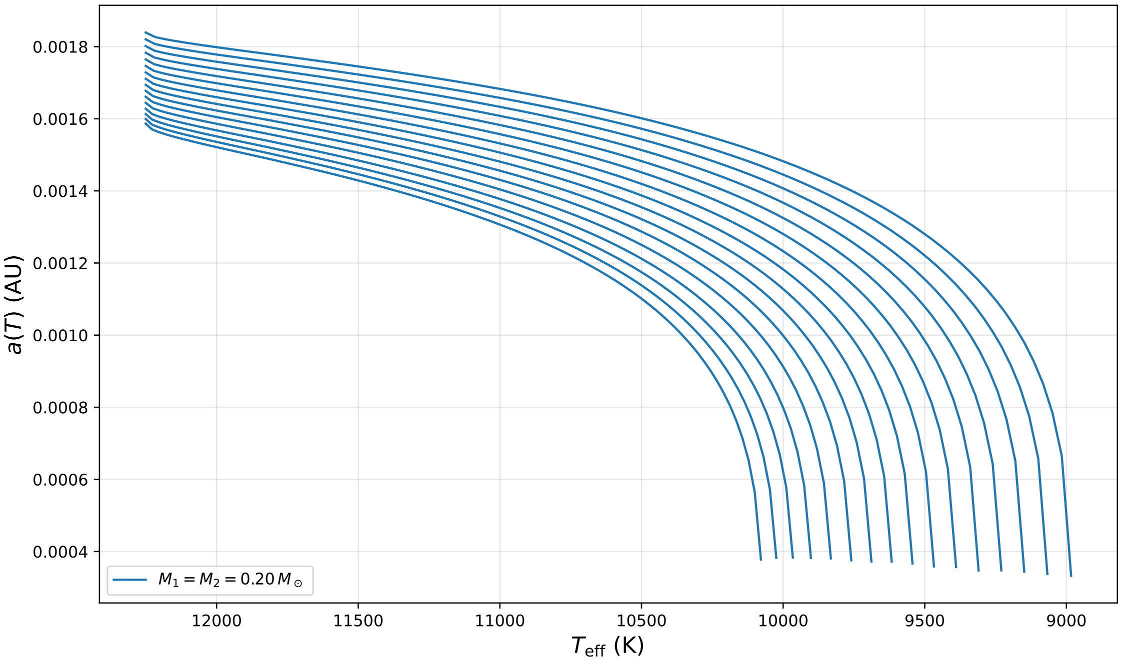

Figure 7.3: Evolution of the separation of binary He white dwarfs as a function of effective temperature. The curves are obtained by integrating the gravitational wave equations starting from the first sub-synchronous resonance locking point up to the highest temperature available for each sequence. The rotation was set to 50% of the critical rotation.

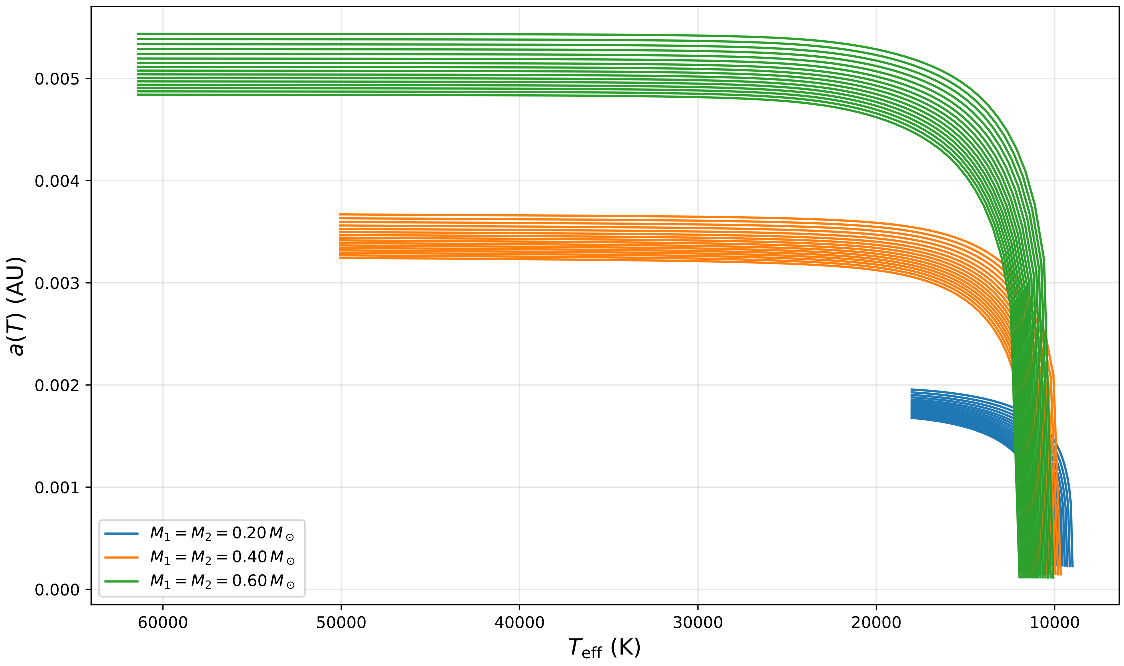

Figure 7.4: Evolution of the separation of binary C-O white dwarfs as a function of effective temperature. The curves are obtained by integrating the gravitational wave equations starting from the first sub-synchronous resonance locking point up to the highest temperature available for each sequence. The rotation was set to 50% of the critical rotation.

7.2 Identifying potential candidates

Based on the initial conditions derived in Section 7.1, only systems with orbital periods below $\sim 10\,000\,\mathrm{s}$ (for twin systems) and containing a DA white dwarf can serve as potential candidates. To verify whether such systems are observed in nature, we compare these criteria against existing white dwarf binary surveys.

Kupfer et al. (2024) compile the shortest period double white dwarf binaries as *verification*[3] and detectable targets for the forthcoming LISA observatory. In that work, the orbital periods and component masses are determined with high precision, since they directly govern the gravitational wave signal. However, effective temperatures are not reported. These latter values are crucial for modelling tidal interactions and unfortunately the temperatures of the systems listed by Kupfer et al. (2024) have only been estimated in dedicated separated studies.

By contrast, Brown et al. (2016), in their Sloan Digital Sky Survey (SDSS) study of extremely low-mass (ELM) white dwarfs, provide for each binary in their sample the orbital period, the mass of both components and the effective temperature of the ELM white dwarf. Because white dwarf radii decrease with increasing mass, the lower-mass companion dominates the optical spectrum and is identified as the *spectroscopic primary*. Only its T_{eff} can thus be directly measured, whereas the more massive secondary remains unseen. Such white dwarf binaries are called *single-line binaries* for this reason. In the Brown et al. sample the unseen secondary components typically have masses $\sim 4\,M_1$, unlike the twin systems considered in our models. Fortunately, MAD_tides' outputs do not depend on the

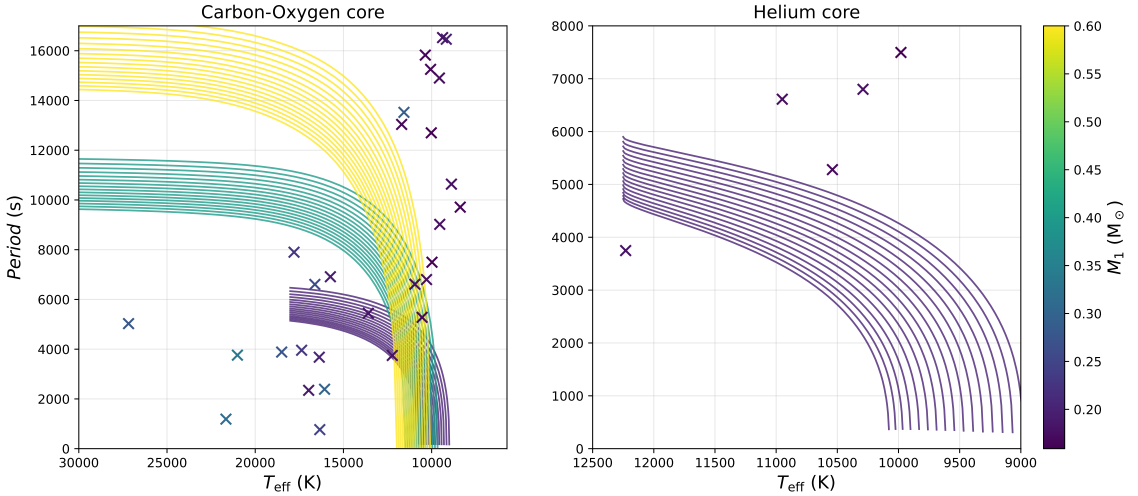

Figure 7.5: Evolution of the period of binary white dwarfs as a function of the effective temperature. Evolutionary curves on the left are for C-O core white dwarf models while evolutionary curves on the right are for a He core white dwarf model. For these models, $M_2 = 4M_1$. Each cross represents an binary system from Brown et al. (2016) with an ELM component.

---

[3] Well-known binaries with predicted LISA signal-to-noise ratios high enough to serve as calibration sources.

mass of the secondary, so we can rescale M_2 when processing those outputs and comparing them to observations. To compare these systems to our constraints on the parameter space, we overlay them on a temperature-period diagram analogous to Figure 7.5, adopting $M_2 = 4\,M_1$. Each system's location is fixed by the measured $T_{\rm eff}$ of the ELM white dwarf and the orbital period of the system.

A few points must be considered regarding the systems represented on Figure 7.5. First, the system selection made by Brown et al. (2016) was restricted to their definition of ELM white dwarfs, which largely limits the number of binary systems represented. The ELM white dwarfs observed in these systems are likely He core white dwarfs due to their low mass.[4] The most relevant comparison with our evolutionary tracks is therefore with our 0.2 $M_\odot$ He model. Each system having a different mass ratio, the 1:4 ratio chosen for this representation thus only yields the overall tendency. Note that changing this ratio even up to 1:1 does not alter our conclusion as shown on Figure D.7 in Appendix D.

Two final parameters must be considered: the stellar rotation rates and the system's eccentricity. Rotation measurements for white dwarfs in binaries are scarce. In a recent study, Lopez et al. (2021) used TESS asteroseismic data to estimate the rotation period of the ELM component in GD 278, finding a spin period of approximately 10 hr, thus sub-synchronous in regard to the 4.61 hr orbital period. This case demonstrates that unsynchronised short period binaries exist, supporting the potential existence of systems similar to those modelled in this work. The authors also report that GD 278's eccentricity is effectively close to zero, as is the case for all but one system in the Brown et al. (2016) sample.[5] Thus, the circular approximation is reasonable given these observational constraints. **In conclusion, our findings indicate that systems being located within a region of parameter space where resonance locking is likely to occur during their future evolution do exist.**

As a final note, these systems are compared only to the conditions required to encounter *sub-synchronous* locking points. It is therefore very likely that many systems satisfy the criteria for super-synchronous locking points, further reinforcing our conclusion that such binaries do exist in nature.

---

[4] Such low-mass white dwarfs cannot form via single-star evolution and must have been stripped of their envelopes before helium ignition. They therefore retain helium cores (e.g. Kepler et al. 2007, Althaus et al. 2013).

[5] The J1631+0605 system listed in Brown et al. (2016) may have an eccentricity up to 0.3.

Conclusions and Prospects

1. Overview of objectives and approach

The principal aim of this thesis was to investigate the interplay between tidal interactions and gravitational wave emission in double DA white dwarf binaries. Guided by the six questions formulated in the introduction, we first established the theoretical foundations of asteroseismology and general relativity. We then applied these principles using state-of-the-art white dwarf models (Fontaine et al., 2001) and the non-adiabatic codes *MAD* and *MAD_tides* to quantify tidal torques and gravitational wave-driven orbital decay. By computing the impact of tides on the semi-major axis near synchronisation and implementing Peters' gravitational wave formula for orbital decay, we have characterised their joint influence. This allowed us to determine the conditions under which locking points occur and the parameters that favour their occurrence. After identifying resonance locking points for several systems, we performed backward integrations of the gravitational wave equations to trace the evolutionary histories of our models, thereby constraining the region of parameter space in which resonance locking can arise. Finally, these theoretical constraints were confronted with the available observational data.

2. Key findings addressing the research questions

2.1 Dominance of gravitational waves vs tides Gravitational wave emission is the overwhelmingly dominant driver of orbital decay for most of the inspiral of double white dwarf binaries, exceeding tidal contributions by several orders of magnitude. Only in the immediate vicinity of synchronisation—both just above (super-synchronous) and just below (sub-synchronous)—do tides intensify significantly, and usually they still fail to balance the effect of gravitational waves.

2.2 Existence of resonance locking points In most situations, the modest increase in tidal strength near synchronisation alone is insufficient to balance gravitational wave decay. However, when the orbital forcing frequency enters resonance with a white dwarf's free oscillation frequency, tides undergo a sharp enhancement. In many cases this peak overtakes gravitational wave torques, yielding *resonance locking points* at the intersection where the two effects compensate. Conversely, if tidal effects at resonance reinforce gravitational wave decay, the semi-major axis can drop abruptly, leading to *kicks.* For very low-mass, rapidly rotating C-O white dwarfs, the regime where tides exceed gravitational waves can produce similar behaviour even without resonance.

2.3 Governing parameters Lower-mass, larger-radius, rapidly rotating white dwarfs in binaries are most prone to locking points. To encounter sub-synchronous locking points, a DA white dwarf must enter the near-synchronous regime while within the ZZ Ceti instability strip. Core composition also modulates this effect.

2.4 Evolution near locking Away from synchronisation, Peters' equations alone reproduce the orbital evolution to high accuracy. Near resonance, however, dynamical tidal must be accounted for. Only through a full orbital integration (e.g. with an adapted version of the *TREMOR* code) can the system's behaviour at locking and during kicks be captured.

2.5 Parameter space region Backward integration from identified sub-synchronous locking points reveals that earlier in their evolution, when at higher temperatures, such systems must have had short orbital periods—typically below a few hours. Systems likely to encounter sub-synchronous resonance locking are thus confined to a narrow region in mass, temperature and separation.

2.6 Observational evidence Comparison with the extremely low-mass white dwarf sample of Brown et al. (2016) and the unsynchronised system GD 278 (Lopez et al., 2021) indicates that binaries satisfying our locking criteria are likely to exist.

3. Limitations

Our analysis is based on white dwarf models with carbon-oxygen cores that assume a pure-carbon core composition. Recent asteroseismic studies indicate significantly higher oxygen fractions than previously believed, which may alter the quantitative results of our analysis (Giammichele et al., 2022). Similarly, we restricted our study to temperatures near the blue edge of the ZZ Ceti instability strip, due to uncertainties on the oscillation behaviour close to the red edge. Although these limitations may alter quantitative thresholds, we expect our qualitative conclusions on resonance locking to remain valid.

On the computational side, the fixed semi-major axis grid in *MAD_tides* cannot resolve true resonance peaks—so we likely underestimate both the number and strength of resonance locking and kick points. The sign problem in the super-synchronous regime disallowed us from exploring further super-synchronous locking points. The effects of mass, rotation, and core composition are expected to remain the same in that regime. However, in contrast to the sub-synchronous locking points, the system must be outside the ZZ Ceti instability strip to encounter such points there. This should largely extend the range of systems likely to experience resonance locking. However, it must be noted that no system was found where tides overtook gravitational waves in the super-synchronous regime. Finally, our orbital evolution code encountered issues when modelling systems at resonance locking or kicks. A fully self-consistent integration of tides and gravitational waves remains to be implemented.

4. Future work

Improved knowledge and modelling of white dwarfs will refine the constraints on parameter space. Most notably, incorporating updated structures from recent asteroseismic studies (e.g. Giammichele et al. 2022) for carbon-oxygen white dwarfs would be an important extension. As shown in Chapter 5, the treatment of cooling processes and timescales can vary significantly between models, which also impacts those constraints. It is thus important to consider evolutionary sequences built with the most up-to-date knowledge of these timescales.

Enhancing *MAD_tides* to converge on resonance peaks—thereby capturing all potential locking points and resolving the super-synchronous sign ambiguity—would better quantify the emergence of resonance locking and allow to explore the super-synchronous regime.

Developing a robust orbital integrator that continuously couples tidal and relativistic torques, would allow the modelling of these systems' behaviour at resonance locking and kicks. In addition, including tidal heating in such a code would be valuable to assess its effect on cooling timescales and thus on the initial conditions. Further study of mass transfer and accretion within a complete evolutionary framework would also be beneficial.

Our developments suggest that radius is a key factor in promoting resonance locking. Consequently, applying our methodology to less compact stars such as subdwarf B star (SdB) in binary systems could reveal stronger tidal interactions and a markedly different balance between tidal and gravitational wave effects.

5. Broader implications and final remarks

Our non-adiabatic approach supports the possibility that tidal and gravitational wave effects on the semi-major axis can counterbalance. Further exploration of these results will improve our understanding of white dwarf binary evolution, contributing to the understanding of the measurements of binary white dwarfs, and inform merger rate estimates, Type Ia supernova progenitor models and LISA verification sources. This thesis thus paves the way for future works in a scientific landscape where compact stars binaries continue to experience an unprecedented gain in interest.

Appendix A

Dynamical Stability

In this appendix we provide further details on the derivation of the dynamical stability criteria for radial oscillations, as obtained within the adiabatic approximation. Here, we focus on the general solution of the oscillation equation and show how the sign of the eigenvalues, σ^2, determines whether the star is dynamically stable or unstable. The general solution of the Sturm-Liouville problem (Eq. (2.47)) is given by

$$\xi(r,t) = \mathrm{Re}\left(\sum_{j=1}^{\infty} c_j\, \xi_j(r)\, e^{i\sigma_j t}\right), \qquad c_j = \left\langle \xi_j \,\middle|\, \xi_0 - \frac{i}{\sigma_j}\frac{\partial \xi_0}{\partial t} \right\rangle, \tag{A.1}$$

with the initial conditions

$$\xi(r,0) = \xi_0(r), \tag{A.2}$$

$$\frac{\partial \xi}{\partial t}(r,0) = \frac{\partial \xi_0}{\partial t}(r). \tag{A.3}$$

As the σ^2 are solutions of a Sturm-Liouville problem, they are, by definition, real. However, this does not imply that the σ themselves are real. Since the solutions are ordered, if at least one σ^2 is negative then, in particular, σ_1^2 is negative. Let us examine the two scenarios:

- If $\sigma_1^2 > 0$, then $\sigma_j^2 > 0$ for all j, and hence all the σ_j are real. From Eq. (A.1) it follows that all the modes are oscillatory and the star is said to be *dynamically stable.*
- If $\sigma_1^2 < 0$, then $\sigma_1 = \pm i\,\eta_1$, with η_1 real. Consequently, the $j = 1$ term in Eq. (A.1) exhibits exponential growth (or decay), signalling that the star is *dynamically unstable.*

Hence, an inspection of σ_1 alone provides insight into the dynamical stability of the star.

Appendix B

Legendre Polynomials

This appendix is dedicated to a more detailed development leading to the Legendre polynomial when developing the tidal potential. This result can be obtained developing the second factor of Eq (3.21) through a Taylor expansion. Indeed, this term is of the form $(1-x)^{-1/2}$, with $x = 2(r/r_2)\lambda + (r^2/r_2^2)$. As we study the effect of the gravitational potential of M_2 in M_1, which is centred in $r = 0$, we can develop this expression around $x = 0$. The Taylor expansion of a function $f(x)$ around the point a is given by:

$$f(x) \approx \sum_{n=0}^{\infty} \frac{f^{(n)}(x=a)}{n!} (x-a)^n \, , \quad f^{(n)} = \frac{\partial^n f}{\partial x^n} \tag{B.1}$$

In this case, $a = 0$ and the first three derivatives of $f(x)$ evaluated in $x = 0$ are:

$$\left[\frac{\partial^0 f}{\partial x^0}\right]_{x=0} = [1-x]_{x=0} = 1 \tag{B.2}$$

$$\left[\frac{\partial^1 f}{\partial x^1}\right]_{x=0} = \left[\frac{1}{2}(1-x)^{-3/2}\right]_{x=0} = \frac{1}{2} \tag{B.3}$$

$$\left[\frac{\partial^2 f}{\partial x^2}\right]_{x=0} = \left[\frac{3}{4}(1-x)^{-5/2}\right]_{x=0} = \frac{3}{4} \tag{B.4}$$

One can easily show that these derivatives are rigorously given by:

$$\left[\frac{\partial^n f}{\partial x^n}\right]_{x=0} = \left[\frac{(2n)!}{2^{2n}n!}(1-x)^{-1/2}\right]_{x=0} = \frac{(2n)!}{2^{2n}n!} \tag{B.5}$$

Therefore the Taylor expansion of $(1-x)^{-1/2}$ around $x = 0$ is:

$$(1-x)^{-1/2} = \sum_{n=0}^{\infty} \frac{(2n)!}{(2^n n!)^2} x^n \tag{B.6}$$

Hence,

$$\frac{1}{r_2}\left(1-2\frac{\vec{r}\cdot\vec{r_2}}{r_2^2}+\frac{r^2}{r_2^2}\right)^{-\frac{1}{2}} \approx \frac{1}{r_2}\left[1+\frac{1}{2}\left(2\frac{r}{r_2}\lambda+\frac{r^2}{r_2^2}\right)+\frac{3}{8}\left(2\frac{r}{r_2}\lambda+\frac{r^2}{r_2^2}\right)^2+\mathcal{O}\left(x^3\right)\right] \tag{B.7}$$

$$\approx \frac{1}{r_2}\left[1+\lambda\left(\frac{r}{r_2}\right)+\frac{1}{2}\left(3\cos^2\theta-1\right)\left(\frac{r}{r_2}\right)^2+\mathcal{O}\left(\frac{r^3}{r_2^3}\right)\right] \tag{B.8}$$

$$\approx \frac{1}{r_2}\left[P_0(\lambda)+P_1(\lambda)\left(\frac{r}{r_2}\right)+P_2(\lambda)\left(\frac{r}{r_2}\right)^2+\mathcal{O}\left(\frac{r^3}{r_2^3}\right)\right] \tag{B.9}$$

where we introduce the Legendre polynomials $P_l(\lambda)$ to obtain Eq (B.9). Historically, the Legendre polynomials were introduced through a development similar to the Taylor expansion presented above.

Appendix C

Python codes

This section is dedicated to the presentation of the Python functions implemented in this work. The external packages imported for this implementation are NumPy (Harris et al., 2020) and SciPy (Virtanen et al., 2020):

```python
import numpy as np
from scipy import integrate
from scipy.special import lpmv, factorial
```

Computing the effect of gravitational waves on the semi-major axis is relatively straightforward, as it simply requires implementing Eq. (4.1):

```python
def da_dt_gw_e(m1, m2, a, e):
    """
    Compute the rate of change of the semi-major axis (da/dt)
    due to gravitational wave emission for an eccentric binary
    system, using Peters' formula.

    Parameters
    ----------
    m1 : float
        Mass of the first body in g
    m2 : float
        Mass of the second body in g
    a : float
        Semi-major axis in cm
    e : float
        Orbital eccentricity (0 <= e < 1)

    Returns
    -------
    da_dt : float
        Time derivative of the semi-major axis [cm/s]
        Should be negative (orbital decay)
    """
    # Check eccentricity
    if not (0.0 <= e < 1.0):
        raise ValueError(f"Eccentricity must be in [0,1[, got e={e}")

```

```
    G = 6.67430e-8       # gravitational constant [cm3 g-1 s-2]
    c = 2.99792458e10    # speed of light [cm/s]

    # prefactor = -(64/5) * G^3 * m1 * m2 * (m1 + m2) / (c^5 * a^3 * (1 - e^2)^(7/2))
    prefactor = -64.0 / 5.0 * (G**3 * m1 * m2 * (m1 + m2)) / (c**5 * a**3 * (1 - e**2)**(7/2))

    # eccentricity polynomial: 1 + 73/24 e^2 + 37/96 e^4
    pol_e = 1.0 + (73.0/24.0)*e**2 + (37.0/96.0)*e**4

    return prefactor * pol_e
```

The effect of tides is more complicated to implement. However, by restricting to circular orbits and ($l = 2, m = \pm 2, k = \mp 2$), the expressions simplify because the values of $G^{(2)}_{2,\pm 2,\mp 2}(0)$ are provided in Willems et al. (2010). In this case, the implementation reduces to:

```
def da_dt_tides(m1, m2, r1, a, P_orb, Im_psi, l, m):
    """
    Parameters:
    -----------
    m1 : float
        Mass of the first component in g
    m2 : float
        Mass of the second component in g
    r1 : float
        Radius of the first component in solar radius
    a : float
        Semi-major axis of the orbit in cm.
    P_orb: float
        Orbital period in days
    Im: float
        Imaginary part of the forcing (IM(phi)/(GM/R))
    l: int
        spherical degree
    m: int
        azimuthal degree

    Returns:
    --------
    da_dt : float
        The time derivative of the semi-major axis in cm/s (a negative value indicates orbital decay).
    """
    # conversions
    Omega_orb = (2.*np.pi)/(P_orb*24*3600) # convert to Hz

    Im_F = (-1./2.) * Im_psi

    if ((l == 2) & (m == 2)):
        G2_lmk = -3./2.
    elif ((l == 2) & (m == -2)):
```

```
        G2_lmk = 3./2.
    else:
        raise ValueError("l, m, combination not supported for
            G2_lmk")
```

where `Im_psi` is notably an output of MAD_tides.

For non-circular binaries and other oscillation modes, computing the effect of tides on gravitational waves requires a careful computation of $G^{(2)}_{l,m,k}(e)$ as presented in Section 6.2. This requires to implement a few functions as presented below.

First, because the Hansen coefficients involve the mean anomaly $\mathcal{M}$, we must recover $\mathcal{M}(\nu)$ exactly from the true anomaly ν by solving Eqs. (6.10) and (6.11). This requires obtaining the eccentric anomaly E from the true anomaly via a quadrant-safe arctan formulation. NumPy's `arctan2` function handles this, ensuring E spans $[0, 2\pi[$. With $E(\nu)$, we can then compute $\mathcal{M} = E - e \sin E$ and normalize it to $[0, 2\pi[$. The following function performs this conversion:

```
def true_to_mean_anomaly(nu, e):
    """
    Convert true anomaly to mean anomaly M for an elliptical
        orbit.

    Parameters
    ----------
    nu : array_like or float
        True anomaly in radians
    e : float
        Orbital eccentricity (0 <= e < 1)

    Returns
    -------
    M : array_like or float
        Mean anomaly in radians, in [0, 2*pi)
    """
    # Eccentric anomaly via quadrant-safe atan2
    E = 2 * np.arctan2(
        np.sqrt(1 - e) * np.sin(nu / 2),
        np.sqrt(1 + e) * np.cos(nu / 2)
    )
    # Mean anomaly
    M = E - e * np.sin(E)
    # Normalize to [0, 2*pi)
    return np.mod(M, 2 * np.pi)
```

Having $\mathcal{M}(\nu)$, we then compute the Hansen coefficients $X_k^{n,m}(e)$ (Eq. (3.35)), where we perform the integration using SciPy's `integrate.quad`:

```
def Hansen_coef(e, n, m, k):
    """
    Compute the Hansen coefficient X_k^{n,m}(e) by direct
        integration.
```

```

    X = (1-e^2)^(n+1.5) / (2*pi)
        * integral_0^{2*pi} [ cos(-m*nu + k*M(nu)) / (1 + e*cos(nu))^(n+2) ] dnu

    Parameters
    ----------
    e : float
        Orbital eccentricity (0 <= e < 1)
    n : float
        Exponent parameter in the denominator
    m : int
        Mode index
    k : int
        Fourier index in mean anomaly

    Returns
    -------
    X : float
        The Hansen coefficient
    """
    prefac = (1.0 - e**2)**(n + 1.5) / (2.0 * np.pi)

    def integrand(nu):
        M = true_to_mean_anomaly(nu, e)
        denom = (1.0 + e * np.cos(nu))**(n + 2.0)
        return np.cos(-m * nu + k * M) / denom

    integral, _ = integrate.quad(integrand, 0.0, 2.0*np.pi,
                                 epsabs=1e-9, epsrel=1e-9)
    return prefac * integral
```

The Hansen coefficients are then used to compute the coefficient $c_{l,m,k}(e)$. This requires evaluating associated Legendre polynomials at $x = 0$, which we compute with SciPy's `lpmv`. In addition, we also use the `factorial` function from Scipy:

```
def c_lmk(a, e, r1, l, m, k):
    """
    Compute the tidal coefficient c_{l,m,k}(e):

      c = X_k^{-(l+1),-m}(e)
          * ((l-|m|)! / (l+|m|)!)
          * P_l^{|m|}(0)
          * (r1 / a)^(l-2)

    Parameters
    ----------
    a : float
        Semi-major axis
    e : float
        Eccentricity (0 <= e < 1)
    r1 : float
        Radius of the perturbed body
    l : int
```

```
        Degree (must be >= 2)
    m : int
        Order (abs(m) <= l)
    k : int
        Fourier index (often k = -m)

    Returns
    -------
    c : float
        The tidal coefficient
    """
    # Hansen part
    X = Hansen_coef(e, n=-(l+1), m=-m, k=k)

    # factorial ratio (l-|m|)! / (l+|m|)!
    mm = abs(m)
    fact_ratio = factorial(l - mm, exact=True) / factorial(l + mm, exact=True)

    # associated Legendre at x=0
    P0 = lpmv(mm, l, 0.0)

    # radial factor
    radial = (r1 / a)**(l - 2)

    return X * fact_ratio * P0 * radial
```

With $c_{l,m,k}(e)$ and $\mathcal{M}(\nu)$ in hand, we compute the coefficient $G^{(2)}_{l,m,k}(e)$ by assembling $c_{l,m,k}$, another factor $P_l^{|m|}(0)$, and two integrals over ν following Eq. (3.39). This is implemented as:

```
def g_lmk_2(e, l, m, k, r1, a):
    """
    Compute the coefficient G_{l,m,k}^{(2)}(e):

      G = 2 / [pi * (1-e^2)^(l+1)]
          * c_lmk(e)
          * P_l^{|m|}(0)
          * [ (l+1)*e * I1   -   m * I2 ]

    where
      I1 = integral_0^pi [ (1+e*cos(nu))^l
                         * sin(m*nu + k*M(nu))
                         * sin(nu) ] dnu

      I2 = integral_0^pi [ (1+e*cos(nu))^(l+1)
                         * cos(m*nu + k*M(nu)) ] dnu

    Parameters
    ----------
    e : float
        Eccentricity (0 <= e < 1)
    l : int
```

```
        Degree (integer >= 2)
    m : int
        Order (integer with |m| <= l)
    k : int
        Fourier index (commonly k = -m)
    r1 : float
        Radius of perturbed body
    a : float
        Semi-major axis

    Returns
    -------
    G2 : float
        The value of G_{l,m,k}^{(2)}(e)
    """
    # basic checks
    if not isinstance(l, int) or l < 2:
        raise ValueError(f"l must be integer >= 2, got {l}")
    if not isinstance(m, int) or abs(m) > l:
        raise ValueError(f"m must satisfy |m|<=l, got m={m}")
    if not isinstance(k, int):
        raise ValueError(f"k must be integer, got {k}")
    if not (0.0 <= e < 1.0):
        raise ValueError(f"eccentricity must be in [0,1), got {e}")

    # tidal coefficient
    c = c_lmk(a=a, e=e, r1=r1, l=l, m=m, k=k)

    # P_l^{|m|}(0)
    P0 = lpmv(abs(m), l, 0.0)

    # mean anomaly function
    M_of = np.vectorize(lambda nu: true_to_mean_anomaly(nu, e))

    # integrands
    def I1(nu):
        return ((1 + e*np.cos(nu))**l
                * np.sin(m*nu + k*M_of(nu))
                * np.sin(nu))

    def I2(nu):
        return (1 + e*np.cos(nu))**(l+1) * np.cos(m*nu + k*M_of(nu))

    # perform integrals over nu = 0..pi
    int1, _ = integrate.quad(I1, 0.0, np.pi, epsabs=1e-9, epsrel=1e-9)
    int2, _ = integrate.quad(I2, 0.0, np.pi, epsabs=1e-9, epsrel=1e-9)

    denom = np.pi * (1 - e**2)**(l + 1)
    bracket = (l + 1)*e * int1 - m * int2

    return 2.0 / denom * c * P0 * bracket
```

We added additional verifications, notably to ensure that the theoretical conditions imposed on l and m are verified. In addition, we make sure that l, m and k are all integers as to avoid notably error with the `factorial` function.

Finally, this function can be used to compute the derivative of the semi-major axis:

```python
def da_dt_tides_e(m1, m2, r1, a, e, P_orb, Im_psi, l, m, k):
    """
    Compute the rate of change of the semi-major axis due to
        tidal interactions.

    Parameters
    ----------
    m1 : float
        Mass of the first component in g
    m2 : float
        Mass of the second component in g
    r1 : float
        Radius of the first component in solar radius
    a : float
        Semi-major axis of the orbit in cm
    e : float
        Orbital eccentricity (0 <= e < 1)
    P_orb : float
        Orbital period in days
    Im_psi : float
        Imaginary part of the forcing (IM(phi)/(GM/R))
    l : int
        Spherical degree (l)
    m : int
        Azimuthal degree (m)
    k : int
        Fourier index (k)

    Returns
    -------
    da_dt : float
        The time derivative of the semi-major axis in cm/s (a
            negative value indicates orbital decay)
    """
    # conversions
    Omega_orb = (2.0 * np.pi) / (P_orb * 24 * 3600)  # convert
        to Hz

    Im_F = (-1.0 / 2.0) * Im_psi

    # Compute G_{l,m,k}^{(2)}
    G2_lmk = g_lmk_2(e=e, l=l, m=m, k=k, r1=r1, a=a)

    return 4.0 * Omega_orb * (m2 / m1) * (r1 ** (l + 3)) * (a **
        (-(l + 2))) * Im_F * G2_lmk
```

Following a few direct computational steps, the output of these functions was used to build the plots presented in this work using the Matplotlib package (Hunter, 2007).

Appendix D

Supplementary figures

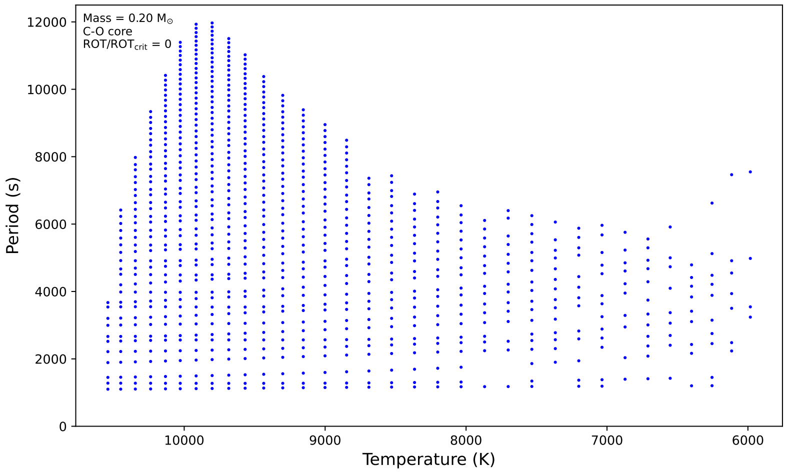

Figure D.1: Period of unstable g-modes (blue) for a 0.2 $M_\odot$ C-O model as a function of its effective temperature.

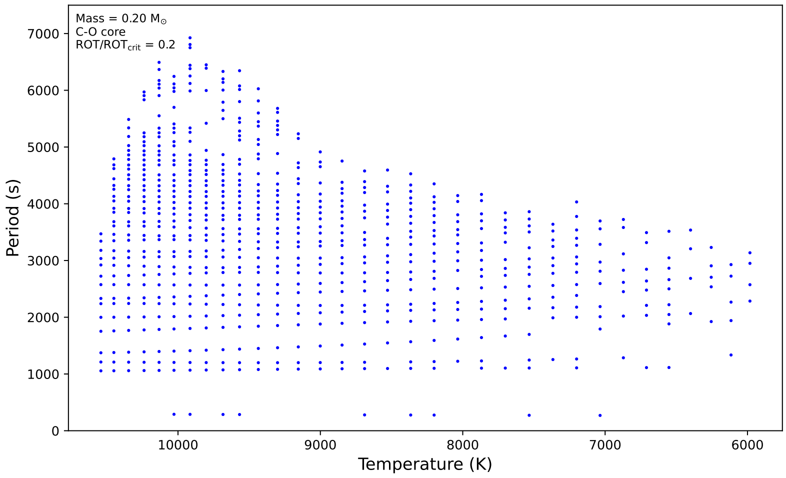

Figure D.2: Period of unstable g-modes (blue) for a rotating (ROT/ROT$_{\text{crit}}$ = 0.1) 0.2 $M_\odot$ C-O model as a function of its effective temperature.

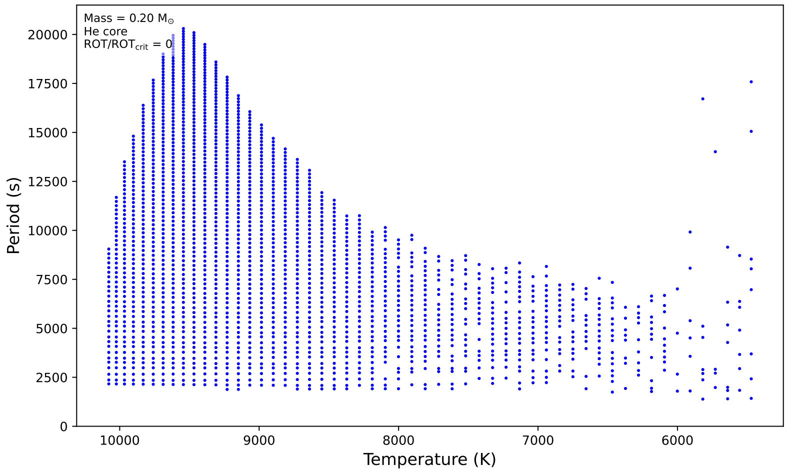

Figure D.3: Period of unstable g-modes (blue) for a 0.2 $M_\odot$ He model as a function of its effective temperature.

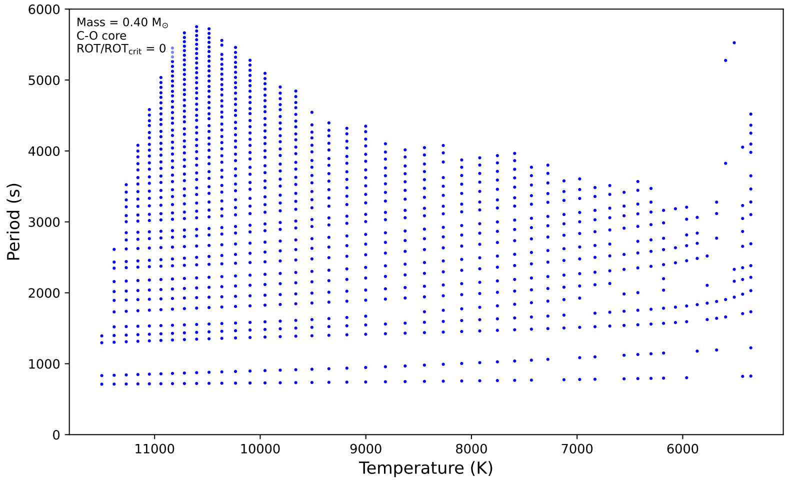

Figure D.4: Period of unstable g-modes (blue) for a 0.4 $M_\odot$ C-O model as a function of its effective temperature.

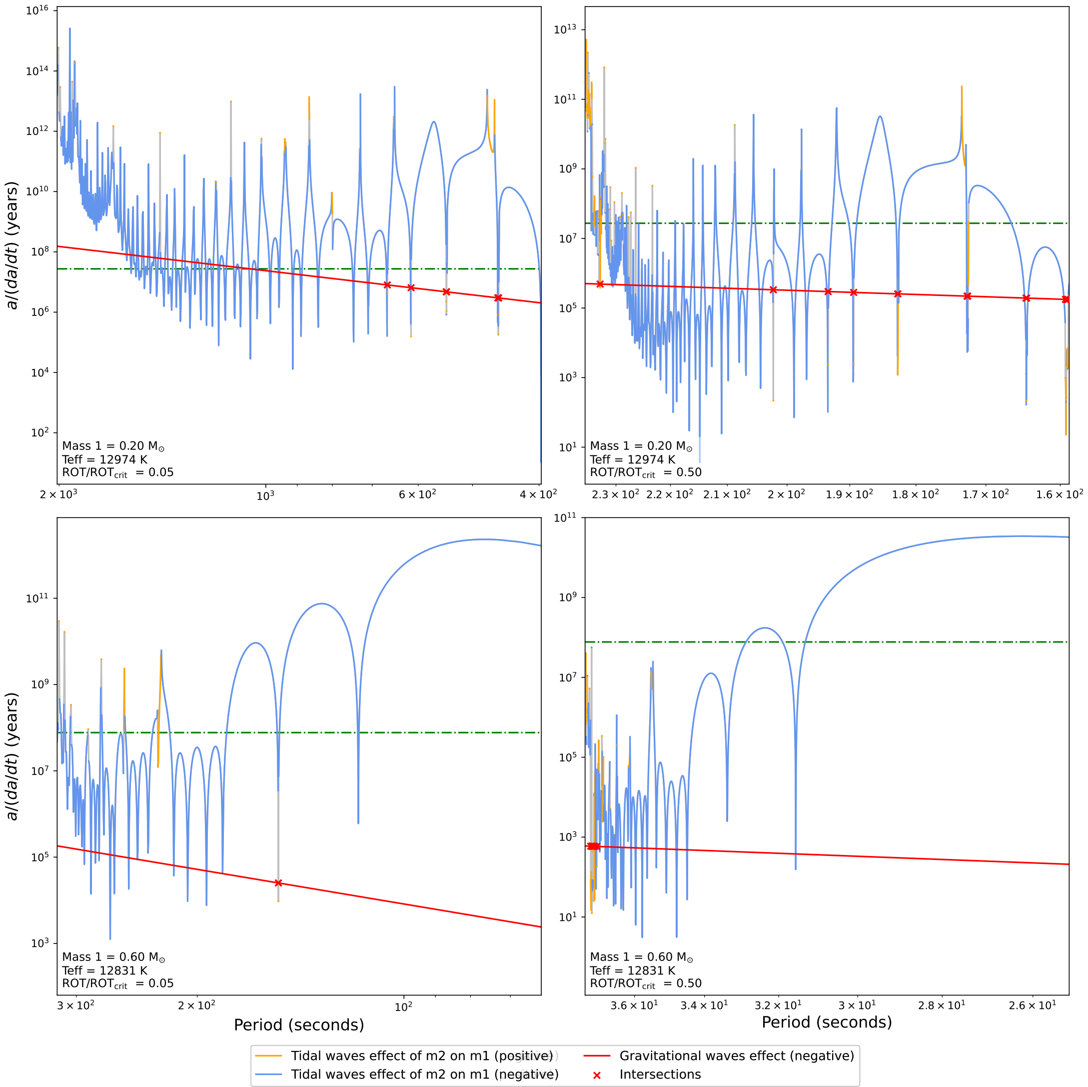

Figure D.5: Comparison of $a/(da/dt)$ for different masses and rotation ($\mathrm{ROT}/\mathrm{ROT}_{\mathrm{crit}}$). The upper plots corresponds to 0.2 $M_\odot$ and the lower to 0.6 $M_\odot$. The left column corresponds to a slow rotation of $\mathrm{ROT}/\mathrm{ROT}_{\mathrm{crit}} = 0.05$, while the right column corresponds to a fast rotation of $\mathrm{ROT}/\mathrm{ROT}_{\mathrm{crit}} = 0.5$. The effective temperatures were chosen such that each model lies before the instability strip. The period ranges are selected to begin directly after each system reaches synchronisation and cover the region of the sub-synchronous regime where tides are strongest.

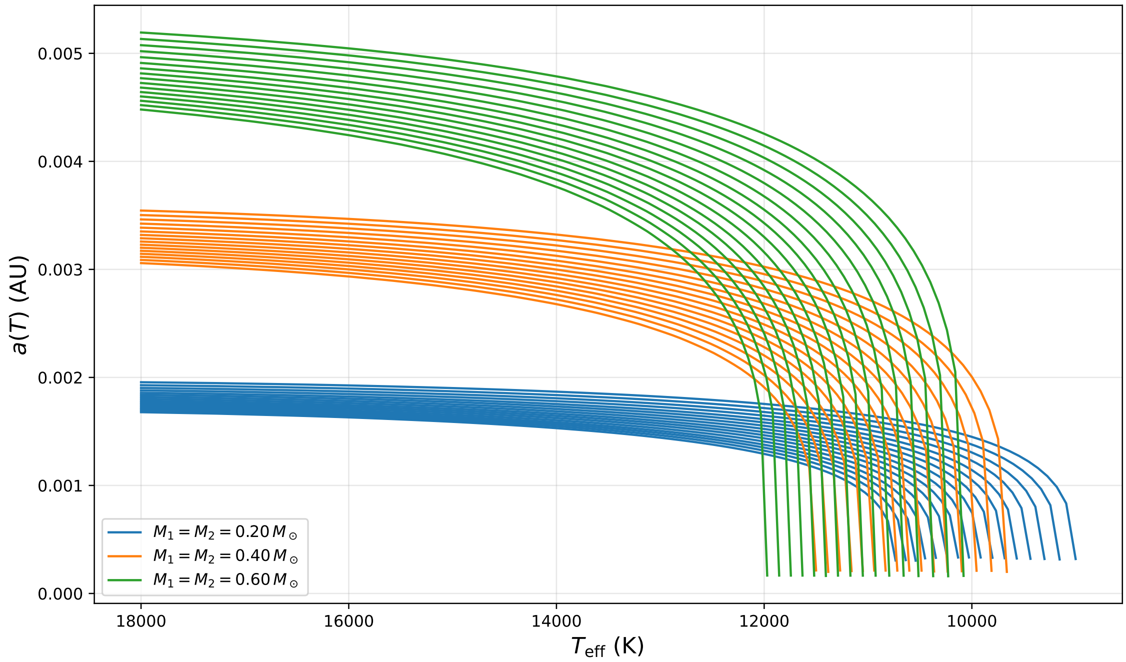

Figure D.6: Evolution of the separation of binary C-O white dwarfs as a function of effective temperature. The curves are obtained by integrating the gravitational wave equations starting from the first sub-synchronous resonance locking point up to a temperature of 18000 K. The rotation was set to 30% of the critical rotation.

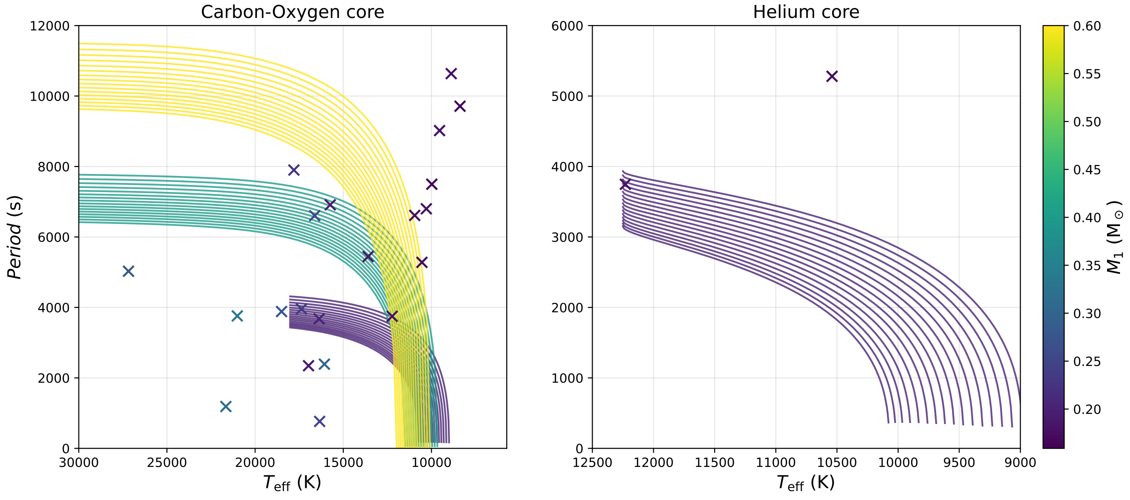

Figure D.7: Evolution of the period of binary white dwarfs as a function of the effective temperature. Evolutionary curves on the left are for C-O core white dwarf models while evolutionary curves on the right are for a He core white dwarf model. For these models, $M_2 = M_1$. Each cross represents an binary system from Brown et al. (2016) with an ELM component.

Bibliography

Abbott, B. P., Abbott, R., Abbott, T. D., et al. 2016, Phys. Rev. Lett., 116, 061102

Abbott, B. P., Abbott, R., Abbott, T. D., et al. 2017, Phys. Rev. Lett., 119, 161101

Abbott, R., Abbott, T. D., Acernese, F., et al. 2023, Phys. Rev. X, 13, 041039

Althaus, L. G., Miller Bertolami, M. M., & Córsico, A. H. 2013, A&A, 557, A19

Bédard, A. 2024, Ap&SS, 369, 43

Bédard, A., Bergeron, P., Brassard, P., & Fontaine, G. 2020, ApJ, 901, 93

Bétrisey, J. 2024, PhD thesis, University of Geneva, Switzerland

Boffin, H. 2014, Mass Transfer by Stellar Wind

Brickhill, A. J. 1991, MNRAS, 251, 673

Brown, W. R., Gianninas, A., Kilic, M., Kenyon, S. J., & Allende Prieto, C. 2016, ApJ, 818, 155

Bédard, A. 2020, White dwarf cooling models, accessed: 15-Apr-2025

Detweiler, S. 1979, ApJ, 234, 1100

Dupret, M. A. 2001, A&A, 366, 166

Dupret, M. A., Grigahcène, A., Garrido, R., Gabriel, M., & Scuflaire, R. 2005, A&A, 435, 927

Eggleton, P. P. 1983, ApJ, 268, 368

Einstein, A. 1916, Sitzungsberichte der Königlichen Preußischen Akademie der Wissenschaften, 688

Einstein, A. 1918, Sitzungsberichte der Königlichen Preußischen Akademie der Wissenschaften, 154

ESA. 2023, Monthly Notices of the Royal Astronomical Society

ESO. 2007, Hertzprung-Russell diagram

Fellay, L. & Dupret, M. A. 2025, A&A, 694, A51

Fellay, L., Dupret, M. A., & Rosu, S. 2024, A&A, 683, A210

Fitzpatrick, R. 2021, Introduction to Celestial Mechanics, 2nd Edition (The University of Texas at Austin)

Fontaine, G. & Brassard, P. 2008, PASP, 120, 1043

Fontaine, G., Brassard, P., & Bergeron, P. 2001, PASP, 113, 409

Fuller, J. 2017, MNRAS, 472, 1538

García, R. A. & Ballot, J. 2019, Living Reviews in Solar Physics, 16, 4

Giammichele, N., Charpinet, S., & Brassard, P. 2022, Frontiers in Astronomy and Space Sciences, Volume 9 - 2022

Giammichele, N., Charpinet, S., Fontaine, G., et al. 2018, Nature, 554, 73

Grigahcène, A., Dupret, M. A., Gabriel, M., Garrido, R., & Scuflaire, R. 2005, A&A, 434, 1055

Harris, C. R., Millman, K. J., van der Walt, S. J., et al. 2020, Nature, 585, 357

Heaviside, O. 1894-1912, Electromagnetic theory (London, "The Electrician" printing and publishing company, limited)

Houdek, G. & Dupret, M.-A. 2015, Living Reviews in Solar Physics, 12, 8

Hunter, J. D. 2007, Computing in Science & Engineering, 9, 90

Jackim, R., Heyl, J., & Richer, H. 2024, arXiv e-prints, arXiv:2404.07388

Kepler, S. O., Kleinman, S. J., Nitta, A., et al. 2007, MNRAS, 375, 1315

Kupfer, T., Korol, V., Littenberg, T. B., et al. 2024, ApJ, 963, 100

Kurtz, D. W. 2022, Ann. Rev. Astron. Astroph., 60, 31

Lopez, I. D., Hermes, J. J., Calcaferro, L. M., et al. 2021, ApJ, 922, 220

Nordlund, Å. & Stein, R. F. 2001, ApJ, 546, 576

Offner, S. S. R., Moe, M., Kratter, K. M., et al. 2023, in Astronomical Society of the Pacific Conference Series, Vol. 534, Protostars and Planets VII, ed. S. Inutsuka, Y. Aikawa, T. Muto, K. Tomida, & M. Tamura, 275

Ott, C. D. 2009, Classical and Quantum Gravity, 26, 063001

Peters, P. C. 1964, PhD thesis, California Institute of Technology, see p. 105

Pointcaré, H. 1905, Comptes Rendus de l'Académie des Sciences, 140, 1504

Schaffner-Bielich, J. 2020, Compact Star Physics (Cambridge University Press)

SciPy Community. 2025, Integration and ODEs: scipy.integrate.solve_ivp

Sesana, A., Vecchio, A., & Colacino, C. N. 2008, Monthly Notices of the Royal Astronomical Society, 390, 192

Sion, E. M., Greenstein, J. L., Landstreet, J. D., et al. 1983, ApJ, 269, 253

Tremblay, P.-E., Fontaine, G., & Ludwig, H.-G. 2015, in IAU General Assembly, Vol. 29, 2253532

Van Grootel, V., Dupret, M. A., Fontaine, G., et al. 2012, A&A, 539, A87

Virtanen, P., Gommers, R., Oliphant, T. E., et al. 2020, Nature Methods, 17, 261

Wesemael, F., Greenstein, J. L., Liebert, J., et al. 1993, PASP, 105, 761

Willems, B., Deloye, C. J., & Kalogera, V. 2010, ApJ, 713, 239

Williams, D. 2016, GW150914 Infographic, accessed: 26-Mar-2025

Williams, J. G. & Boggs, D. H. 2016, Celestial Mechanics and Dynamical Astronomy, 126, 89